A STUDY OF ELECTRODEPOSITED NEGATIVE ELECTRODES FOR LITHIUM-ION BATTERIES WITH AN EMPHASIS ON COMBINATORIAL ELECTRODEPOSITION

By

Shane D. Beattie

SUBMITTED IN PARTIAL FULFILLMENT OF THE REQUIREMENTS
FOR THE DEGREE OF DOCTOR OF PHILOSOPHY

AT

DALHOUSIE UNIVERSITY
HALIFAX, NOVA SCOTIA
April 2004

Your file Votre référence
ISBN: 0-612-89796-6
Our file Notre référence
ISBN: 0-612-89796-6

DALHOUSIE UNIVERSITY

To comply with the Canadian Privacy Act the National Library of Canada has requested that the following pages be removed from this copy of the thesis:

Preliminary Pages
- Examiners Signature Page (pii)
- Dalhousie Library Copyright Agreement (piii)

Appendices
- Copyright Releases (if applicable)

Table of Contents

List of Figures viii

List of Tables xiv

List of Abbreviations and Symbols Used xv

Abstract xx

Acknowledgements xxi

1. Motivation 1

1.1 Rechargeable batteries 1

1.1.1 Battery terminology 1

1.2 Basic electrochemistry 2

1.3 Commercial Li-ion batteries 4

1.3.1 Cell geometry 6

1.4 Desirable characteristics of electrode materials 7

1.4.1 Capacity 7

1.4.2 Average voltage 10

1.4.3 Reversibility 11

1.5 Nanocomposites 16

1.6 Conventional fabrication methods 16

1.7 Advantages of electrodeposition 17

2. Experimental techniques 19

2.1 Characterization 19

2.1.1 X-ray diffraction 19
2.1.2 Electron microprobe 20
2.1.3 Electrochemical testing 30
2.2 Electrodeposition 34
2.2.1 Instruments 34
2.2.2 Software 34
2.2.3 Plating baths 36
2.2.4 Electroplating cells 38
2.2.5 Cleaning, substrates and plater's tape 40
2.3 Sputter deposition 41
2.4 Preparation of powdered Sn electrodes 41
3. Theory of electrodeposition 42
3.1 Electrode/solution interface potentials 42
3.2 Standard hydrogen reference electrode 44
3.3 RedOx potentials 46
3.4 Reference electrodes 48
3.5 Standard electrode potentials 53
3.6 Overpotential 54
3.7 Mechanisms of electrodeposition 54
3.8 Leveling agents 57
3.9 Pulse plating 59
3.10 Immersion plating 63
4. Results and discussion 65

4.1 Behavior of electroplated Sn in a Li-cell 65

4.1.1 Typical behavior of electroplated Sn in a Li-cell 66

4.1.2 Observed behavior of electroplated Sn in a Li-cell 68

4.1.3 Anomalous, high-voltage irreversible capacity observed in Li-cells made from sputtered and powder Sn electrodes 74

4.2 The bronze-age 77

4.3 Combinatorial electrodeposition 92

4.4 A combinatorial library of Cu-Sn alloys 93

4.4.1 Electroplating strategy 93

4.4.2 Discussion 98

4.5 The Cu-Zn system and scalability of combinatorial electrodeposition 106

4.5.1 Results 107

4.5.2 Discussion 117

4.6 Ternary combinatorial electrodeposition 122

4.6.1 Sn-Zn 122

4.6.2 Dripped immersion plating 126

4.6.3 Compositional variation 129

4.6.4 Phenomenological model 130

5. Future work 139

5.1 Anomalous high-voltage irreversible capacity in electroplated Sn electrodes for Li batteries 139

5.2 Further studies in combinatorial electrodeposition 140

5.3 Amorphous metal alloys 142

5.4 Another method for ternary combinatorial material synthesis via electrodeposition 143

5.5 Theoretical model 145

5.6 Nanocomposites 146

5.7 Masked electrodeposition on a 64 channel combinatorial cell plate 147

6. Conclusion 158

References 161

Appendix 1 Electron binding energies 168

Appendix 2 Standard electrode potentials to the nearest 10 mV 172

List of Figures

Figure 1-1 Schematic of a basic Li-Sn cell 3

Figure 1-2 Schematic of a Li-ion battery made from a carbon-based negative electrode and a Li transition metal oxide positive electrode (from the Paul Scherrer Institute) 5

Figure 1-3 Typical design of a cylindrical 18650 cell 7

Figure 1-4 Lithium binding energy diagram for various compounds, quoted relative tolithium metal 11

Figure 1-5 Step by step schematic of SEI formation, lithiation, delithiation and subsequent cracking resulting in electrically isolated islands of material 15

Figure 2-1 Schematic of an electron transition resulting in an emitted x-ray 22

Figure 2-2 Atomic model, showing electron transitions that may follow electron vacancies. 23

Figure 2-3 Typical EDS spectra showing peaks from Cu and Sn 25

Figure 2-4 Schematic of the JEOL JXA 8900 RL electron microprobe with emphasis on the WDS detector 27

Figure 2-5 Sample WDS spectra in terms of L-spacing for a pure Zn sample 28

Figure 2-6 Exploded view of a coin cell 31

Figure 2-7 A typical pulsed waveform using a zero mA X pulse and 100 mA Y pulse 35

Figure 2-8 Two electroplating cells used to deposit metal-alloy films 39

Figure 3-1 Metal-solution interface 42

Figure 3-2 Standard hydrogen reference electrode 45

Figure 3-3 Simple schematic of a RedOx reaction on a Pt electrode in a solution of Fe^{+3} and Fe^{+2} ions 47

Figure 3-4 Schematic of a typical reference electrode 49

Figure 3-5 Silver/silver-chloride reference electrode attached to a Cu electrode immersed in a Cu sulfate solution 52

Figure 3-6 Step-wise illustration of a hydrated ion depositing into a kink site 55

Figure 3-7 Layered and 3D crystallite growth 56

Figure 3-8 Sn deposit from a simple Sn-sulfate bath with no levelers 57

Figure 3-9 Artist's rendition of how leveling agents work 59

Figure 3-10 Pulse plating waveform 61

Figure 3-11 Ideal pulse plated film, alternating layers of Sn and Cu with no interdiffusion 62

Figure 3-12 Zero current pulse plating waveform 63

Figure 4-1 A typical Li-Sn voltage profile where plateaus are well understood and correspond to a change in phase according to the Li-Sn phase diagram..... 67

Figure 4-2 The Li-Sn phase diagram. 68

Figure 4-3 Three voltage vs. capacity data sets representing three different cells using electroplated Sn negative electrodes. 69

Figure 4-4 Voltage vs. capacity for a Li/electroplated Sn cell where the recharge cut-off voltage was kept below 1.4 V 71

Figure 4-5 Anomalous high-voltage irreversible capacity vs. specific current for Li-Sn cells with electrodes prepared from a SnTech solution 72

Figure 4-6 Anomalous high-voltage irreversible capacity in a Li-Sn powder composite electrode cell 75

Figure 4-7 Anomalous high-voltage irreversible capacity observed in sputtered electrodes cycled above 1.4 V, but not in sputtered electrodes cycled to 0.8 V 76

Figure 4-8 X-ray diffraction pattern of a Cu_6Sn_5 film electroplated by pulsed deposition onto a nickel substrate 80

Figure 4-9 X-ray diffraction pattern of an electrodeposited Sn film exposed to platingsolution over night and a x-ray diffraction pattern of the unexposed film 82

Figure 4-10 X-ray diffraction patterns of three films prepared by pulsed electrodeposition from a Lucent SnTech + 0.016 M $CuSO_4 \cdot 5H_2O$ bath 84

Figure 4-11 The Cu-Sn phase diagram 86

Figure 4-12 Voltage vs. specific capacity and specific capacity vs. cycle number for a Li/Cu_6Sn_5 cell 87

Figure 4-13 Specific capacity vs. cycle number for two Li/Cu_6Sn_5 cells using different voltage windows 89

Figure 4-14 Capacity vs. cycle # data from two Cu-Sn/Li cells with different Cu:Sn ratios 91

Figure 4-15 Effect of interdiffusion on layer structure 95

Figure 4-16 Cu:Sn atomic ratio and atomic % Sn versus position on the electrodeposited film. 96

Figure 4-17 SEM image of the deposited film 97

Figure 4-18 The Cu:Sn phase diagram. The arrow indicates the region of phase space sampled by the composition-spread film 98

Figure 4-19 X-ray diffraction patterns of portions of the film. Known Sn and Cu-Sn alloy XRD patterns are superimposed on the data for comparison..... 101

Figure 4-20 Twenty XRD patterns measured at equal spacing along the length of the Cu-Sn film. 103

Figure 4-21 Capacity versus cycle number and voltage versus capacity for five Li/Cu-Sn cells 105

Figure 4-22 Atomic percent Cu or Zn vs. distance from top of film. 110

Figure 4-23 Deposited mass and thickness vs. distance from top of film. 111

Figure 4-24 Twelve XRD scans taken sequentially along the composition-spread Cu-Zn film deposited in the Hull cell..... 112

Figure 4-25 The Cu-Zn phase diagram. 113

Figure 4-26 XRD patterns of seven individual Cu-Zn bulk films prepared by conventional one-at-a-time methods. 115

Figure 4-27 XRD patterns of Cu-Zn films. 117

Figure 4-28 Compositional variation of Sn, Zn and Ni as a function of position from the top of the film 124

Figure 4-29 Structural variation of a composition-spread Sn-Zn film as a function of position 125

Figure 4-30 The Sn-Zn phase diagram 126

Figure 4-31 Modified Tsunami Blaster X water gun used as an inexpensive and convenient peristaltic pump 127

Figure 4-32 Schematic of the immersion plating timeline 128

Figure 4-33 Contour plots showing compositional variation for all three elements, Cu, Sn and Zn 130

Figure 4-34 Thickness of deposited film vs. punch number 131

Figure 4-35 Schematic of the theoretical film in both the x-y and x-z planes 132

Figure 4-36 Cu-Sn-Zn contour plots generated using data from the first phenomenological model 135

Figure 4-37 Cu-Sn-Zn contour plots generated using data from the second phenomenological model 137

Figure 5-1 Combinatorial electrodeposition of ternary alloys using a reel fed cathode in a Hull cell with a soluble sacrificial anode 144

Figure 5-2 Schematic of a parallel RC circuit used to model simple galvanostatic deposition 146

Figure 5-3 Schematic representation of the 64-channel electrode used in the combinatorial cell 148

Figure 5-4 Coal tar epoxy painted on the lead pattern shown in Figure 5.7-1 150

Figure 5-5 Cu foil placed over the coal tar epoxy painted glass slide with punches cut out above the electrode pads 151

Figure 5-6 Electrode pad positions printed onto Cu foil using a bubble-jet printer 152

Figure 5-7 Cu foil after the electrode positions have been punched out..... 153

Figure 5-8 Composition spread film deposited onto the coal tar epoxy painted, Cu foil masked glass slide..... 154

Figure 5-9 Lead pattern with a composition spread film electrodeposited on the pads only..... 155

Figure 5-10 EDS measurements along the punched Cu foil after deposition and removal from patterned glass slide..... 156

List of Tables

Table 1-1 Common rechargeable battery technologies 1

Table 1-2 Theoretical specific and volumetric capacities of Li, lithiated carbon and selected Li-alloy negative materials 9

Table 1-3 Cost comparison between sputter and electro-deposition 17

Table 2-1 Electrodeposition baths used to deposit films discussed in this thesis.... 37

Table 3-1 Standard electrode potentials in aqueous solution 53

Table 3-2 Description of leveling agents 58

Table 3-3 Standard hydrogen electrode (SHE) potentials and change in free energy for the electrodeposition of Cu and Sn 64

Table 4-1 List of candidates tested as the cause of anomalous behavior when electrodeposited Sn is used in a Li cell 70

Table 4-2 Cu:Sn atomic ratio determined by energy dispersive spectroscopy for electroplated deposits corresponding to the X-ray patterns presented in Figure 4-10 85

Table 4-3 Standard hydrogen electrode (SHE) potentials and change in free energy for the electrodeposition of Cu and Sn 94

Table 5-1 List of active and inactive elements (with respect to alloying with Li) that can be deposited from aqueous solution 141

List of Abbreviations and Symbols Used

γ_I	the activity co-efficient of species i in solution
η	overpotential
θ	scattering angle
λ	wavelength
μ	chemical potential
ρ	density
φ_M	potential of the metal
φ_S	potential of the solution
$\Delta\varphi(M,S)$	potential difference between the potential of the metal and solution
a_i	activity of species i
A	absorption correction
AHVIC	anomalous high-voltage irreversible capacity
A^{-z}	negative metal ion
c	speed of light
ccw	counter clock-wise
c_i	concentration of species i
C	capacitance
C_{DL}	double layer capacitance
CE	current efficiency
$[Cl^-]$	molarity of Cl^- ions

CMA	compositionally modulated alloy
combi cell	64 channel combinatorial cell
$Cu_{exchanged}$	number of Cu units exchanged
d	crystallattice spacing
DEC	diethyl carbonate
DMM	digital multimeter
e	charge of an electron
e^-	electron
E	cell potential
EC	ethylene carbonate
EDS	energy dispersive spectroscopy
$E(I)$	the potential while current flows
E_o	standard hydrogen electrode reduction potential
F	Faraday's constant
F	fluorescence
ΔG	change in free energy
GPIB	general purpose interface board
h	Planck's constant
i	current
i	species
i_{in}	number of ions entering the crystal lattice
i_o	equilibrium current density
i_{out}	number of ions leaving the crystal lattice

j	current density
K	degrees Kelvin
K, L, M	electron shells
L	distance from sample to diffracting crystal
m	mass
M	metal
M / M^{+z}	metal solution electrode interface
M_a	actual mass deposited
MA	metal salt
M_M	molar mass
M_t	theoretical deposited mass
M^{+z}	positive metal ion
$[M^{+z}]$	molarity in moles/liter
n	moles of Lithium
n	number of moles of Li transferred per mole of starting material
n	number of electrons required to reduce the aqueous ion
n	diffraction order
n_b	The fraction of electrons back-scattered from the sample
n_x	number of steps in the x-direction
n_y	number of steps in the y-direction
Ni-Cad	Nickel-Cadmium
Ni-MeH	Nickel Metal Hydride
Ox	oxidized species

[Ox]	molarity of the oxidized species
PC	propylene carbonate
PC	personal computer
PVC	polyvinyl chloride
q	charge
$-q_M$	net negative charge on the metal
$+q_S$	net positive charge in solution
R	radius
R	gas constant
RCHC	rotating cylindrical Hull cell
R_{CT}	resistance due to charge transfer
Red	reduced species
[Red]	molarity of the reduced species
SAXS	small angle x-ray scattering
SEI	solid electrode interphase
SEM	scanning electron microscopy
SHE	standard hydrogen electrode
$Sn_{exchanged}$	number of Sn units exchanged
Sn_{units}	number of Sn units
t	time
t_{Pulse}	pulse length, in time
T	temperature
T	thickness

TGA	thermal gravimetric analysis
UV	ultra-violet
V	potential
WDS	wavelength dispersive spectroscopy
XRD	x-ray diffraction
z	number of electrons
Z	atomic number
Zn_{added}	number of Zn units added
$Zn_{exchanged}$	number of Zn units exchanged
Zn_{units}	number of Zn units

Abstract

When Sn-rich electrodes are cycled in a Li cell to large voltages (> 1.4 V) anomalous high-voltage irreversible capacity (AHVIC) can be initiated. AHVIC is detrimental to the cell and should be avoided. A theory describing AHVIC is proposed that teaches ways to eliminate AHVIC. Three ways to avoid AHVIC are: 1) keep the recharge voltage below 1.3 V (vs. Li); 2) cycle the cell at a rate above about 75 mA/cm^2 and 3) by alloying Sn with another element (such as Cu).

It is shown that advanced negative electrode materials for Li-ion batteries can be made quickly, simply and inexpensively using electrodeposition. In order to investigate a wide range of alloys in a single experiment, combinatorial electrodeposition has been successfully developed and implemented. Electrodes are cut from the composition spread film and tested in Li button cells to determine which composition exhibits both high capacity and good capacity retention. Using combinatorial methods it was determined that a Cu-Sn electrode with 28 atm. % Sn satisfied these criteria.

Combinatorial electrodeposition can be applied to many binary systems. Here we look at three binary systems: Cu-Sn, Cu-Zn and Sn-Zn. Composition-spread films were deposited for each system. Composition and crystal structure varied smoothly with position for each system. Combinatorial electrodeposition can also be applied to ternary systems. The Cu-Sn-Zn system is discussed as an example.

Combinatorial electrodeposition embodies and even extends the advantages of combinatorial material science: faster, cheaper, better, simpler and scalable. Ingenuity replaces robots and million dollar machines with water guns and buckets.

Acknowledgments

This is dedicated to all my fans.

I would like to thank the administration staff (hello ladies), Alex, Simon and Andy. Thank you team Dahn-Lab. You've made my time here both productive and enjoyable. Kevin Whittingstall, Dave Stevens, Mike Fleischauer, Luc Beaulieu and Tim Hatchard have been especially helpful over the years.

I would like to acknowledge the members of my committee. Thank you Dr. Gharghouri for your guidance and help, especially after all those times I broke the SEM. Thank you Dr. Dunlap for your advice and discussions about Mössbauer spectroscopy. Thank you Jeff. Thank you for your support, generosity, patience, and dedication. Thank you for pushing me, even when I didn't want to be pushed. I owe you a burger.

Thanks to security for overlooking the numerous panty raids.

Thank you to my family for all their support. Thank you Mom, moderation in all things, thank you Dad, for not gloating when you beat me at cards, and thank you Troy, for getting caught all those times I never did.

Thank you beer, you are proof that God loves us and wants us to be happy (BF).

Thank you friends. I'll try to forget the nights I spent at school until 3 am, but I'll never forget the nights I spent at the Seahorse until 3 am. Thanks Kevin (Whoot, Ice, keV, K-man), Mike (Fleshie, Meat Packer), Tim (South Park Timmy), Jody (Dr. J), Robbie (Ram-rod), Rick (Sherminska), Amy (Rainbow), Cory (Gibby, Frenchie), Amy (what a catch) and everyone else. I did this despite your influence.

Thank you Six Flags for the Tsunami Blaster X.

Thank you Al and Janet, you're my favorite other parents. Thank you Anna. I wouldn't be here without you, and I wouldn't want to be here without you. I love you, and I look forward to the rest of our life together. See you in Burnaby.

Dahn Drone #3.14

1 Motivation

1.1 Rechargeable batteries

Rechargeable batteries are a large, rapidly growing sector of consumer electronics and communications. The three major rechargeable battery technologies in use today are Nickel-Cadmium, Nickel-Metal-Hydride and Lithium-ion. J. M. Tarascon and M. Armand compared these three competing technologies [1.1].

Table 1-1 Common rechargeable battery technologies

Technology	Discharge Voltage (V)	Specific Energy (W·h/kg)	Energy Density (W·h/L)
Nickel-Cadmium (Ni-Cad)	1.2	60	180
Nickel-Metal-Hydride (Ni-MeH)	1.25	100	300
Lithium-ion	3.75	177	475

Table 1-1 illustrates the advantages Lithium-ion (Li-ion) cells have over their older, more established counterparts. In 2003 the U.S. Li-ion battery market will likely surpass 2 billion U.S. dollars.

1.1.1 Battery terminology

What we commonly call a battery (e.g.: AA, D, C) is actually a cell. Strictly speaking a battery is a collection of individual cells, typically connected in series (e.g.: car battery). In this thesis, the terms battery and cell will be used interchangeably.

Discharge capacity, quoted in ampere-hours (Ah), is equal to the amount of charge delivered during discharge. The average voltage at which the charge is delivered defines the amount of energy in the battery, where energy is the product of total capacity and average voltage (Wh). Specific energy is the energy per unit mass (Wh/kg). Energy density is the energy per unit volume (Wh/L). Typically, researchers working on negative electrode materials don't quote their results in terms of specific energy and energy density. Instead, specific capacity and volumetric capacity are used. Specific capacity describes the capacity per unit mass (mAh/g). Volumetric capacity describes the capacity per unit volume (mAh/cc). The terms anode and cathode refer to the direction of charge transfer at the interface between the electrode and the solution; strictly speaking, the terms should be interchanged during recharging. Potential confusion is avoided by simply referring to the electrodes as negative or positive. During discharge, reduction of Lithium (Li) ions occurs at the positive electrode (e.g.: $LiCoO_2$), and oxidation at the negative electrode (e.g.: graphite). Cycling refers to repeated charge-discharge cycles. The host material may be fully, or only partially, charged/discharged during cycling. Cyclability refers to the battery's ability to perform numerous cycles without appreciable loss of original capacity. The next section will describe the basic chemistry used in a Li-based battery.

1.2 Basic electrochemistry

To understand the Li-ion battery it is useful to consider a simple Li cell, Figure 1-1.

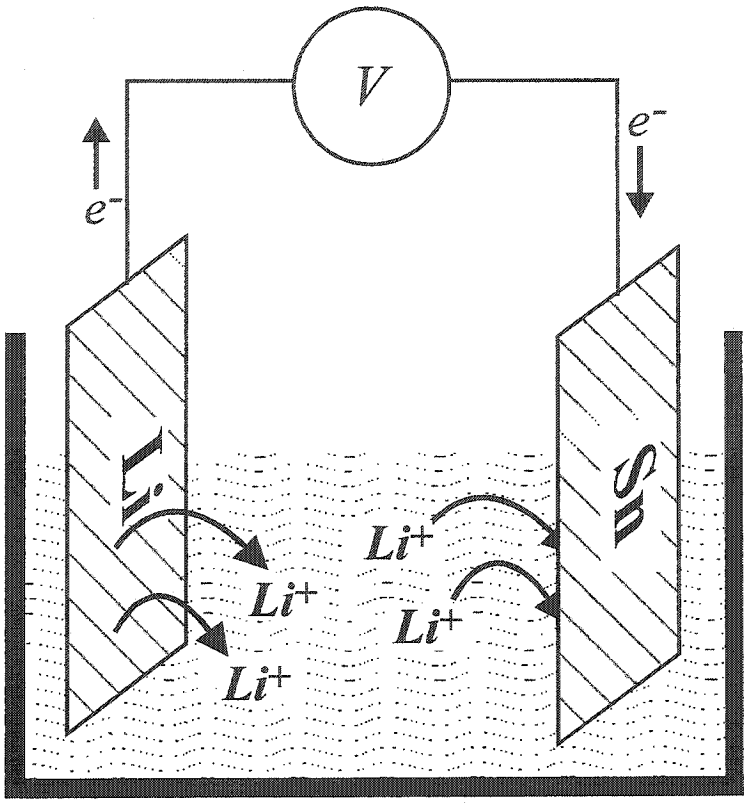

Figure 1-1 Schematic of a basic Li-Sn cell

The reaction for a cell with a negative Li-metal electrode and a positive tin (Sn) electrode is presented below. This cell will be very important to the rest of the thesis, so it is a good place to start.

The discharge of a Li-Sn cell involves two half-cell reactions:

$$nLi \rightarrow nLi^{+} + ne^{-} \qquad \text{Negative}$$

$$nLi^{+} + Sn + ne^{-} \rightarrow Li_{n}Sn \qquad \text{Positive}$$

The full cell-reaction is:

$$nLi + Sn \rightarrow Li_{n}Sn \qquad \text{Full Cell}$$

Li can react with Sn to a maximum n of 4.4 (Sn_5Li_{22}). The electrodes are immersed in a non-aqueous electrolyte, described in section 1.3.

The difference in chemical potential (μ) of Li in the negative electrode compared to the positive electrode drives the reaction. The voltage difference between electrodes is given by:

$$V = \frac{-(\mu_{POSITIVE} - \mu_{NEGATIVE})}{e} \qquad (1.2\text{-}1)$$

where e is the magnitude of the charge on an electron. To charge the cell the reactions must be reversed. Energy is required to remove Li from Sn and re-deposit it onto the negative electrode, recharging the cell.

1.3 Commercial Li-ion batteries

A typical commercial Li-ion battery uses a lithium cobalt oxide ($LiCoO_2$) positive electrode and a graphite negative electrode. Since graphite is the industry standard, new negative electrodes are compared to it. The electrodes are immersed in a non-aqueous electrolyte containing dissolved Li salt (such as $LiPF_6$). The electrolyte solvent is usually a mixture of inorganic liquids, such as ethylene carbonate (EC) and diethyl carbonate (DEC). The discharge half-cell reactions and the full cell reaction, are given below:

$$Li_yC_6 \rightarrow C_6 + yLi^+ + ye^- \qquad \text{Negative}$$

$$Li_{1-x}CoO_2 + yLi^+ + ye^- \rightarrow Li_{1-x+y}CoO_2 \qquad \text{Positive}$$

$$Li_{1-x}CoO_2 + Li_yC_6 \rightarrow C_6 + Li_{1-x+y}CoO_2 \qquad \text{Full Cell}$$

Electrode materials that have a high binding energy for Li, such as $LiCoO_2$, are referred to as positive electrodes. Materials with a low binding energy for Li, such as graphite, are negative electrodes. Figure 1-2 shows a schematic of a lithium-ion battery consisting of a carbon-based negative electrode and a Li transition metal oxide positive electrode (e.g.: $LiCoO_2$). Upon charging, lithium atoms are extracted from the positive electrode material and inserted into the negative electrode material. Upon discharging, the reverse process takes place. Hence, the basic electrochemistry of the cell involves only the transfer of lithium atoms between the two insertion electrodes. Note the layered structure of both electrodes: Li atoms effectively slide between the layers in each compound.

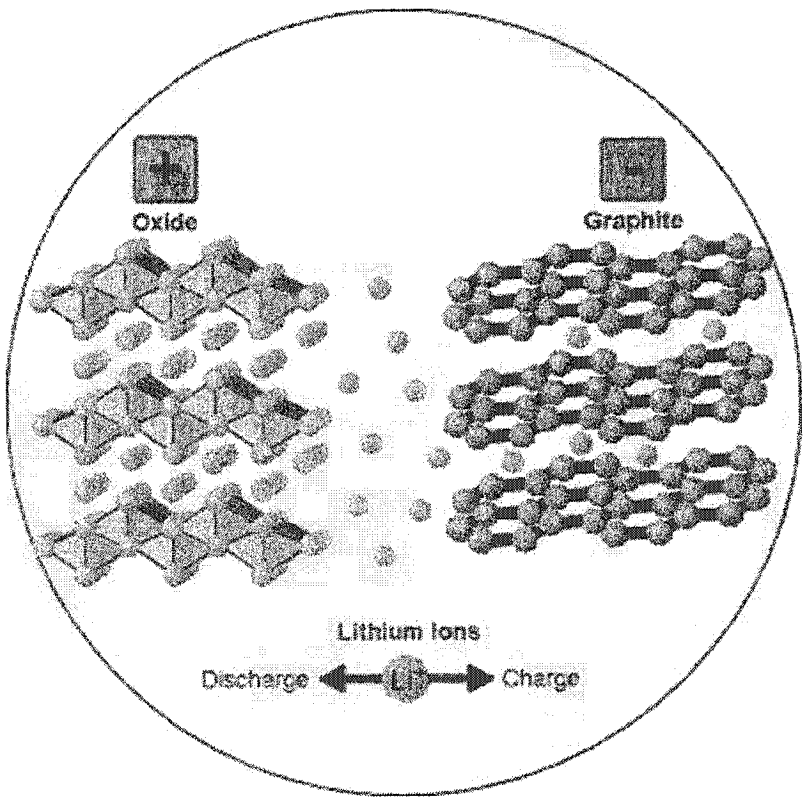

Figure 1-2 Schematic of a Li-ion battery made from a carbon-based negative electrode and a Li transition metal oxide positive electrode (from the Paul Scherrer Institute)

The work reported in this thesis used test cells with a Li-metal negative (not a Li-ion cell, but simply a Li cell) and a test material positive. This way, the variation of the voltage profile (voltage versus specific capacity) can be attributed to the test material alone, and not to a combination of both electrodes.

1.3.1 Cell geometry

The basic cell chemistry and design are the same for all types of Li-ion batteries. Figure 1-3 shows a typical cell design. Thin layers of positive (cathode), separator, and negative (anode) are rolled up on a central mandrel and inserted into a cylindrical can. The gaps are filled with liquid electrolyte. The basic design remains unchanged on substitution of one electrode material for another, although the layer thickness might change. This is the same design used for most small commercial cells, like the 18650 (18 mm in diameter, 65 mm long) used in devices such as camcorders and laptops.

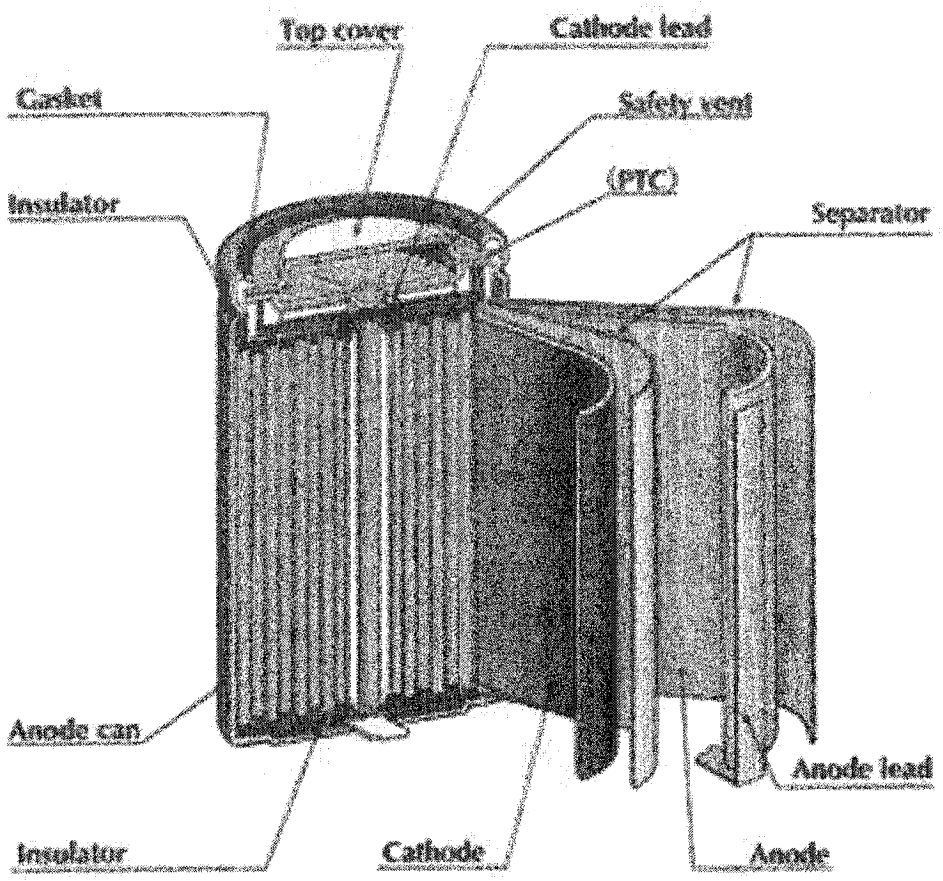

Figure 1-3 Typical design of a cylindrical 18650 cell [1.2]

1.4 Desirable characteristics of electrode materials

Graphite and $LiCoO_2$ are not the only choices for electrode materials in a Li-ion cell. Numerous replacement materials have been investigated. There are several characteristics used to compare electrode materials, such as: average voltage, capacity, and reversibility. Capacity considerations will be discussed next.

1.4.1 Capacity

Under ambient conditions, one mole of Li can react with six moles of carbon. The specific capacity of the reaction can be calculated using equation 1.4.1-1, where M is

the molar mass (e.g.: 12.011 g/mol for graphite), F is Farday's number (96485 C/mol), and n is the number of electrons transferred per mole of starting materials (e.g.: $1/6^{th}$ of an electron per mole of graphite).

$$\text{specific capacity (mAh/g)} = \frac{F \cdot 1000 \frac{mA}{A} \cdot n}{3600 \frac{s}{h} \cdot M} \qquad (1.4.1\text{-}1)$$

The volumetric capacity is easily calculated by multiplying the specific capacity by the density of the starting material. Electrode materials with high specific or volumetric capacities are desirable because they can hold more charge per unit mass or volume, making the cell lighter and smaller. Table 1-2 lists theoretical specific gravimetric and volumetric capacities (from largest to smallest) of several Li-alloy materials. These are not all the Li-alloys known, just some of the ones that would make interesting electrode materials for commercial Li-ion batteries.

Table 1-2 Theoretical specific and volumetric capacities of Li, lithiated carbon and selected Li-alloy negative materials

Alloy	Specific capacity (mAh/g)	Volumetric capacity (mAh/cc)
$Li_{4.4}Si$	4199	9784
$Li_{3.75}Si$*	3581	8344
$Li_{4.4}Sn$	994	7266
$Li_{4.4}Pb$	569	6458
Li_3As	1073	6148
Li_3Sb	660	4416
$LiZn$	410	2923
$LiAl$	993	2680
Li	3861	2062
LiC_6	372	818

** Recent results by M.N .Obrovac and T. D. Hatchard suggest Li may alloy with Si up to only 3.75 Li/Si* [1.3]

Due to the large specific capacity of Li-metal it was used in some of the first commercial Li-ion batteries. However, batteries based on Li-metal sometimes vented when heated above 120°C. When the battery is assembled, the Li-metal electrode is smooth and relatively unreactive. Cycling causes dendrites to form, significantly increasing the available reaction area. One theory describing why Li-metal based cells vent when heated above 120°C suggests that the passivating solid electrolyte interphase

(SEI, discussed in section 1.4.3-1) decomposes, exposing bare Li-metal to electrolyte, resulting in the rapid reaction of Li with electrolyte causing the cell to rapidly heat and eventually vent. This is one of the reasons that alternative electrode materials have been investigated. Although carbon has less capacity than Li-metal it is much safer, and has replaced Li-metal negatives in commercial cells. From Table 1-2 the benefits of Li-alloys over graphite are obvious, especially when volumetric capacity is considered. Average voltage considerations will be discussed next.

1.4.2 Average voltage

The voltage of a positive-negative pair is determined by the chemical potential of Li in each material. The voltage is given by equation 1.2-1. Figure 1-4 shows the binding energy of Li in various compounds [1.4]. Batteries with large energy densities are desirable, so large operating voltages are required (Energy density $= \frac{voltage \cdot current \cdot time}{volume}$). Useful positive electrode materials will have large binding energies paired with negative electrode materials of low binding energies. From Figure 1-4 the best system would be Li-metal versus F. This and other combinations are not feasible due to safety and reversibility concerns [1.5]. From Figure 1-4 coke and graphite intercalation hosts are also attractive, but as discussed above, these materials have low capacities. Metal-alloy electrodes enjoy the best of both worlds, low binding energies with high specific capacities resulting in a smaller, lighter battery with more energy.

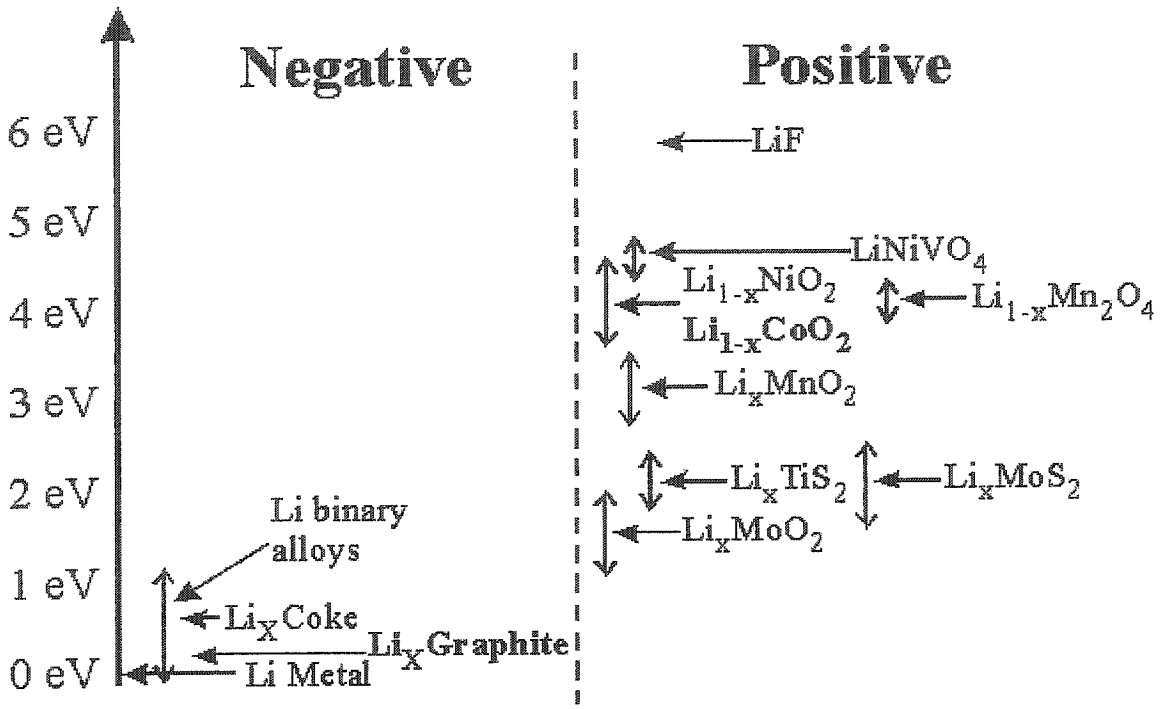

Figure 1-4 Li binding energy diagram for various compounds, quoted relative to Li metal [1.4]

Reversibility is another important characteristic of electrode materials, and will be discussed next.

1.4.3 Reversibility

Metals that alloy with Li are attractive alternatives to carbon based intercalation negative electrodes because of their large specific and volumetric capacities. However, problems arise in their cyclability. Graphite can be cycled hundreds, or even thousands of times [1.6] with a small (~20%) loss of starting capacity. Metal-alloy negatives such as Si and Sn can lose 90% of their capacity in tens of cycles. This huge loss in capacity

over relatively few cycles is unacceptable for use in consumer rechargeable battery applications. Why do metal-alloy negatives cycle so poorly?

The reaction of Li with graphite is relatively benign. When fully lithiated, one Li atom is added to every six carbon atoms. Due to varying degrees of turbostratic misalignment between adjacent layers, graphite can have a range of densities (1.9 -2.2 g/cc) [1.7]. However, crystalline graphite has a density of 2.2 g/cc [1.8]. In graphite there is one carbon atom per 10.1 $Å^3$. In LiC_6 there is one carbon atom per 11.1 $Å^3$. This results in a volume expansion of 11% [1.2]. Furthermore, the intercalation reaction mechanism is benign. Graphite consists of stacked sheets [1.9], analogous to a deck of playing cards where each card represents one sheet. When Li is intercalated the sheets are shifted by 1/3 of a unit cell along the 110 direction and the distance between sheets is increased slightly, analogous to a slightly swollen deck of cards. On removal, the graphite adopts its initial structure. Compare intercalation to the electrochemical lithiation of metal alloys, Li-Sn for example: In a fully lithiated Sn lattice, 4.4 Li are added to every one Sn atom. In the tetragonal Sn phase there is one Sn atom per 27 $Å^3$. Fully lithiated, there is one Sn atom per 96 $Å^3$. The result is a volume expansion of 256% [1.2].

More important, perhaps, are the seven inter-metallic phases of different crystallographic structure found in the Li-Sn phase diagram [1.2, or Figure 4-2]. During cycling, the composition of the Sn electrode shifts from one side of the Li-Sn phase diagram to the other and back again, undergoing numerous phase transitions from one crystal structure to another. At any given point two phases will co-exist simultaneously (except at the composition of a line phase). The transformation between phases of

different structures results in stress. The large internal stress results in pulverization. Eventually, pulverized particles become poorly connected and electrical contact is lost. When electrical contact is lost the pulverized particle cannot participate in subsequent cycles, resulting in a loss of capacity. The cracking/pulverization mechanism is cumulative. Each lithiation/delithaition cycle results in loss of capacity due to electrical isolation of particles. The capacity lost during previous cycles is rarely recovered, so the effect is cumulative. If a significant amount of capacity is lost on each cycle the cell's total capacity is quickly reduced to zero.

To understand why pieces of the electrode become electrically isolated it is important to understand the solid electrode interphase. Figure 1-5 is an oversimplified schematic describing SEI formation, cracking and resulting loss of capacity. Though oversimplified, the schematic is useful to describe the basics of capacity fade. We begin with a fresh negative electrode (Figure 1-5a), such as a sputtered or electrodeposited film. During the first discharge a passivating film known as the solid electrode interphase (SEI) is formed between the surface of the negative electrode and the electrolyte. Electrons from the current collector are supplied to the surface of the electrode. Lithium ions transferred to the surface combine with electrolyte and electrons to form the SEI (Figure 1-5b). In Figure 1-5 the electrolyte solvent is ethylene carbonate (EC). In this simplified model the decomposition products are lithium carbonate and ethylene. Refer to [1.10-15] for a thorough investigation of SEI formation and electrolyte decomposition products. Electrolyte will react with Li to a maximal thickness until electrons cannot pass through the insulating layer (Figure 1-5c). Although the SEI layer does not conduct electrons, it is an ion conductor. Electrons can no longer reach the electrolyte, instead,

Li-ions diffuse through the passivating layer and are reduced at the electrode surface (Figure 1-5d). Eventually the negative electrode becomes fully lithiated (Figure 1-5e). The cell is then recharged. Li is removed from the electrode and goes back into solution. During discharge, removal of Li causes the electrode to crack and pulverize (Figure 1-5f). New surface area is exposed. During the next discharge SEI is formed on the newly exposed surfaces. Over many charge-discharge cycles cracking and pulverization is so severe that entire particles become encrusted with the passivating layer. Since the SEI is non-conductive, the encrusted particles are electrically isolated, and therefore unable to participate in further lithiation/delithiation cycles, hence loss of capacity [1.16-19].

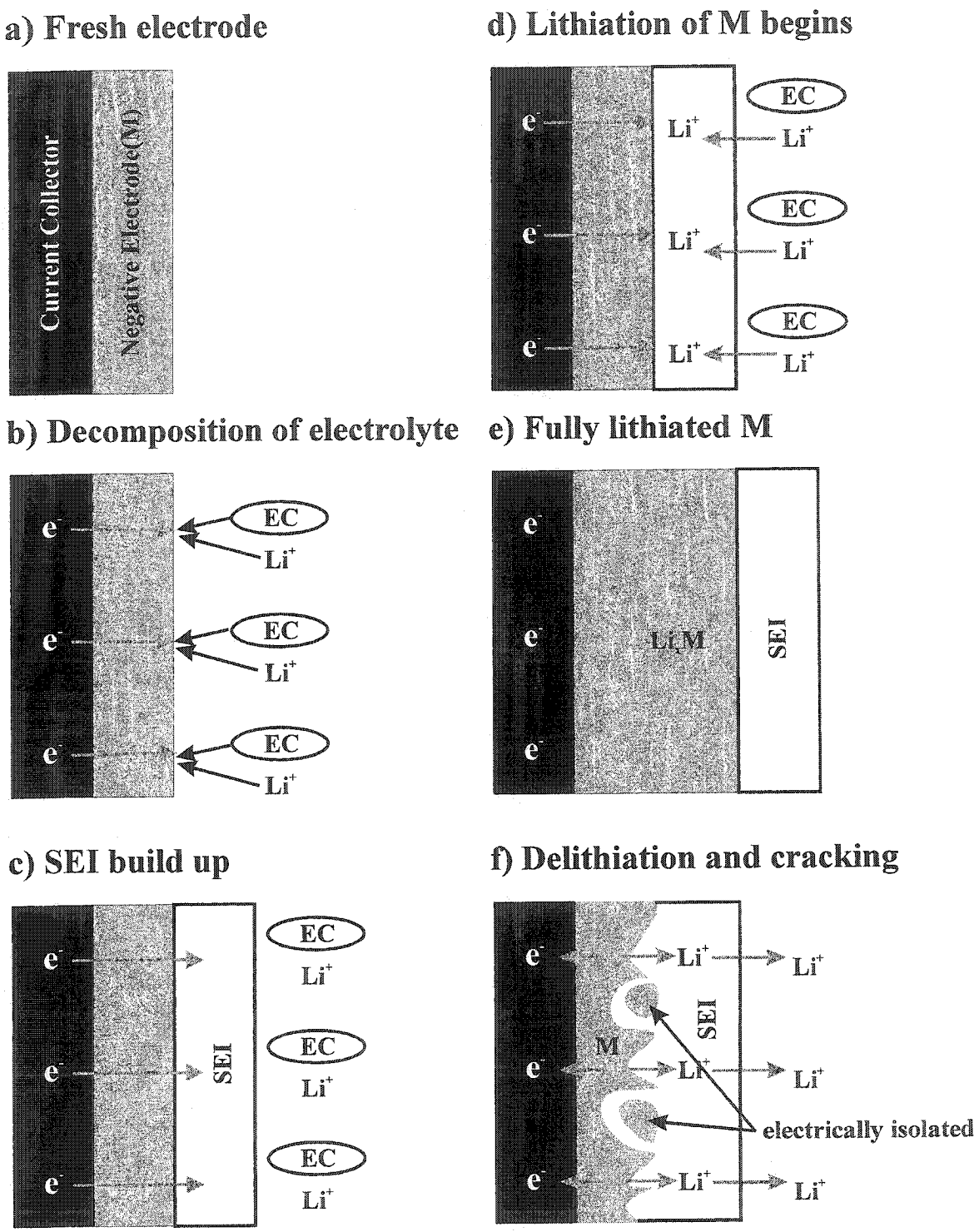

Figure 1-5 Step by step schematic of SEI formation, lithiation, delithiation and subsequent cracking resulting in electrically isolated islands of material

1.5 Nanocomposites

Courtney and Dahn [1.21-23] postulated that metal-alloys which do not show regions of co-existence between phases with mismatching lattice constants will be resistant to cracking and fragmentation, and therefore will exhibit the best cycling behavior while retaining large specific capacity. Their research was motivated when, in March 1996, Fuji Film company announced plans for the sale of a new generation of Li-ion batteries which do not use graphite as the negative electrode, but Sn oxide (incidentally this product was never brought to market). Courtney and Dahn [1.21-23] were able to show that the success of this new type of negative material was due to the presence of an inactive matrix surrounding the active material which served as an effective buffer against stress and pulverization due to volume expansion. Since co-existing Li-Sn phases have unique lattice parameters, when two distinct phases co-exist, a volume mismatch results along the grain boundary. The regions of Sn which form are kept very small (tens of angstroms) and two-phase coexistence regions between bulk Li-Sn alloys of different composition do not occur. It is the volume mismatch that causes damaging morphological changes in the electrode material. Nanostructured materials limit pulverization by virtue of small cluster size. In theory, nanostructured materials will solve the problems of pulverization while retaining large capacity for lithiation. The next section discusses how nanostructured materials are typically fabricated.

1.6 Conventional fabrication methods

Nanostructured materials can be made by a variety of methods. J. Schoonman reviews current and future fabrication methods for the production of nanostructured

materials [1.24]. Current processes used to generate nanoparticles and nanostructured materials include: chemical vapor deposition, sputter deposition, mechanical alloying, *electrodeposition*, sol-gel, and aerosol spray pyrolysis.

1.7 Advantages of electrodeposition

The most important advantage electrodeposition has over the techniques mentioned in section 1.6 is cost. Electrodeposition is an inexpensive technology with the capability of depositing bulk materials quickly and easily. A table comparing sputter deposition with electrodeposition is given below (Table 1-3). Estimated cost and time associated with depositing a Sn film, two micrometers thick on a 3 x 3" substrate is presented.

Table 1-3 Cost comparison between sputter and electro-deposition

Category	Sputter deposition	Electrodeposition*	Ratio (Sputter/Electro)
Start-up cost ($)	200000	2000	100:1
Electricity ($/kg)	40	2	20:1
Deposition time, including preparation (min)	2000	20	100:1
Cost of consumable materials ($/g)	5	0.1	50:1

based on a Sn-sulfate bath operating at 4.0 mA/cm^2

While sputter deposition may be inferior in $/kg it excels in sophistication. Exotic, technologically interesting materials can be fabricated by sputter deposition, which would be impossible with today's electrodeposition technology. These technologies, however, will share a symbiotic relationship in bringing a new battery technology to market. Sputter deposition excels in synthesis, while electrodeposition excels in production cost and speed of deposition.

2 Experimental techniques

This chapter describes the equipment and methodologies used to electrodeposit and characterize metal-alloy films.

2.1 Characterization

This section outlines the characterization techniques used.

2.1.1 X-ray diffraction

X-ray diffraction (XRD) analysis was conducted on three different diffractometers, a Siemens D5000, a homemade diffractromator called the JD2000, and an INEL CPS120. All three report scattered intensity versus scattering angle. The JD2000 and D5000 have diffracted beam monochromators while the INEL has an incident beam monochromator that limits the wavelengths striking the sample to copper (Cu) K_α. They are all equipped with Cu target x-ray tubes (λ=1.541 Å). The JD2000 and D5000 measure one sample at a time, collecting scattering intensities by moving either the tube and detector (D5000) or sample and detector (JD2000) in discrete steps and counting at each step. The JD2000 has a fixed divergence slit of 1° and a 0.2 mm receiving slit, corresponding to a footprint 1.0 cm wide and between 3.74-0.457 cm long, for an angular range of 10-90°, the typical measurement range. The D5000 has variable divergence and anti-scatter slits. Typically, 1° divergent and anti-scatter slits as well as 0.6 mm receiving slits were used. The D5000 has a foot-print (foot-print refers to the size of the beam-spot striking the sample) 1.2 cm wide, and between 4.15-0.506 cm long, in the scattering angle range of 10-90°.

The INEL has a curved position sensitive detector and an x-y measure-move translating stage enabling XRD scans to be taken anywhere within a 2 × 2″ area. The detector measures the entire diffraction pattern between scattering angles of 6° and 120°. Typically, an array of XRD patterns is taken on a user-defined grid so that changes in crystallographic structure can be studied as a function of position. This will be important when "composition-spread" films are studied. The INEL has a foot-print of approximately 1 × 1 mm^2.

2.1.2 Electron microprobe

Scanning electron microscopy (SEM) studies were performed with a fully automatic JEOL 8200 electron microprobe equipped with five wavelength dispersive spectrometers and a Noran (133 eV resolution) energy dispersive spectrometer. Images of the electroplated deposits were taken with the same microprobe.

Most of this section can be referenced to [2.1]. A heated tungsten filament thermally emits electrons, which are accelerated by a typical voltage of 15 kV. The electrons pass through a small aperture into the beam column. In the column the electrons are focused into a coherent beam using electric and magnetic fields. The beam of electrons then impinges onto the sample knocking out inner and outer shell electrons (depending on the accelerating voltage and relative electron binding energies). Binding energy refers to the minimum energy required to remove an electron in a specific electron shell from the atom. Valence or outer shell electrons replace ejected electrons, which results in a cascade of characteristic x-ray photons. This process is called x-ray fluorescence, or the generation of secondary radiation resulting from the removal of an

electron from its electronic shell. Two types of removal are possible. Of little importance for our purpose is resonance excitation, where an atom receives exactly the right amount of energy required to excite an electron from a low energy bound state to a higher one. The more important process is the removal of an electron from the atom, requiring a minimum energy equal to its binding energy. The atom will subsequently seek to regain a stable energy by reverting back to its original electron configuration. This is accomplished by higher shell electrons transferring to the vacant electron site. Such electron transitions, by virtue of the discrete characteristics of permissible shells, imply a well-defined loss of energy of the atomic system. The fundamental requirement of energy conservation is satisfied by the emission of electromagnetic radiation (x-ray) carrying an amount of energy equivalent to the energy difference between the two shells of the electron transition. The energy of the emitted electron is very close to the difference in binding energies between the electron shells [2.1].

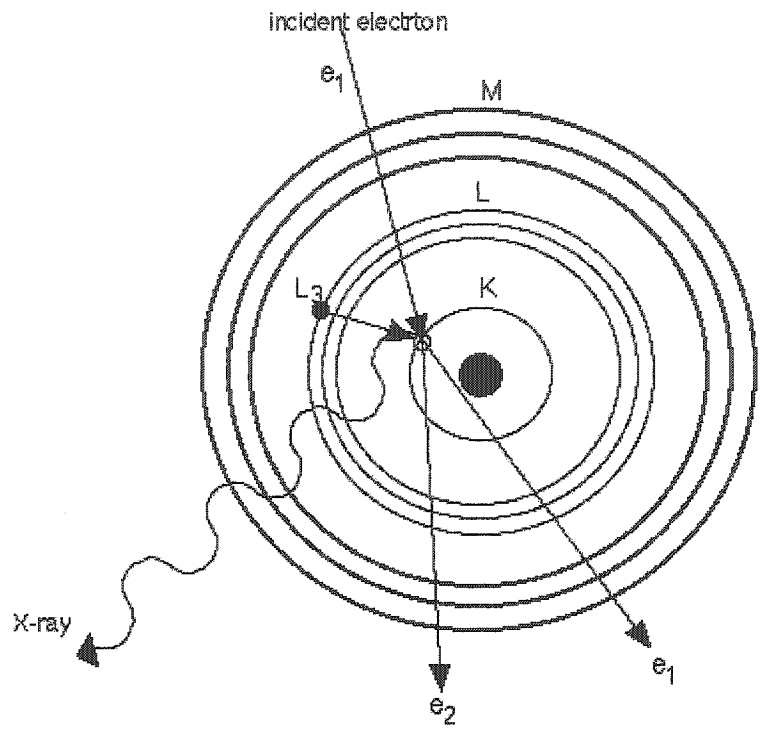

Figure 2-1 Schematic of an electron transition resulting in an emitted x-ray [2.1]

Figure 2-1 shows $K_{\alpha 1}$ x-ray emission as incident electron 1 (e1) knocks out an inner (K-shell) electron (e2) which is replaced by an L_3 electron, which triggers emission of an x-ray of energy $E_{x\text{-}ray} = E_{L_3} - E_K$. E_{L_3} corresponds to the binding energy of the electron in shell L_3, similarly, E_K corresponds to the binding energy of the electron in shell K. Figure 2-2 shows possible electron transitions that may follow electron vacancies. In Figure 2-2 binding energies of the K, L and M shells are indicated by the lines labeled K_{ab}, L_{lab} and M_{mab}, where l varies from 1-3 and m from 1-5.

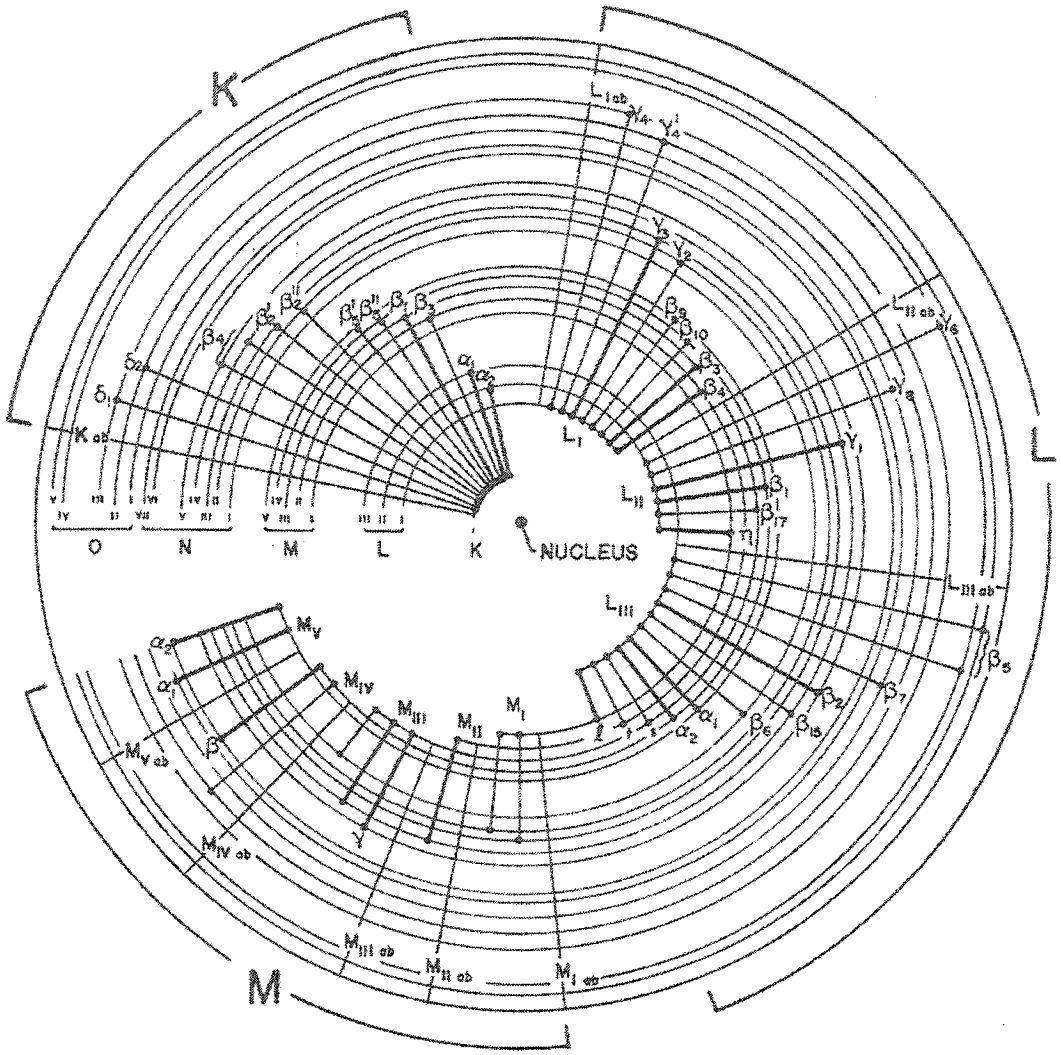

Figure 2-2 Atomic model, showing electron transitions that may follow electron vacancies. Transitions are labeled with conventional notation for associated emission lines [2.1]

The emission of electromagnetic energy may be characterized in two ways. 1) The concept of the photon characterizes the emission as a well-defined quanta of energy, like a particle. The emission is then detected based on the energy of the emitted photon; this type of spectroscopy is called energy dispersive spectroscopy (EDS). 2) Electromagnetic radiation possesses a dual character, in that it may also be associated

with an electromagnetic wave having a well-defined wavelength and speed of propagation. A simple relationship exists between the wavelength of the emitted x-ray and its energy:

$$E_{x-ray} = \frac{h \cdot c}{\lambda} \qquad (2.1.2\text{-}1)$$

where h is Planck's constant (6.6261×10^{-34} J·s), λ the wavelength and c the speed of light (2.9979×10^{8} m/s). The wavelength, rather than the energy, of the emitted x-ray can be measured. This type of spectroscopy is called wavelength dispersive spectroscopy (WDS) [2.1].

Since the energy and wavelength of emitted x-rays are determined by electron transitions, it is important to consider the various transitions allowed. Figure 2-2 shows schematically most of the electron transitions that may occur, with reasonable probability, following the creation of a vacancy (the electron transition is from the higher to the lower shell). Statistically, over a large number of such events, a vacancy will yield a characteristic emission spectrum (Figure 2-3 for example). The emission lines (energies) will bear intrinsic intensity ratios reflecting the probabilities for the associated electron transitions. These probabilities are governed by certain fundamental aspects of quantum mechanics, known as the selection rules, which will not be discussed here. The transitions shown in Figure 2-2 are labeled with the conventional notation for the emission lines. Heavy lines indicate emissions that are commonly measured in emission spectroscopy [2.1].

Now that the emission of electromagnetic radiation (x-rays) has been discussed, the next step is to describe how they are analyzed. In EDS the energies of the emitted x-rays are measured and then compared to theoretical, and/or standardized values.

Depending on the accelerating voltage, K, L and M transitions can be excited and detected. Figure 2-3 is an example of a typical spectrum.

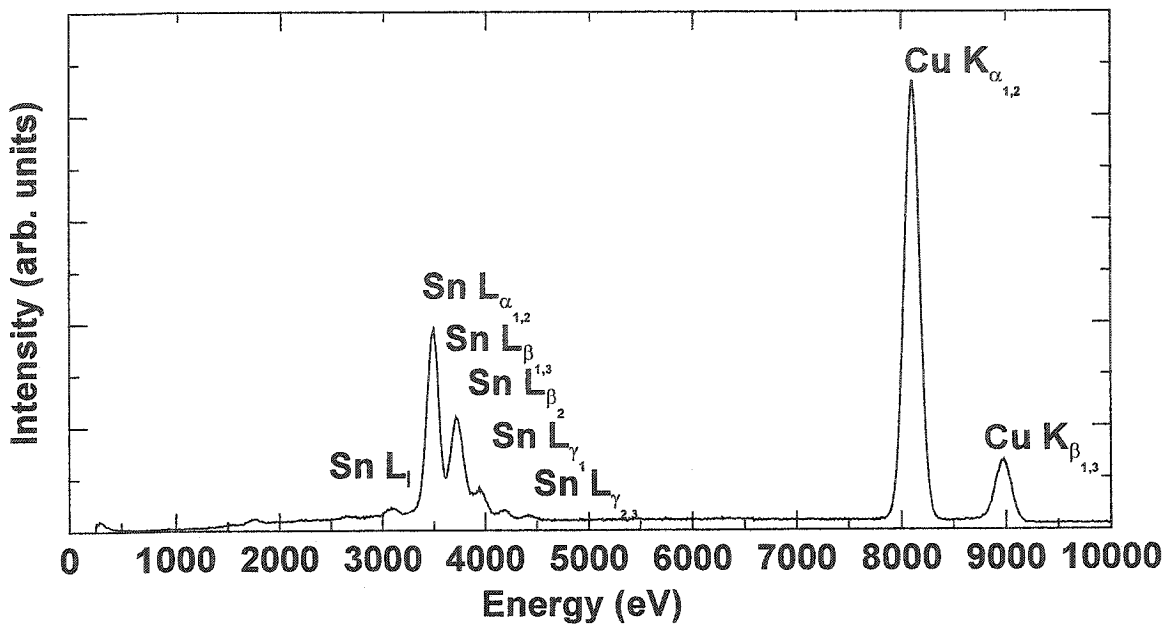

Figure 2-3 Typical EDS spectra showing peaks from Cu and Sn

The energy of an emitted x-ray depends on which atomic transition took place. Since the energies are characteristic of specific electron transitions a qualitative elemental analysis can be performed (refer to Appendix 1).

Quantitative analysis can also be performed to determine the relative quantities of elements present. ZAF corrections are applied to the measured spectra taking into account the effect of atomic number (Z), absorption (A), and fluorescence (F). All these factors contribute to the shape and intensity of lines in an energy spectrum (Figure 2-3 for example). The atomic number effect (Z) governs the amount of energy from the electron beam that enters the sample. This effect consists of two components: backscattering and electron-stopping power (or retardation). Both are a function of average Z and, to a lesser

degree, the accelerating voltage. Backscattered electrons leave the sample carrying energy without producing x-rays. The fraction of electrons back-scattered from the sample, n_b, ranges from about 0.12 for Al to 0.55 for U [2.1]. At lower Z, more electrons stay within the sample to produce x-rays.

Since x-rays are generated below the surface of the sample, the emergent radiation suffers absorption prior to detection. The absorption correction (A) is a function of the take-off angle (length of path traversed by the x-rays), the distribution of X-ray generation, the wavelength of the emergent X-ray, and the elements present. As the take-off angle increases, the intensity of characteristic radiation decreases due to an increase in path length. Less energetic x-rays are more easily absorbed. Absorption can also be strongly affected by surface irregularities; a good sample polish is thus critical. It should be noted that the electrodeposited samples could not be polished, and they did have surface irregularities. This will introduce an unknown error into the composition measurements. It is assumed that this error is not significant.

The correction for fluorescence (F) is a function of the elements present, their concentrations, mass absorption coefficients, and the take-off angle. The most important factors are the concentrations of fluorescing elements and elements fluoresced. In general, the correction for fluorescence is the least important factor in the ZAF correction [2.1].

After the ZAF correction is applied, quantitative measurements can be made. These measurements are quoted in weight or atomic %. For example, using ZAF quantitative techniques, the spectra in Figure 2-3 suggests the presence of Sn and Cu in atomic percents of 30 and 70 respectively.

In wavelength dispersive spectroscopy (WDS) the wavelengths of emitted x-rays are analyzed. X-rays from the sample impinge onto a crystal of known d-spacing and are Bragg diffracted at a specific angle. A spectrometer is placed at the diffracting angle to measure the intensity of the diffracted x-rays, shown schematically in Figure 2-4.

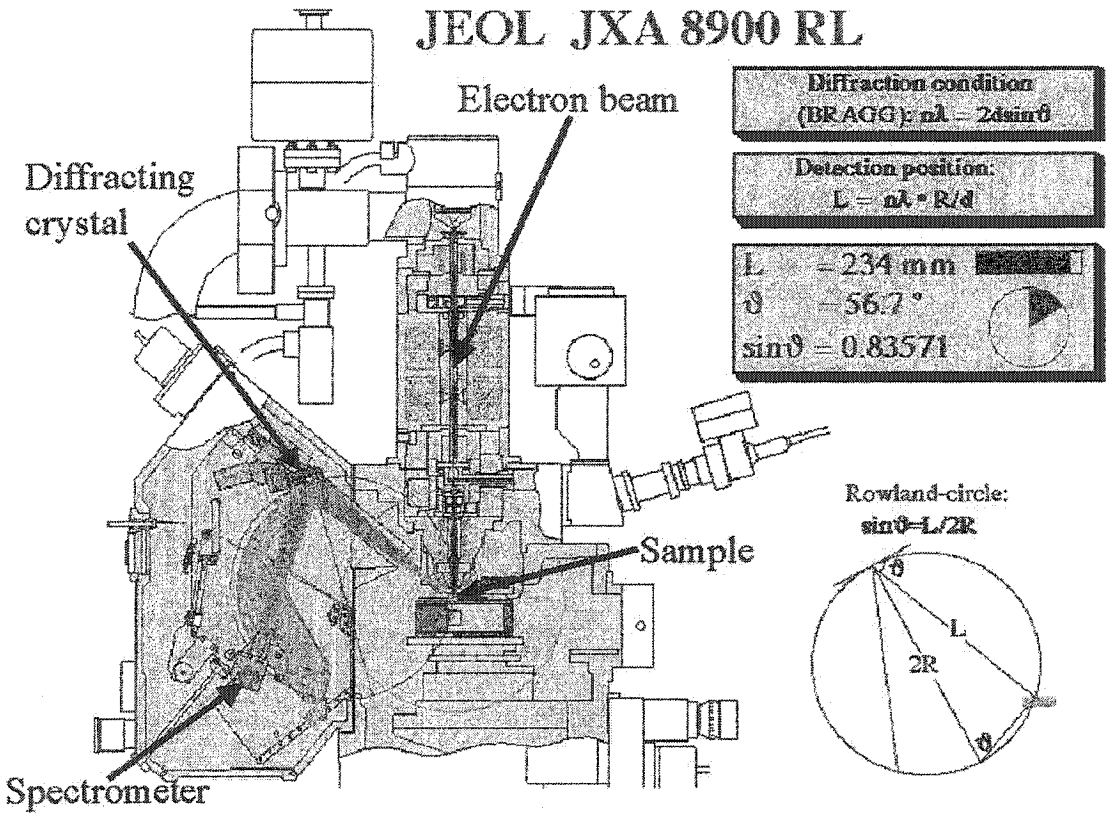

Figure 2-4 Schematic of the JEOL JXA 8900 RL electron microprobe with emphasis on the WDS detector [2.2]

Peaks are detected at various angles depending on the wavelength of the emitted x-ray. Given the d-spacing of the diffracting crystal, the Bragg scattering angle and the diffraction order, the wavelength can be calculated from equation 2.1.2-2.

$$n\lambda = 2d \cdot \sin\theta \qquad (2.1.2\text{-}2)$$

where n is the diffraction order (typically 1), λ the wavelength, d the lattice or d-spacing and θ the scattering angle. The wavelength of the emitted x-ray is characteristic of a particular atomic transition, and usually can be attributed to a specific element. However, a given scattering angle may not correspond to a unique atomic transition, especially when second order reflections are considered.

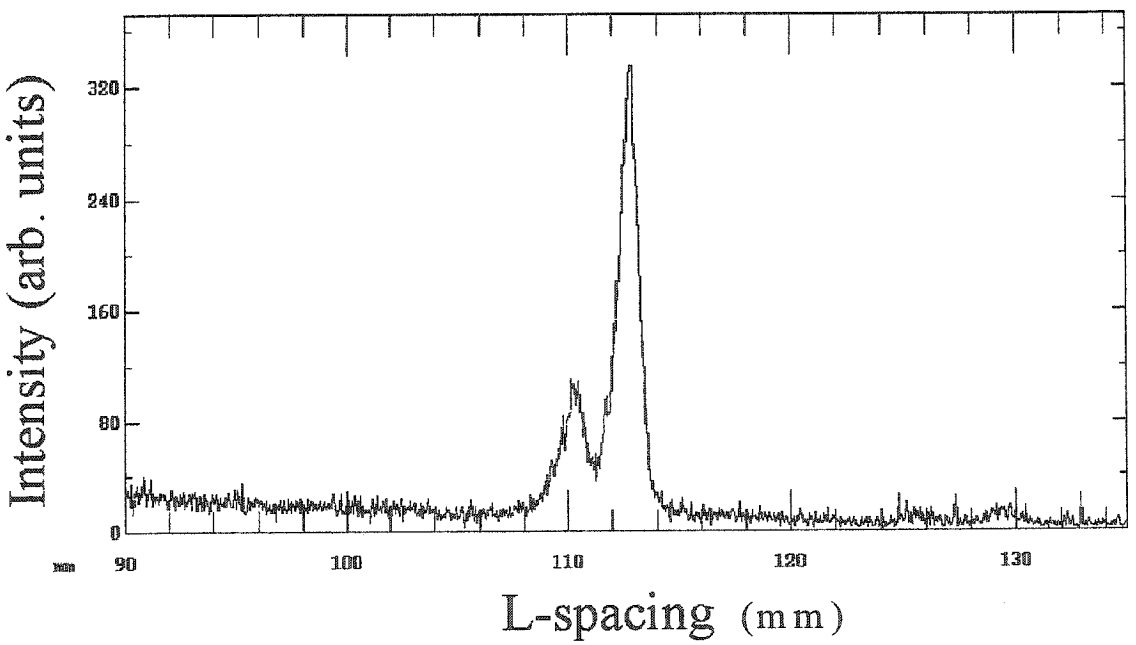

Figure 2-5 Sample WDS spectra in terms of L-spacing for a pure Zn sample

Figure 2-5shows a graph of intensity vs. L-spacing, which is similar to 2θ for XRD, while analyzing a sample for zinc (Zn) and O content. L-spacing is defined in Figure 2-4, where L depends on the radius of the Rowland circle used in the WDS equipment, and is therefore machine specific (JEOL JXA 8900 RL in this case). Equation

2.1.2-3 (also given in Figure 2-4) shows how to calculate the L-spacing where n is the diffraction number, λ is the wavelength of the incident x-ray, R is the radius of the Rowland circle (defined by machine specifications) and d is the lattice, or d-spacing of the diffracting crystal.

$$L = n\lambda \cdot \frac{R}{d} \qquad (2.1.2\text{-}3)$$

The software used to analyze the spectra in Figure 2-5 searches for an O (oxygen) peak at 110.227 mm, corresponding to the theoretical position of the K_α transition in O [2.3]. In Figure 2-5 there are two peaks near 110.227 mm, the software chooses the largest peak closest to 110.227 mm (~112.3 mm) as the characteristic K_α O peak and calculates the relative O content from there. This results in an error. There is little or no O in this particular sample. The peaks in Figure 2-5 arise from two second order reflections of characteristic x-rays from Zn, corresponding to the $L_{\alpha_{1,2}}$ (expected at 114.371 mm) and L_{β_1} (expected at 111.841 ,mm) transitions [2.3]. This particular problem was encountered during our studies. When WDS was used to analyze a sample for both O and Zn, the analysis would consistently report abnormally large O and low Zn concentrations. Given a pure Zn sample WDS analysis would report over 30 at.% O and only 70 at.% Zn. Understanding these types of phenomena is crucial when using WDS.

Note that the theoretical positions of the Zn $L_{\alpha_{1,2}}$ and L_{β_1} lines do not line up with the experimentally obtained spectra in Figure 2-5. This could be due to mechanical drift or other experimental inconsistencies. Due to these systematic errors the microprobe is

usually calibrated with respect to known standards to define the proper, experimental positions of x-ray peaks, rather than relying on the theoretical values.

These considerations are important to understand when using WDS. Previous knowledge of the sample's constituents (using XRD for example) will help avoid such errors.

2.1.3 Electrochemical testing

The electrochemical characterization of a material is a three-step process: electrodeposition of test negative electrode material, cell fabrication, and electrochemical testing. These steps will be discussed next. Electrodeposition of test negative electrodes will be discussed in section 2.2. Once the film is made, small circular disks 0.5″ in diameter are punched, weighed, and taken into an inert atmosphere glove box for cell construction.

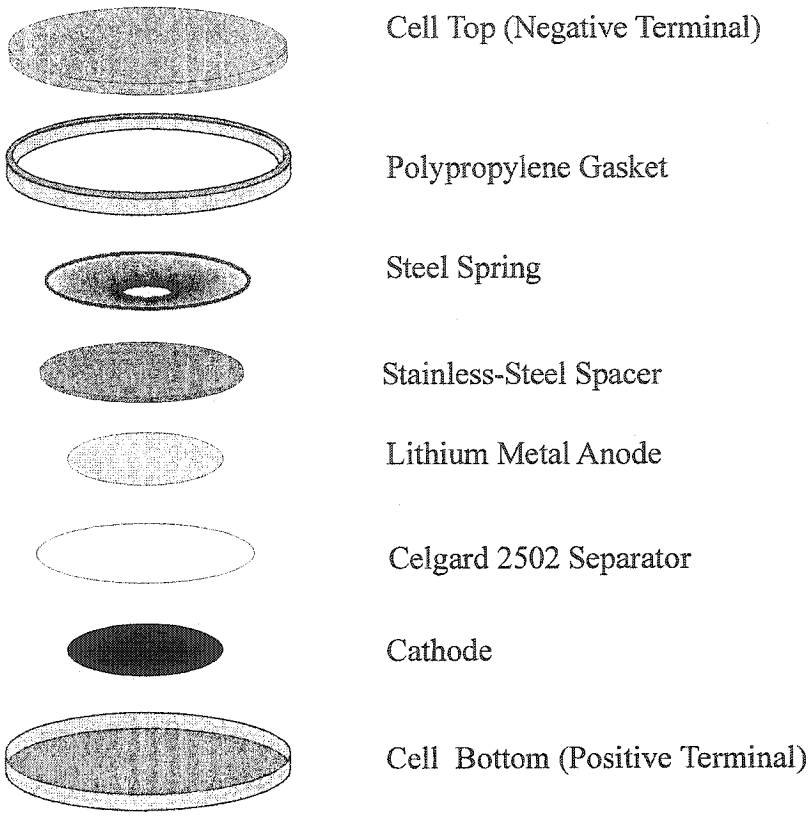

Figure 2-6 Exploded view of a coin cell [1.5]

Figure 2-6 shows an exploded view of a coin cell. The test negative electrode material (labeled cathode in Figure 2-6) is placed on the stainless-steel cell bottom (2325 coin cell hardware – 23 mm outer diameter and 2.5 mm thick) and wetted with a few drops of electrolyte (1 M $LiPF_6$ dissolved in a 1:2 vol % mixture of ethylene carbonate (EC) and diethyl carbonate (DEC), Mitsubishi Chemical). A microporous polypropylene separator (Celgard 2502) is set on top of the test negative electrode. Next, a 14 mm-diameter, 125 μm-thick lithium foil disk is placed on top of the separator and centered with respect to the test negative electrode. A stainless steel spacer disc is placed on top of the lithium. A cone-shaped mild-steel spring is placed next. When the cell is sealed, the cone-shaped spring is compressed and applies force to the cell bottom and spacer disk,

which keeps the electrodes under stack pressure (approximately 200 psi). Finally, a stainless-steel cap, which has a polypropylene gasket along its circumference, is placed onto the stack. The cell is then crimped closed. The sides of the can fold over onto the gasket and seal the cell. The cell is taken out of the glove box and stainless-steel tabs are spot-welded to the top and bottom of the coin cell. The tabs are connected to the charger by alligator clips and wires.

Note that when the test negative electrode is cycled in the configuration above it is actually the positive electrode. Li foil is the negative electrode. Figure 1-4 shows a Li binding energy diagram for various compounds quoted relative to Li metal. The electrode with the largest Li binding energy is the positive electrode. Similarly, the electrode with the lowest binding energy is the negative electrode. In a commercial cell $LiCoO_2$ is the positive electrode and carbon is the negative electrode (refer to Figure 1-4). However, during testing it is convenient to use Li as the counter electrode, making it the negative electrode and any test electrode material (i.e.: Sn) the positive electrode. By convention, an electrode material is given the sign it would have if it was in a commercial Li-ion cell, so Sn-based compounds are called negative electrode materials.

The currents chosen for charge and discharge are based on the active electrode material. The active mass is calculated by subtracting the total mass of the disk from the mass of the substrate and then multiplying by the percent composition of active material (e.g. 50% given a Cu-Sn alloy with a compositional atomic ratio of 1:1). Cells were typically cycled at a C/10 or C/20 rate, meaning 10 or 20 hours per charge or discharge, corresponding to ~100-200 $\mu A/cm^2$.

The cells are housed in temperature controlled environments (30.0 ± 0.1°C) and connected to a computer controlled charger system (E-One Moli Energy Canada Ltd., Maple Ridge, B.C.). The charger system measures voltage versus time. The voltage measurement is made by a Keithley 196 digital multi-meter (DMM), which has 6.5 digit precision. The charger system operates in constant current mode, discharging and recharging the cells to pre-set voltage limits. Voltage limits were typically set between 0 and 1.6 V, although voltage limits as low as 0-0.8 V and as high as 0-3.0 V were also used.. The system maintains a constant current (to within 1 μA) during charge and discharge.

The discharge capacity can be calculated from the data that the charger logs, as follows:

$$\text{discharge capacity (mAh/g)} = \frac{-i \cdot t}{m} \qquad (2.1.3\text{-}1)$$

where i is the current in mA, t the time in hours and m the active mass in grams. Data were logged with 10 μV precision whenever the cell voltage changed by 5 mV or more and time is measured to the nearest second. The lower voltage-trip chosen for discharge was between 0 V and 0.3 V, and the upper voltage-trip chosen for charge was between 0.8 V and 3.0 V. The specific voltage ranges chosen for the discharge and charge of a particular cell will be provided in subsequent chapters.

2.2 Electrodeposition

The equipment and software used to electrodeposit metal-alloy films are discussed below.

2.2.1 Instrument

A Keithley 236 source/measure unit was used to control all electrodeposition experiments.

2.2.2 Software

This section discusses software developed to perform pulse plating, a key concept in the rest of the thesis. Refer to sections 3.9 and 4.4.1 for a complete discussion of pulse plating. A Visual Basic program was written to apply user-defined pulsed waveforms to an electroplating cell (refer to section 2.2.4) using a Keithley 236. Commands were sent to the Keithley using a GPIB card in a PC. Voltage, current and time measurements were recorded on the PC. The pulsed waveforms used are current modulated, so the Keithley operated in "source I-measure V" mode.

A database of half-cell reactions was tabulated containing density, molar mass and oxidation number for a variety of elements capable of aqueous deposition. Pulsed deposition was performed in a bath containing at least two elements, X and Y. Species X was present in low concentration and deposited more readily (higher reduction potential) than species Y, which was present in high concentration.

The wave-form was built from six user-defined parameters: i) deposition current for species X, ii) deposition current for species Y, iii) thickness per pulse for species X,

iv) thickness per pulse for species Y, v) deposition area and vi) total number of cycles. One cycle consists of X and Y pulses. Once X and Y were selected, these parameters, coupled with the elemental properties in the database were used to build the waveform. In addition, the following calculations were made: time per X/Y pulse, mg of X/Y plated per pulse, mC passed per X/Y pulse, total thickness, X/Y current density and total deposition time. Typically, wave pulses such as the one in Figure 2-7 were used, where the deposition current of species X is zero. The electroplating strategy will be discussed in section 4.4.1. The maximum current supplied by the Keithley 236 is 100 mA.

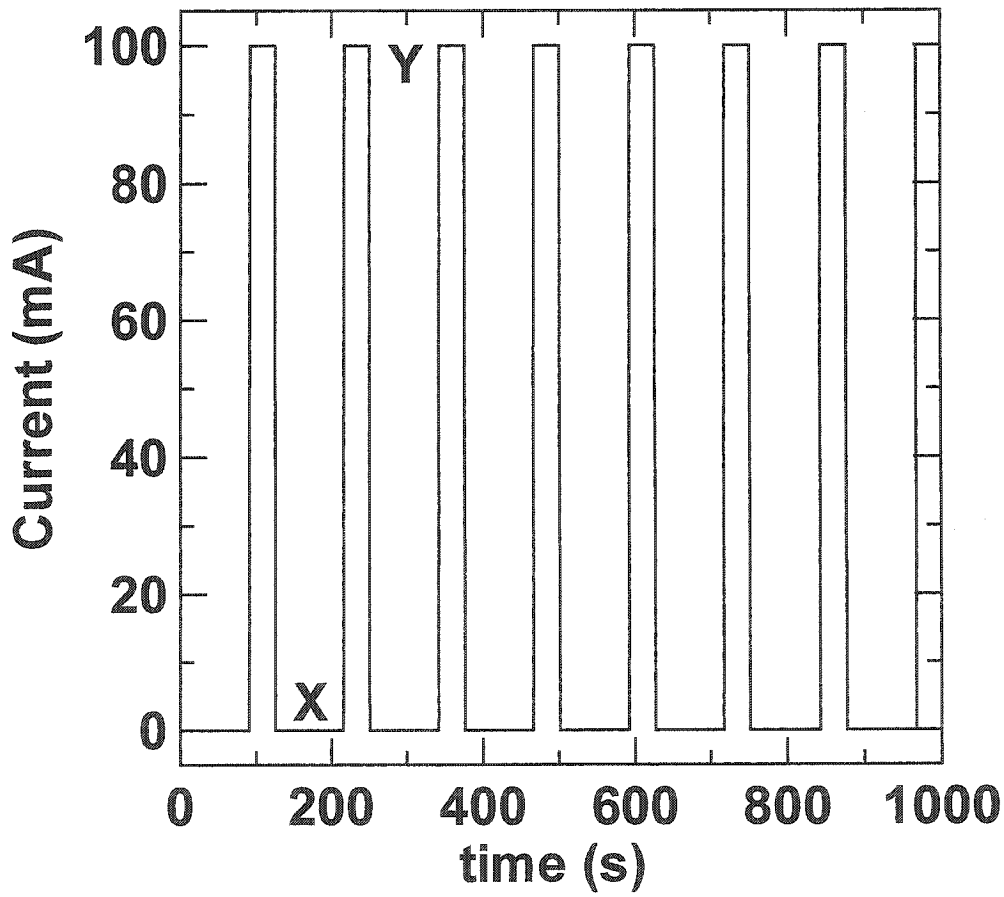

Figure 2-7 A typical pulsed waveform using a zero mA X pulse and 100 mA Y pulse

2.2.3 Plating baths

The simplest electrodeposition bath consists of a source of metal ions and a solvent; Cu sulfate in water for example. If deposition were performed in such a bath the deposit would be powdery, non-adherent, and rough [2.4]. One of the reasons the film forms this way is poor ionic conductivity of the bath. Typically, a supporting salt is added to the bath to increase ionic conductivity. The supporting salt often has the same anion as the metal source, which actually decreases the solubility of the metal source, so the metal ion source should be readily soluble in water.

Sometimes leveling agents (discussed in section 3.8) are also added. Certain characteristics of electrodeposited films, such as surface roughness and brittleness, are highly dependent on the type of bath from which they are deposited [2.4]. For example, electrodeposited Sn tends to cluster, resulting in dendritic, tree-like structures rather than a smooth film. If proper leveling agents are added to the bath, the resulting film is smooth, shiny and fully covers the substrate.

When a bath is unable to deposit films that completely and evenly cover a substrate they are said to have poor throwing power. Conversely, a bath with good throwing power produces films with uniform coverage and thickness despite macroscopic irregularities on the substrate [2.4]. Poor throwing power baths will be exploited to obtain composition-spread films discussed in section 4.4.

For simplicity, only aqueous deposition baths were used, presented in Table 2-1. The simplified function of each ingredient is indicated in the right column. Proprietary ingredients are not discussed since little is known about them. Deposition was performed at room temperature with no agitation.

Table 2-1 Electrodeposition baths used to deposit films discussed in this thesis

Bath Name	Constituents	Function
Sn Sulfate	60 g/L $SnSO_4$	Metal source
	40 g/L H_2SO_4	Increase conductivity
	2 g/L Gelatin	Levelling
	1 g/L β-Naphthol	Levelling
E-Brite (Sn)	20 mL/L 180-M	Levelling
	7.5 mL/L 180-B	Levelling
	24 g/L $SnSO_4$	Metal source
	100 mL/L H_2SO_4	Increase conductivity
SnTech	150 mL/L SnTech Acid Concentrate	Increase conductivity
	67 mL/L SnTech Tin Make-Up	Metal source
	40 mL/L SnTech Additive A	Levelling
	20 mL/L SnTech Additive B	Levelling
Sn Pyrophosphate	36 g/L $Sn_2P_2O_7$	Metal source
	137 g/L $K_4P_2O_7$	Increase conductivity
	0.3 g/L Gelatin	Levelling
Bronze 1	150 mL/L SnTech Acid Concentrate	Increase conductivity
	67 mL/L SnTech Tin Make-Up	Metal source
	40 mL/L SnTech Additive A	Proprietary
	20 mL/L SnTech Additive B	Proprietary
	4 g/L $CuSO_4 \cdot 5H_2O$	Metal source
Bronze 2	36 g/L $Sn_2P_2O_7$	Metal source
	137 g/L $K_4P_2O_7$	Increase conductivity
	0.3 g/L Gelatin	Levelling
	1g/L $Cu_2P_2O_7 \cdot 3H_2O$	Metal source
Brass	3.2 g/L $CuSO_4 \cdot 5H_2O$	Metal source
	86.4 g/L $ZnSO_4 \cdot 7H_2O$	Metal source
	218 g/L $K_4P_2O_7$	Increase conductivity
Sn-Zn	3.8 g/L $Sn_2P_2O_7$	Metal source
	54 g/L $ZnSO_4 \cdot 7H_2O$	Metal source
	218 g/L $K_4P_2O_7$	Increase conductivity

The SnTech bath is a proprietary product from Lucent technologies. SnTech acid concentrate is simply methane sulfonic acid of unknown molarity; SnTech Tin make up is 300 g/L Sn^{+2} stannous methane sulfonate in methane sulfonic acid, again of unknown molarity. SnTech additives A and B are unknown except that they contain isopropyl alcohol.

2.2.4 Electroplating cells

Two different electroplating cells were used, a Hull cell and a parallel electrode cell. The Hull cell design is slightly modified compared to the one discussed in [2.5]. The cell discussed here was made from polyvinyl chloride (PVC), and a schematic is given in Figure 2-8a (cross section). The cell is 7.5 cm wide and 6.9 cm tall. The working electrode is inclined at ~50° with respect to the counter electrode. The counter electrode is 7.3 cm wide. The closest approach of counter electrode to working electrode is 1.0 cm, and the furthest separating distance is 9.0 cm. The oblique angled working electrode is 11.0 cm long. The cell has a volume of approximately 250 mL. A parallel electrode cell was also used, (Figure 2.8b, side view) measuring 8.2 × 5.0 × 6.7 cm (approximately 250 mL). The working and counter electrodes were separated by 5.0 cm.

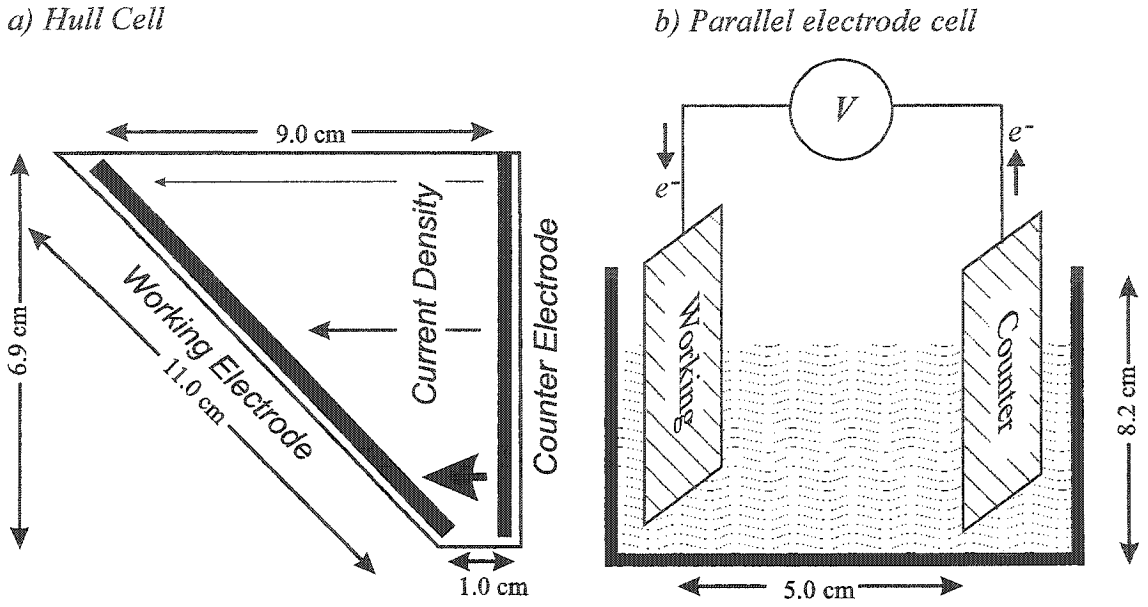

Figure 2-8 Two electroplating cells used to deposit metal-alloy films

Note that a reference electrode was not used in any of the deposition experiments. Reference electrodes are typically used to study potential changes in the working electrode. We were not concerned with this change in potential, only that the potential was low enough to deposit the species of interest. Furthermore, understanding the variation in potential can be quite complicated. During deposition there could be numerous processes occurring at the working electrode that affect the potential. Some examples are: i) reduction of metal ions; ii) miscellaneous side and partial reactions, such as H_2 evolution; iii) a local change in pH near the electrode due to processes like H_2 evolution; iv) rapid depletion of metal ions near the electrode establishing a concentration gradient, v) hindrances due to mass or charge transport and vi) crystallization [2.4]. These processes cause the actual deposition potential to be different from the equilibrium reduction potential. The difference between the equilibrium reduction potential (E_o) and the actual deposition potential when current (i) is flowing ($E(i)$) is called the over

potential (η) [2.6-7]. The relationship between E_o, $E(i)$ and η is given below in equation 2.2.4-1:

$$E(i) = E_o + \eta \qquad 2.2.4\text{-}1$$

For example, a potential of 0.1 V vs. SHE (refer to section 3.2) may be required to reduce Cu^{+2} to Cu, rather than the theoretical reduction potential of 0.342 V. The concept of overpotential will be discussed again in section 3.6.

Due to the complicated nature of the overpotential we focused on controlling the current, rather than the potential. Typically, the desired thickness of the deposited film was specified. Then, given a constant current, it was trivial to determine deposition time. Note that a current efficiency of 100% is assumed during calculations, which is certainly wrong, but previous studies of the species of interest suggest plating efficiencies near 90-95%. Current efficiency (CE) is easily calculated since there is a simple relationship between current passed and mass deposited:

$$CE = 100 \cdot \frac{M_a}{M_t}\% \qquad (2.2.4.1)$$

where M_a is the mass actually deposited and M_t the theoretical mass calculated using Faraday's law. Current efficiency is expressed in percent.

2.2.5 Cleaning, substrates and plater's tape

Nickel or Cu foil was used as the working electrode. The foil, PVC vessel, and counter electrode were wiped with acetone, ethanol and then methanol prior to deposition. 3M Plater's tape was used to secure the foil to the PVC backing around the immersed edges to prevent deposition on the back of the foil. Note that the Plater's tape

slightly decreased the available area for deposition. In the modified Hull cell the usable area is decreased from 11.0 × 7.3 cm to approximately 10.8 × 7.1 cm. In the parallel electrode cell configuration the usable area is decreased from 8.2 × 6.7 cm to approximately 8.0 cm × 6.5 cm.

2.3 Sputter deposition

Sputtered films were prepared by Tim Hatchard using DC magnetron sputtering (Corona Vacuum Coaters V-3T system with 2″ diameter targets). Using a 500 L/s turbo pump and a Polycold system, the ultimate base pressure of the system is $6 \cdot 10^{-8}$ Torr. One micrometer thick Sn films were deposited on 100 μm thick Cu foil corresponding to 0.731 mg/cm^2. Sputtering was done using an argon pressure of 2 millitorr and a power of 50 W. The target-substrate distance in the sputtering system is 55 mm.

2.4 Preparation of powdered Sn electrodes

A slurry is prepared from Sn powder (Aldrich - 10 mesh, 99.85 %), polyvinylidene fluoride (PVDF) (Aldrich) and "Super S" carbon black (Chemetals, USA). PVDF is added at 10% the mass of the Sn powder and carbon black is added at 5% the mass of the Sn powder. The PVDF is dissolved in N-methly pyrrolidineone (NMP) (Aldrich). The slurry is mixed together with ceramic mixing beads and shaken vigorously for 15 minutes. The slurry is then coated onto thin (125 μm thick) copper foil with a typical mass loading of 5-15 mg/cm^2 and allowed to dry. The NMP evaporates leaving a film of approximately 85% by weight Sn powder, 10% carbon black and 5% PVDF.

3 Theory of electrodeposition

Electrodeposition was discovered by Luigi V. Brugnatelli in 1805. Despite almost 200 years of experience, modern day practitioners lack an in-depth understanding of the deposition process. Most of this chapter can be referenced to [2.4].

3.1 Electrode/solution interface potentials

When metal M is immersed in an aqueous solution containing M^{+z} ions there will be an exchange of ions between the solution and metallic phase (e.g.: when a Cu electrode is placed in an aqueous $CuSO_4$ solution, Cu^{+2} ions are exchanged). Figure 3-1 is a schematic representation of the ion exchange.

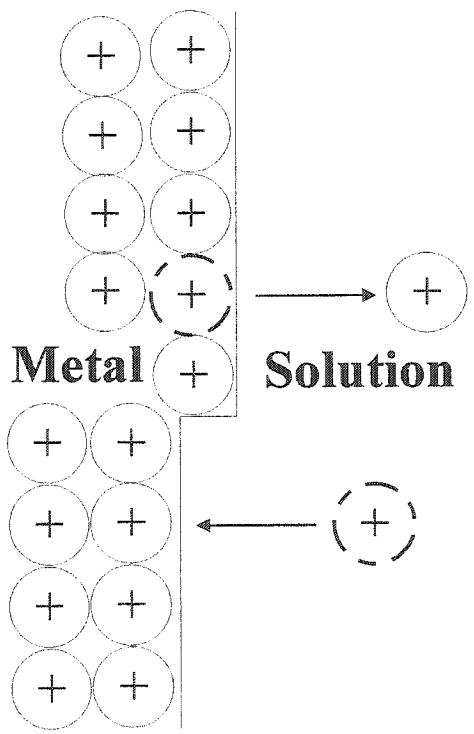

Figure 3-1 Metal-solution interface

Initially one of these reactions may occur faster than the other. Assume more M^{+z} ions leave than enter the crystal. There is an excess of electrons on the metal so it acquires a negative charge per unit area $(-q_M)$. Similarly, there is an excess of positive ions in solution. In response to the charging of the metal there is a rearrangement of ions in solution. The negative charge on the metal attracts positively charged M^{+z} ions from solution while repelling negatively charged ions. For example, given a metal salt, *MA*, the M^{+z} ions are attracted by the metal and the A^{-z} ions are repelled. The result is an excess of positively charged M^{+z} ions close to the metal/solution interface. Given the net negative charge on the electrode $(-q_M)$, the solution must acquire an equal and opposite charge $(+q_S)$. The positive charge at the solution side of the interface slows the rate of M^{+z} leaving the crystal lattice (due to repulsion) and accelerates the rate of ions entering the crystal (due to increased concentration). In time a dynamic equilibrium between metal *M* and its ions in solution (M^{+z}) is established:

$$M^{+z} + ze^{-} \Leftrightarrow M \qquad (3.1\text{-}1)$$

where *z* is the number of electrons involved in the reaction. At dynamic equilibrium, an equal number of ions leave and enter the crystal lattice per unit time, that is $i_{in} = i_{out}$. The equilibrium exchange of ions in and out of the metal is called the equilibrium exchange current density [3.1], i_o, which reflects the kinetic properties of a particular interfacial system, and varies from one reaction to another and therefore from one electrode to another. The equilibrium exchange current density cannot be measured directly since there is no net flow of charge, however, it can be measured indirectly.

The interface region is electrically neutral at equilibrium:

$$q_M = -q_S \tag{3.1-2}$$

Charging of the interface results in a potential difference, much like charging a capacitor $(q = C \cdot V)$. $\Delta\varphi(M,S)$ is the potential difference between the potential of the metal, φ_M, and solution, φ_S, where:

$$\Delta\varphi(M,S) = \varphi_M - \varphi_S \tag{3.1-3}$$

The potential difference between a single solution/metal interface cannot be measured directly. To determine the potential difference another metal/solution interface is required. By connecting two metal/solution interfaces an electrochemical cell is formed. A potential difference can be measured across the cell that is the sum of the metal/solution interface potentials for each electrode. Since only potential differences, not individual potentials, can be measured, it is convenient to define a reference electrode and measure cell potentials relative to that. The standard hydrogen reference electrode will be discussed next.

3.2 Standard hydrogen reference electrode

Any electrochemical cell could be constructed to measure the combination of two metal/solution interface potentials. By convention, these potentials are measured relative to a standard hydrogen electrode (SHE), illustrated in Figure 3-2.

The standard hydrogen electrode is ascribed a zero potential by convention. The measured value of the potential difference of the cell in Figure 3-2 is 0.342 V. This potential is called the relative standard electrode potential of Cu and is denoted E_o. The standard electrode potential of other metal/solution (M / M^{+z}) electrode interfaces is

obtained in a similar way, by forming a cell consisting of the standard hydrogen electrode (SHE) and the M / M^{+z} electrode under investigation.

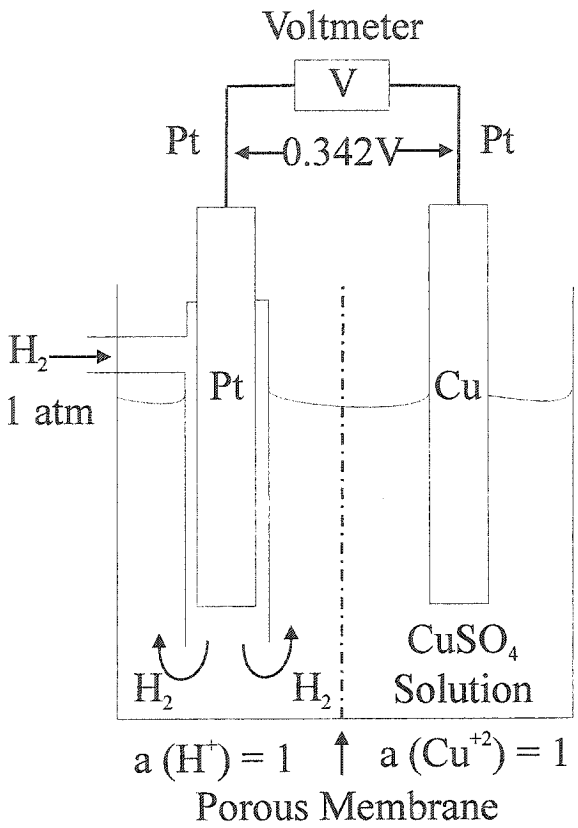

Figure 3-2 Standard hydrogen reference electrode

The potential, V, of the M / M^{+z} electrode interface is a function of the activity of metal ions in solution. The definition of the activity co-efficient (γ_i) of species i is given by the following equation:

$$\gamma_i = \frac{a_i}{c_i} \tag{3.2-1}$$

where c_i is the concentration in moles per liter and a_i is the activity of species i in solution. The activity co-efficient of species i is a dimensionless quantity that depends

on the concentration of all ions in solution. A thorough examination of ionic activity and its role in determining M/M^{+z} electrode interface potentials will not be attempted here. Instead, the low ionic concentration limit (<0.001 Molar) in which ionic activity is equivalent to ionic concentration in moles per liter, will be used. By considering cell reactions and changes in free energy the Nernst equation can be derived. In the formalism of low ionic concentration the Nernst equation is used to determine the potential, E, of the M/M^{+z} electrode interface as a function of concentration:

$$E = E_o + \frac{RT}{zF}\ln[M^{+z}] \tag{3.2-2}$$

where, R is the gas constant, T is the absolute temperature, E_o is the standard potential relative to SHE, M^{+z} is the molarity in moles/liter, z is the number of electrons involved in the reaction and F is Faraday's constant. $\frac{RT}{F}$ has the dimensions of volts and at 298 ^{o}K (25 ^{o}C) equals 0.0257 V.

3.3 RedOx potentials

RedOx (Reduction-Oxidization) electrode potentials are the result of an exchange of electrons between metal and electrolyte. In the previous section metal/metal-ion electrode potentials resulted from an exchange of metal ions between electrode and electrolyte. In a RedOx system the electrode, made of an inert materiel (e.g.: platinum) for which there is no exchange of metal ions between metal and electrolyte, acts as a source or sink of electrons. The electrolyte is composed of electron-donors and electron-acceptors, in other words, oxidizing and reducing agents. The RedOx electrode reaction is $Ox + ze^{-} \leftrightarrow Red$. The modified Nernst equation in the low ionic limit is then:

$$E = E_o + \frac{RT}{zF} \ln \frac{[Ox]}{[\mathrm{Re}\, d]} \tag{3.3-1}$$

Where $[Ox]$ is the molarity of the oxidized species and $[Red]$ is the molarity of the reduced species.

A simple example of a RedOx system is shown in Figure 3-3.

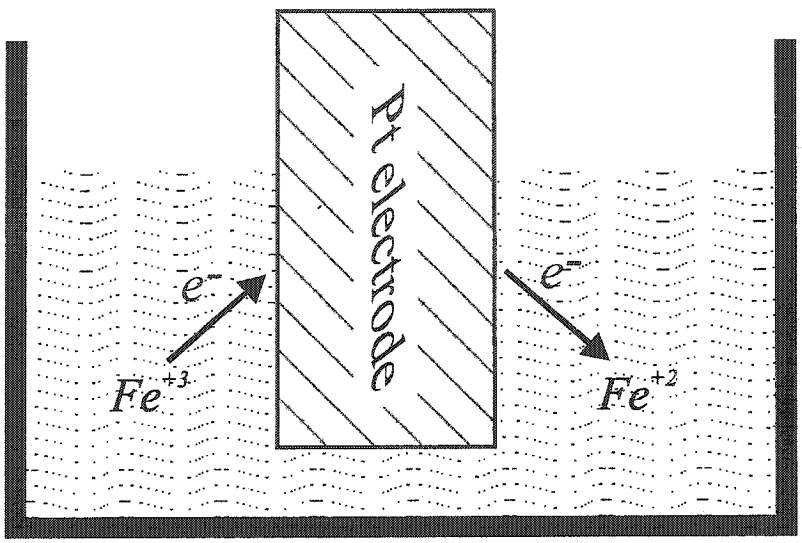

Figure 3-3 Simple schematic of a RedOx reaction on a Pt electrode in a solution of Fe^{+3} and Fe^{+2} ions

In this case the electron donor is Fe^{+2}, the electron acceptor is Fe^{+3}, the electrode is Pt, and the electrode process is:

$$Fe^{+3} + e^{-} \leftrightarrow Fe^{+2} \tag{3.3-2}$$

This electrode reaction consists of changing the oxidation state of ions. In this example Fe^{+3} is the oxidized form and Fe^{+2} is the reduced form.

In general, if the oxidized ions are designated *Ox* and the reduced ions *Red*, then the general RedOx reaction is:

$$Ox + ze^{-} \leftrightarrow Red \tag{3.3-3}$$

Reaction from left to right consumes electrons and is called reduction, reaction from right to left liberates electrons and is called oxidation.

Complex RedOx reactions often involve H^+ ions. An example is given below:

$$MnO_4^- + 5e^- + 8H^+ \leftrightarrow Mn^{+2} + 4H_2O \tag{3.3-4}$$

Equation 3.3-4 applied to the Nernst RedOx equation (3.3-1) yields

$$E = E_o + \frac{RT}{zF} \ln \frac{[MnO_4^-][H^+]^8}{[Mn^{+2}]} \tag{3.3-5}$$

For example, given E_o = 1.545 V, $[MnO_4^-]=10^{-1}$ mol/L and $[Mn^{+2}]=10^{-4}$ mol/L in a solution with a pH of 2 then E = 1.356 V. Similarly, if the pH was 4, E = 1.166 V.

3.4 Reference electrodes

Electrode potentials are normally reported relative to the standard hydrogen electrode (SHE). However, in aqueous solution they are usually measured with respect to a secondary reference electrode (e.g.: calomel, silver/silver-chloride). It is much easier to purchase and maintain a silver/silver-chloride reference electrode than a standard hydrogen reference electrode. Reference electrodes typically consist of a metal, M, covered by a layer of a sparingly soluble salt, MA, immersed in a solution containing saturated A^{-z} anions. Figure 3-4 shows a schematic of a typical reference electrode.

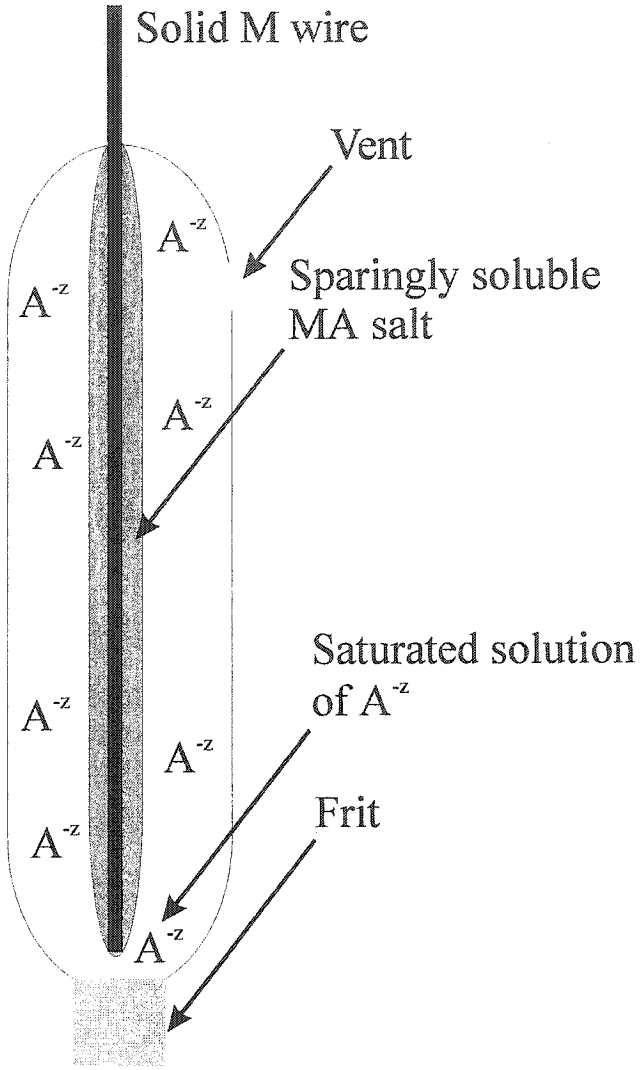

Figure 3-4 Schematic of a typical reference electrode

Consider the most widely used reference electrode, the silver/silver-chloride electrode. As in Figure 3-4 this reference electrode consists of a piece of silver wire (*M*) covered with a film of sparingly soluble salt, AgCl (*MA*). The salt covered wire is immersed in a solution of saturated KCl. At the bottom of the reference electrode there's a ceramic frit to allow the passage of K^+ and Cl^- ions in and out of the electrode. To accommodate any loss or excess of KCl in the chamber a small vent is located near the top of the electrode, which also serves as a filling port when the level of the KCl solution

is low. Crystals of KCl are sometimes added to solution to ensure the solution remains saturated even after extended periods of use.

Consider the following cell: A silver/silver-chloride reference electrode immersed in an aqueous solution of Cu^{+2} ions and a Cu electrode. The oxidation-reduction reactions and associated SHE potentials are as follows:

$$Cu^{+2} + 2e^{-} \rightarrow Cu \quad (0.342\ \text{V}) \tag{3.4-1}$$

$$AgCl + e^{-} \rightarrow Ag + Cl^{-} \quad (0.222\ \text{V}) \tag{3.4-2}$$

The electrodes are connected by a wire and a voltmeter is placed between them in parallel. Refer to Figure 3-5 for a schematic of the cell. Electrons flow from left to right (less positive to more positive).

For the reaction to proceed spontaneously the half-cell reactions must be combined such that the overall voltage is positive. Reaction 3.4-2 must be reversed and the overall reaction is:

$$\tfrac{1}{2}Cu^{+2} + Ag + Cl^{-} \rightarrow Cu + AgCl \quad (0.120\ \text{V}) \tag{3.4-3}$$

As indicated in Figure 3-5 $\frac{1}{2}Cu^{+2}$ will deposit onto the Cu electrode. To balance charge transfer, a Cl^{-} ion is removed from solution surrounding the metal wire and combined with a metallic Ag atom to form AgCl. The solution surrounding the reference electrode now has a net positive charge. In response, a K^{+} ion leaves the saturated solution through the frit into the surrounding medium, hence the solution around the reference electrode is again neutral. Similarly, the solution around the Cu electrode momentarily acquires a net negative charge, the K^{+} ion expelled by the silver/silver-chloride electrode diffuses to the Cu side and charge neutrality is satisfied everywhere.

Now that there is one less K^+ and Cl^- ion in solution it is favorable for the precipitated KCl salts to solvate and replace the lost ions. This way the concentration of K^+ and Cl^- remains constant. It is very important that the Cl^- concentration remain constant. The potential of a reference electrode should not vary, otherwise it would not be a reference electrode. When the Nernst equation is applied to equation 3.4.2 the result is equation 3.4-4.

$$E = 0.222V - \frac{RT}{F}\ln[Cl^-] \tag{3.4-4}$$

The overall voltage depends on the Cl^- concentration, therefore the Cl^- concentration must remain constant.

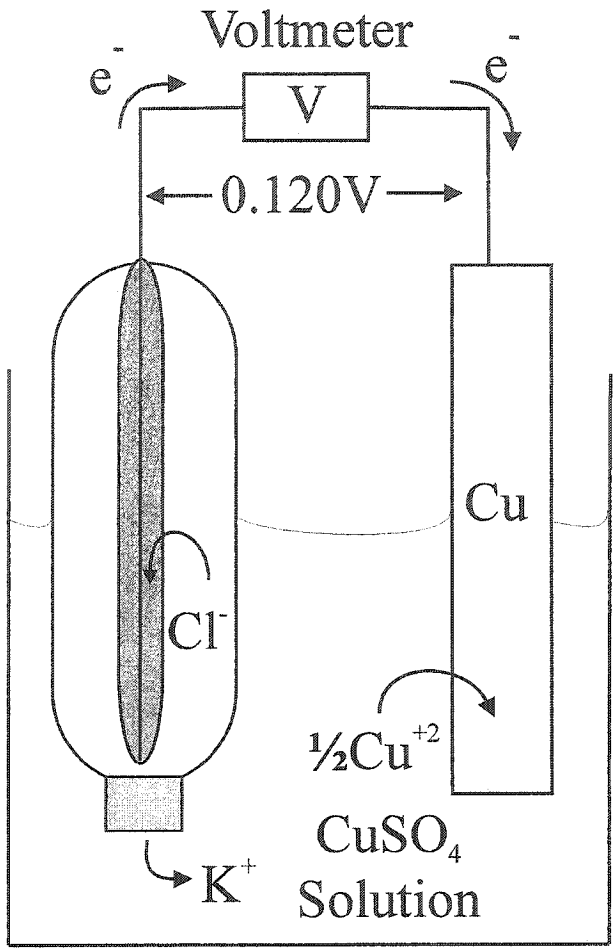

Figure 3-5 Silver/silver-chloride reference electrode attached to a Cu electrode immersed in a Cu sulfate solution

A similar analysis could be performed where the reference electrode is attached to an electrode with a more negative reduction potential, Zn for example. In this case the reactions are simply reversed, the silver/silver-chloride electrode becomes the electron acceptor and Zn the electron donor. AgCl is reduced to Ag + Cl^- and Cl^- ions are released into solution, similarly Zn is oxidized to $½Zn^{+2}$. As $½Zn^{+2}$ ions enter solution charge balance is maintained by Cl^- ions leaving the reference electrode.

3.5 Standard electrode potentials

In general, an electrode with low electrode potential will reduce ions of an electrode with higher potential. A large, positive standard electrode potential indicates a propensity towards reduction, a large negative standard electrode potential indicates a strong tendency towards oxidization. Table 3-1 is a compilation of standard electrode potentials at 25°C in aqueous solution (also refer to Appendix 2).

Table 3-1 Standard electrode potentials in aqueous solution

Metal/Metal-ion couple	Electrode reaction	Electrode potential (V)
Au / Au^{+}	$Au^{+} + e \leftrightarrow Au$	1.692
O_2 / H^{+}	$O_2 + 4H^{+} + 4e \leftrightarrow 2H_2O$	1.229
Pd / Pd^{+2}	$Pd^{+2} + 2e \leftrightarrow Pd$	0.951
Cu / Cu^{+2}	$Cu^{+2} + 2e \leftrightarrow Cu$	0.342
H_2 / H^{+}	$2H^{+} + 2e \leftrightarrow H_2$	0.000
Pb / Pb^{+2}	$Pb^{+2} + 2e \leftrightarrow Pb$	-0.126
Sn / Sn^{+2}	$Sn^{+2} + 2e \leftrightarrow Sn$	-0.137
Ni / Ni^{+2}	$Ni^{+2} + 2e \leftrightarrow Ni$	-0.257
Zn / Zn^{+2}	$Zn^{+2} + 2e \leftrightarrow Zn$	-0.759
H^{+} / O_2	$2H_2O \leftrightarrow 4H^{+} + 4e + O_2$	-1.229
Al / Al^{+3}	$Al^{+3} + 3e \leftrightarrow Al$	-1.662
Li / Li^{+}	$Li^{+} + e \leftrightarrow Li$	-3.040

For example, consider a strip of Zn placed in a solution of $CuSO_4$. Zn/Zn^{+2} has a lower metal/solution electrode potential than Cu/Cu^{+2}, meaning Cu^{+2} ions will be reduced by metallic Zn, which is oxidized. Zn^{+2} ions go into solution and Cu deposits onto the Zn strip.

3.6 Overpotential

When an electrode is made part of an electrochemical cell through which current flows its potential will differ from the equilibrium potential. If E_o is the equilibrium potential without current, and $E(i)$ the potential while current flows, the overpotential, η, is defined as the difference between the two [2.4]:

$$\eta = E(i) - E_o \tag{3.6-1}$$

The overpotential is the voltage required to overcome any hindrance(s) to the overall electrode reaction. There could be many hindrances, including, but not limited to, charge transfer, diffusion, chemical reaction and crystallization. A proper discussion of overpotential and the mechanisms that cause it is well beyond the scope of this project. It is sufficient to say that overpotential exists whenever current flows through an electrochemical cell.

3.7 Mechanisms of electrodeposition

To understand bulk deposition it is useful to consider deposition on the atomic scale. Metal ions in solution are hydrated. It is generally assumed that atoms attach to the crystal via a kink site [2.4]. Figure 3-6 is a step-wise illustration of a hydrated ion depositing into a kink site.

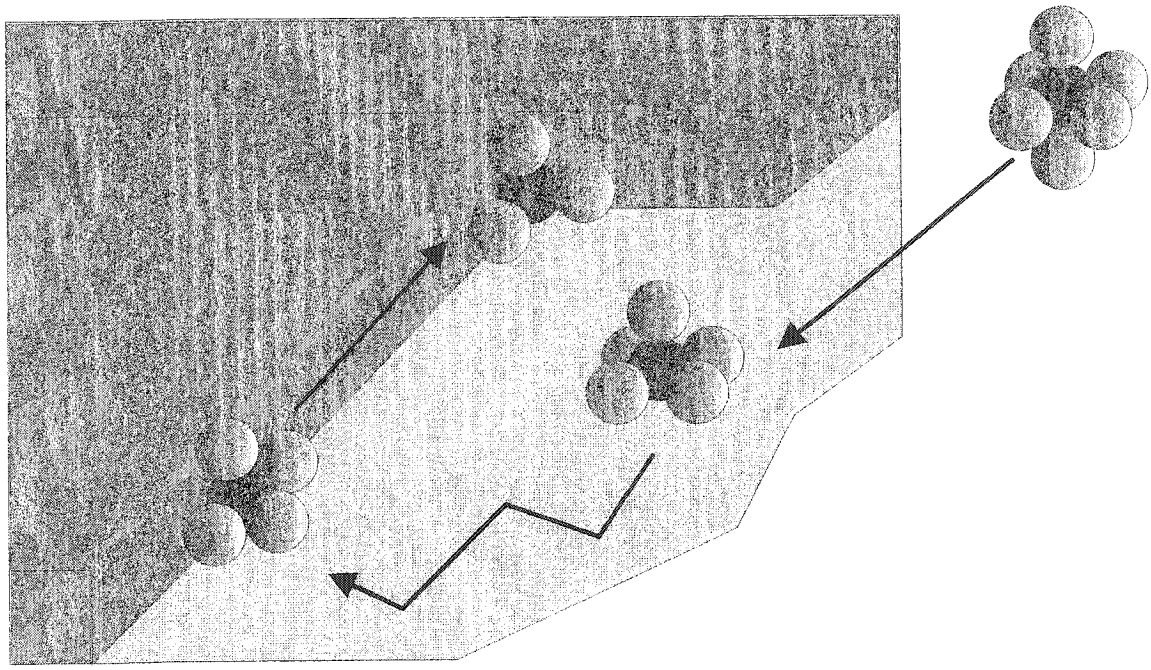

Figure 3-6 Step-wise illustration of a hydrated ion depositing into a kink site

Subsequent electrodeposited atoms break off the remaining water ligands until the original ion is completely stripped and incorporated into the lattice.

Consider a perfectly smooth surface prior to deposition. There are two basic growth mechanisms, layered and 3D crystallites (or nucleation-coalescence). A schematic is given in Figure 3-7.

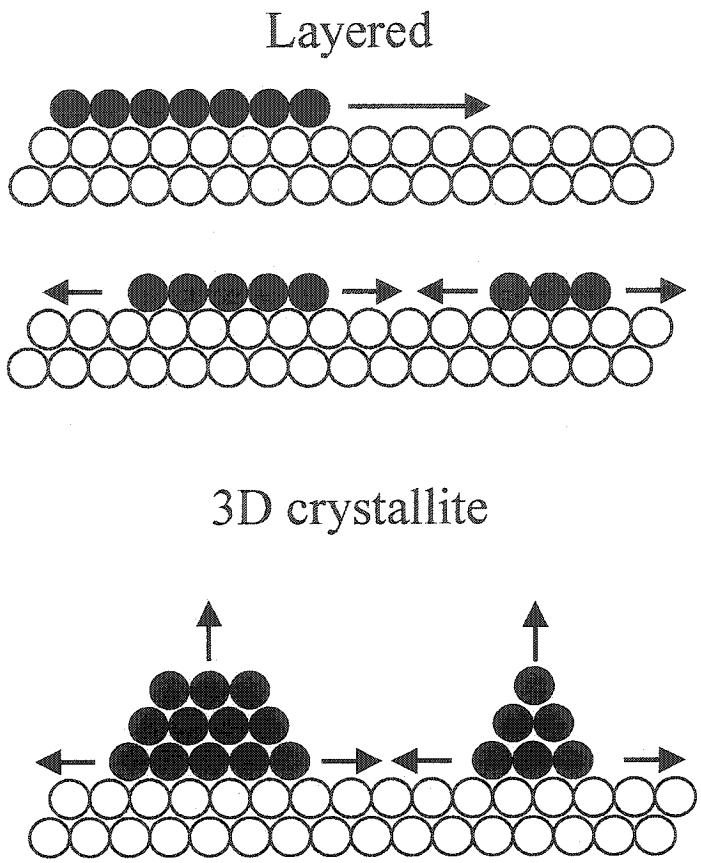

Figure 3-7 Layered and 3D crystallite growth

Understanding growth mechanisms is very important in understanding the properties of a deposit. The ideal growth mechanism is sequential layering, one atomic layer at a time, which can only be achieved under highly controlled conditions. Most deposits grow by a combination of the two mechanisms. If a deposit is inclined to grow exclusively via nucleation-coalescence, large tree-like clusters result. Sn is a good example of growth by nucleation-coalescence. Once deposited, a Sn atom is highly mobile. This mobility encourages cluster growth. Figure 3-8 is an example of such a Sn deposit. The circled structure in the right image is especially interesting. The structure looks amazingly similar to a fern seedling. Despite the interesting structures, in general, cluster growth should be avoided.

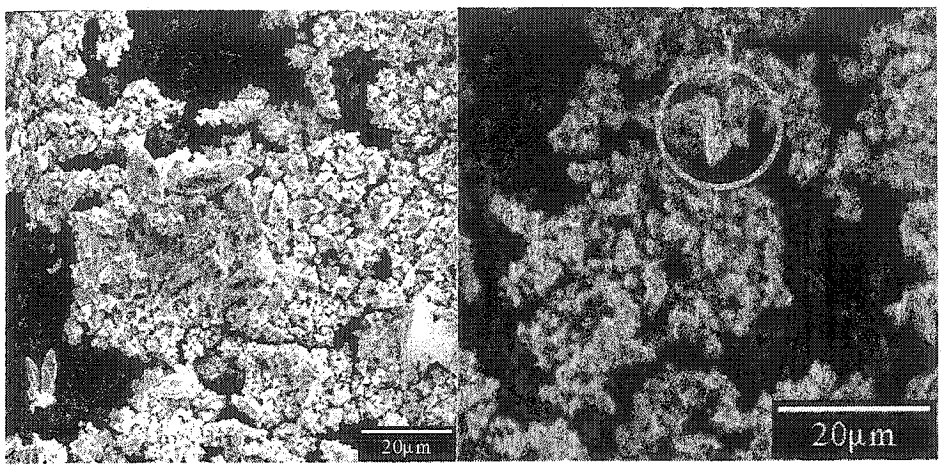

Figure 3-8 Sn deposit from a simple Sn-sulfate bath with no levelers

3.8 Leveling agents

The importance of leveling agents is not matched by an understanding of how they work. The effects of leveling agents on the electrodeposition process are only recently becoming understood. There are four classes of leveling agents, described in Table 3-2 [3.2].

Table 3-2 Description of leveling agents

Class	Subclass	Description
Suppressor	Carrier	Increases overpotential so a higher voltage is required to deposit. Forms a surface film analogous to carpet shag, inhibiting mass transfer and ion mobility. (e.g.: long polymers)
	Leveler	Reduce surface topology by adsorbing at a mass transfer dependent rate, then poisoning that site. Not a static film like carrier class (e.g.: surfactants). Refer to Figure 3-9.
Accelerator	Brightener	Electrochemically active species. Rapidly diffusing small molecule which catalyses charge transfer.
	Depolarizor	Depolarize water ligands around the ion weakening the shell.

Typically, a combination of all the above is used in a plating bath. Figure 3-9 illustrates how a leveler works. By adsorbing at a mass transfer dependent rate it blocks a site of high growth, encouraging growth in other areas.

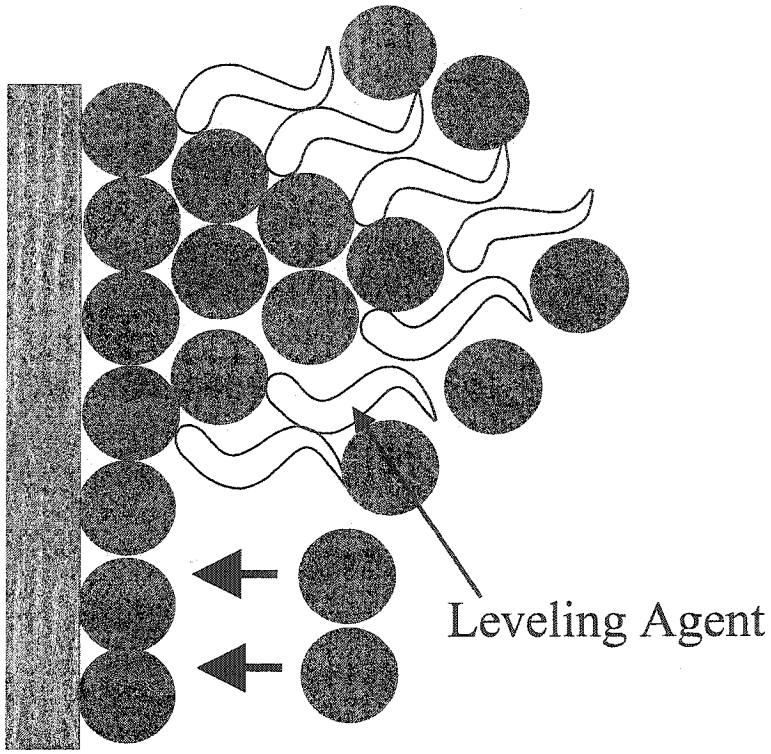

Figure 3-9 Artist's rendition of how leveling agents work

3.9 Pulse plating

Nanocomposites of interest for Li-ion batteries can be fabricated by depositing alternating layers of active and inactive material. Deposition parameters determine the periodicity of the inactive/active sandwich layer. Such a material is sometimes referred to as compositionally modulated. Brenner first performed electrodeposition of a compositionally modulated film in 1939 by employing two separate baths. One compositionally modulated layer would require two immersions in two separate baths with thorough rinsing in between. This is too cumbersome to be adopted. Deposition from a single bath with two salt components is needed.

Two species in a common bath presents an obvious problem, how can alternating layers of each species be deposited without depositing a homogeneous alloy? The

electroplating cell would have to be made up of a substrate (cathode), insoluble anode, electrolyte (probably water) and two metal-salt components. Each species has a unique deposition potential. Consider Sn^{+2} and Cu^{+2} ions in solution. At 0.342 V (vs. SHE) only Cu will be able to deposit. At -0.137 V (vs. SHE), however, both species will deposit. This is unacceptable, unless a plating bath with dramatically different metal-ion molaritites is used. Cu^{+2}, which deposits more readily, will be present in low concentration, similarly, the concentration of Sn^{+2} will be high. At 0.342 V (vs. SHE) only Cu will deposit. Cu^{+2} ions near the cathode will be quickly consumed and the rate of deposition will be limited by how quickly new Cu^{+2} ions can be brought to the cathode. The flux of Cu^{+2} ions will be low, and deposition will be slow. At -0.137 V (vs. SHE), both species will deposit. Due to the dramatic difference in ionic concentrations mostly Sn will deposit with trace amounts of Cu. Trace amounts of Cu in the Sn layer is acceptable for our applications (nanocomposite negative electrode materials). Figure 3-10 shows a typical pulse plating waveform.

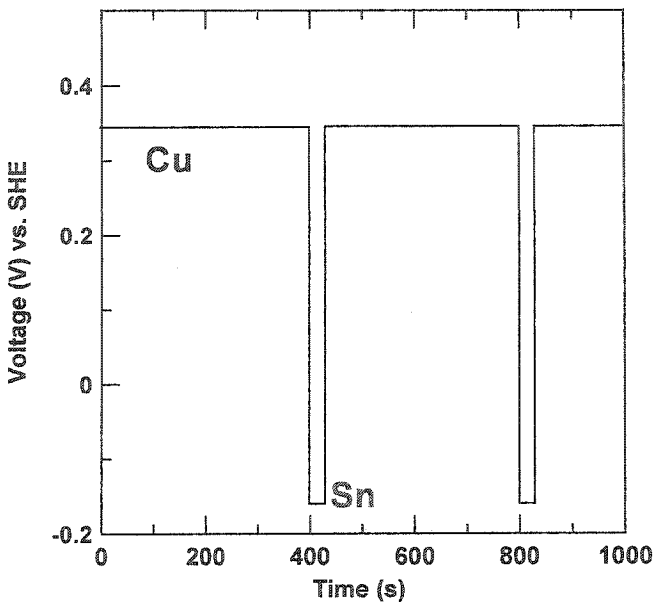

Figure 3-10 Pulse plating waveform

The length of each pulse determines the thickness of each layer. To fabricate a nanocomposite, layer thickness would have to be on the order of tens of angstroms. Ideally, alternating layers of each species will deposit without interdiffusion. Figure 3-11 is an ideal representation of the pulse plating process. Single bath pulsed electrodeposition of compositionally modulated alloys has been highly successful in systems such as Cu-Ni [3.3-4] and Cr-Ni [3.5]. We hoped the technique would be equally successful in active-inactive systems such as Cu-Sn. As discussed in chapter four, this is not the case.

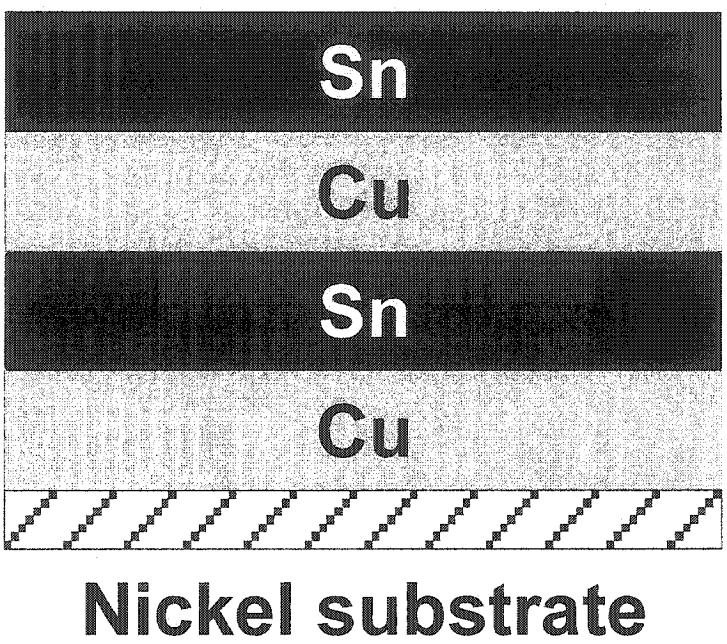

Figure 3-11 Ideal pulse plated film, alternating layers of Sn and Cu with no interdiffusion

A pulsed waveform with a zero current off pulse could also be used to fabricate compositionally-modulated nanocomposites. During the off pulse the ionic species with a more positive SHE potential (i.e.: Cu^{+2} @ 0.342 V) will ion-exchange with deposited atoms of the species with a more negative SHE potential (i.e.: *Sn* @ -0.137 V). The on-off current pulse is applied hundreds/thousands of times building up alternating layers of Sn and Cu layers. Figure 3-12 shows a typical pulse plating waveform with a zero current pulse. This technique is used extensively in the thesis and will be discussed in section 4.4.

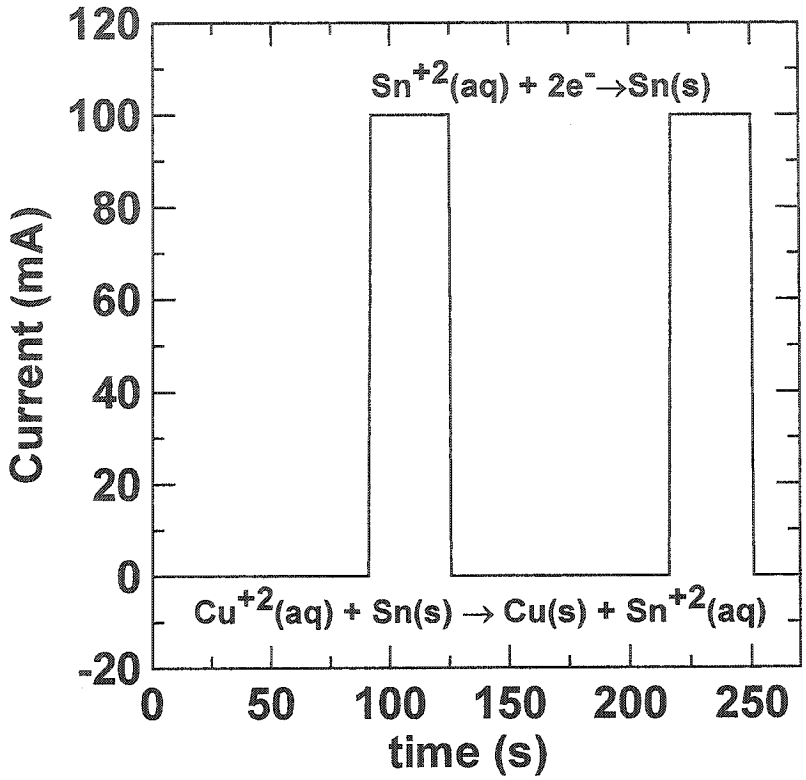

Figure 3-12 Zero current pulse plating waveform

3.10 Immersion plating

Immersion plating is also known as dip or displacement plating. It is used extensively in industry due to its technical simplicity and low cost. To immersion plate metal x onto metal y, metal x must have a higher reduction potential than metal y. For example, when Sn metal (y) is placed in a solution of Cu (x) sulfate Cu ions will exchange with Sn atoms via the reaction:

$$Sn + Cu^{+2} \rightarrow Sn^{+2} + Cu \qquad (3.10\text{-}1)$$

Equation 3.10-1 is constructed from two half reactions, presented in Table 3-3. This reaction is mentioned throughout the thesis, especially in section 4.4.1.

Table 3-3 Standard hydrogen electrode (SHE) potentials and change in free energy for the electrodeposition of Cu and Sn

Reaction	SHE Potential (V)	ΔG (eV) / atom
$Sn^{+2} + 2e \Rightarrow Sn$ (y)	-0.137	0.274
$Cu^{+2} + 2e \Rightarrow Cu$ (x)	0.342	-0.680
$Sn + Cu^{+2} \Rightarrow Sn^{+2} + Cu$	0.479	-0.954

Typically only very thin layers of metal x are deposited, since the base metal (y) is quickly covered with deposit x. However, if species x readily interdiffuses into y then y can be completely converted to x, in time. Such is the case with the Sn/Cu system.

A good example of immersion plating is gold (Au) on Cu. An inexpensive Cu necklace is quickly and easily covered (gilded) with 24 carat gold $(Au^{+3} + 3e^{-} \rightarrow Au@1.36V)$ creating the illusion of a pure gold necklace at a fraction of the cost (don't tell the girlfriend) [3.6].

4 Results and discussion

Until now the thesis has been focused on theory and experimental setup, now we get to the main course, results.

4.1 Behavior of electroplated Sn in a Li-cell

Sn negative electrodes have been studied by such authors as Besenhard [4.1-3], Huggins [4.4-5], Owen [4.6], Schliech [4.7-11] and Fujitani [4.12]. It is well known that when Sn or Sn-based electrodes are used in a Li cell the Sn particles undergo severe pulverization. Pulverization results in loss of electrical conductivity, which eventually results in poor cycle performance [4.13].

As discussed in section 1.5, the pulverization (i.e. cracking) problem may be avoided by fabricating a Sn nanocomposite. The nanocomposite could consist of alternating layers of active and inactive material with respect to alloying with Li. We chose to try to electrodeposit a Cu-Sn nanocomposite. The nanocomposite would be fabricated by depositing alternating layers of Cu and Sn. Sn was chosen as the active component due to its large capacity for alloying with Li. Cu was chosen as the inactive component because it is easily electrodeposited from aqueous solution.

Before an electroplated, layered nanocomposite could be attempted it was important to understand the electrodeposition process for each layer. Cu can be deposited without difficulty. Using a simple Cu-plating bath, smooth films of uniform nanometer thickness were deposited. Sn, however, presented numerous problems (briefly discussed in section 3.7). Electroplated Sn has a tendency to cluster (Figure 3-8), resulting in a rough film with uneven surface growth and film thickness. Many Sn plating bath recipes

were tested (Table 2-1), but only one, a proprietary Sn plating bath from Lucent Technologies (SnTech) could satisfy all of our requirements. Using the SnTech bath, smooth, uniform thickness films only several nanometers thick could be deposited. To electrodeposit a Cu-Sn nanocomposite consisting of alternating layers of Cu and Sn the two baths had to be combined. Ideally, the dual bath would be able to deposit smooth, thin layers of both Cu and Sn. Before a dual bath was attempted, electroplated Sn was tested in a Li cell to ensure that it behaved as expected. Unfortunately, it did not. Before the unexpected behavior is discussed, the expected behavior will be discussed.

4.1.1 Typical behavior of electroplated Sn in a Li-cell

Electroplated Sn negative electrodes were expected to behave much like electrodes made from sputtered or powdered Sn. The voltage profile of a Li-Sn cell is well understood [1.21-1.23], and presented in Figure 4-1. SEI formation and effects due to irreversible capacity complicate the structure of the first discharge voltage profile. Correspondingly, the first recharge cycle and second discharge cycles are presented in Figure 4-1.

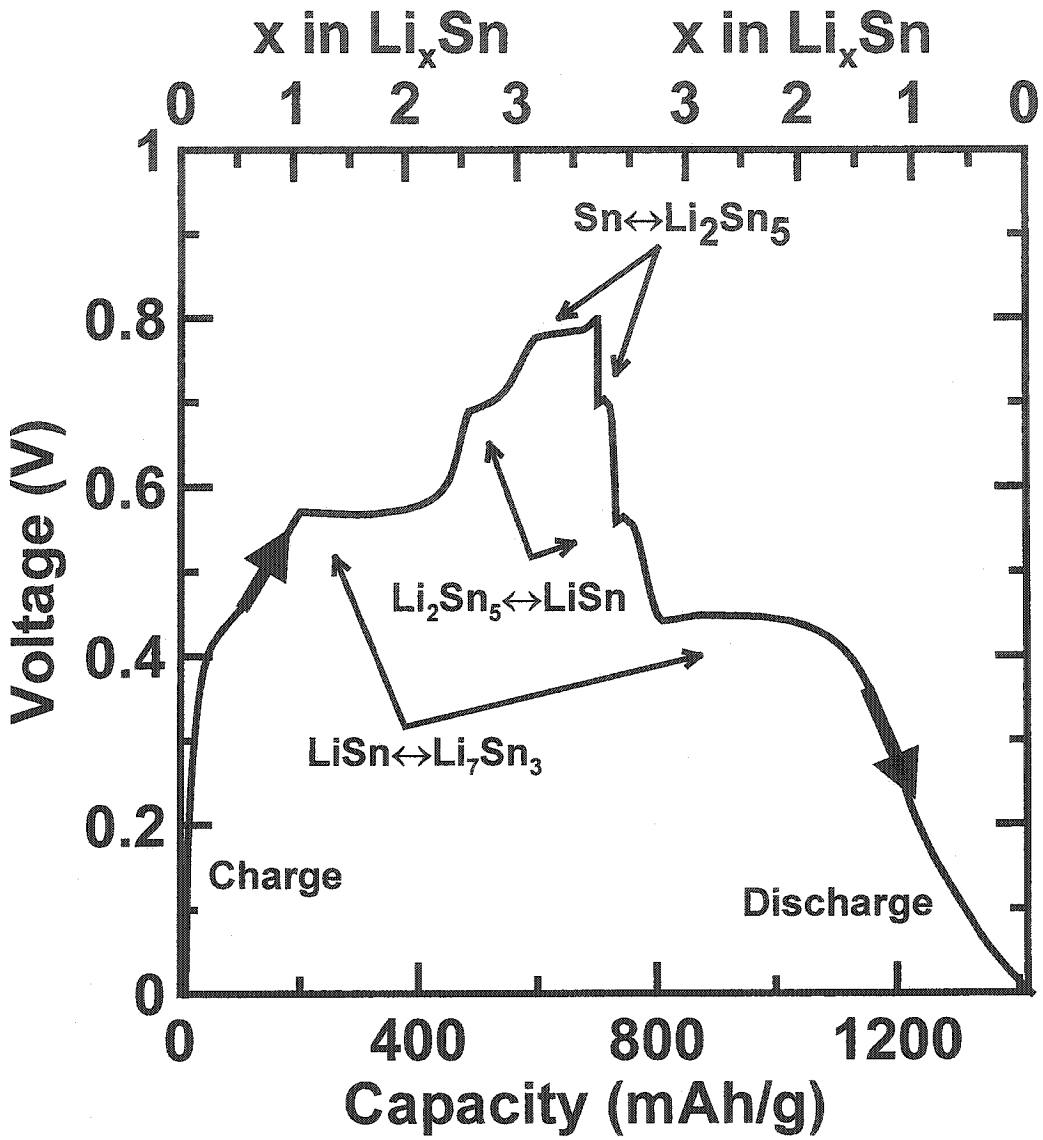

Figure 4-1 A typical Li-Sn voltage profile where plateaus are well understood and correspond to a change in phase according to the Li-Sn phase diagram. Voltage is measured vs. metallic Li. The cell was cycled at 100 μA/cm^2 or 50 mA/g of Sn

The voltage profile in Figure 4-1 was obtained from a Li-Sn cell with a Sn powder positive electrode. Each plateau in the voltage profile corresponds to a two-phase co-existence region according to the Li-Sn phase diagram, given in Figure 4-2 [1.10].

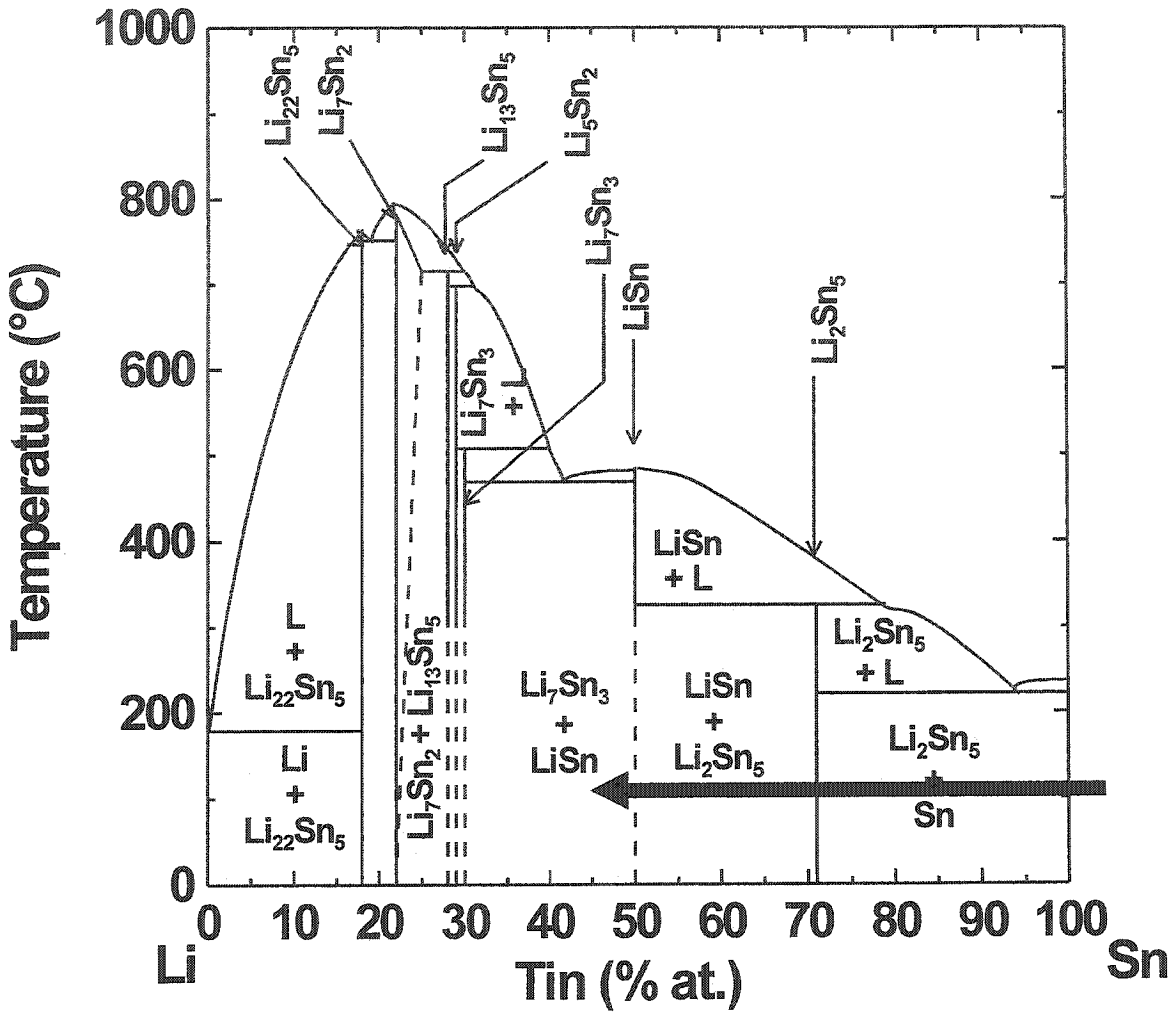

Figure 4-2 The Li-Sn phase diagram. As a Sn-based electrode is lithiated, starting from the right hand side of the figure, it goes though many phase changes. This is reflected in the voltage profile of Figure 4-1 [1.10]

The behavior is well understood [1.21]. Previous studies with Sn [1.5, 1.21-23] have shown that no capacity is expected above 0.8 V.

4.1.2 Observed behavior of electroplated Sn in a Li-cell

A section dedicated to the observed behavior of electroplated Sn electrodes in a Li-cell is required because the observed behavior is different from the typical behavior

presented above. When Li-Sn cells were cycled between 1.6 V and 0 V sustained capacity at voltages well above those expected from section 4.1.1 was observed. From Figure 4-1 significant capacity is not expected above 0.8 V.

Figure 4-3 shows three voltage vs. capacity data sets representing three different Li-Sn cells prepared with electroplated Sn electrodes. Keep in mind that the cells were cycled between 0 and 1.6 V. In panel a), the voltage vs. capacity profile is very different compared to the typical voltage profile given in Figure 4-1. Unexpected capacity is observed at high voltage, which appears to be irreversible. In the remainder of the thesis, sustained, high-voltage (above 0.9 V) capacity will be referred to as anomalous high-voltage irreversible capacity (AHVIC). In Figure 4-3a) AHVIC is only observed during the first cycle. In panel b) AHVIC is observed during the second cycle, but not during the first. In panel c) AHVIC is observed during the third cycle, but not during the first or second.

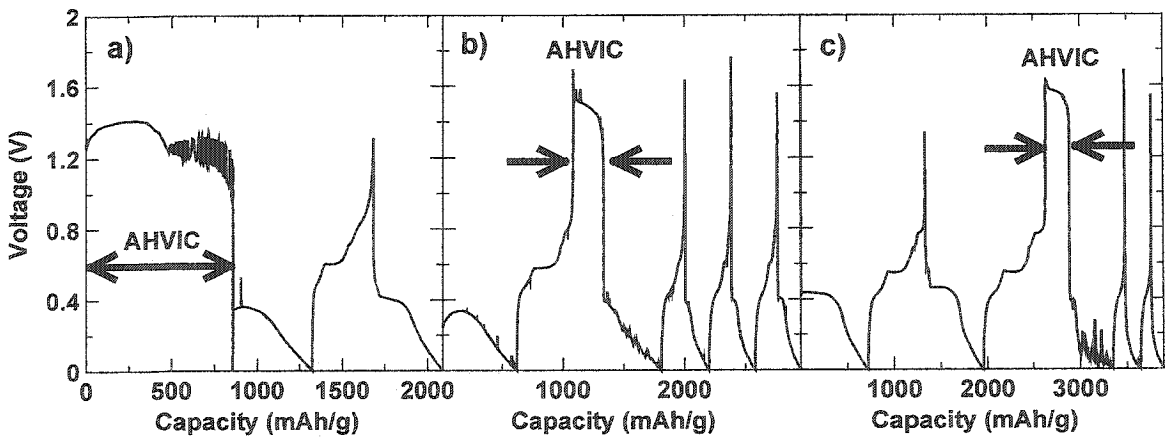

Figure 4-3 Three voltage vs. capacity data sets representing three different cells using electroplated Sn negative electrodes. Cells were cycled between 0 and 1.6 V

Why does the voltage vs. capacity profile from cells made with electroplated Sn differ from the voltage vs. capacity profile in Figure 4-1, and why does the anomalous high-voltage irreversible capacity sometimes not occur until the second or third discharge? Numerous experiments were performed to determine the cause of the anomalous behavior. Table 4-1 outlines the suspected causes of the irreversible capacity and the analysis techniques used.

Table 4-1 List of candidates tested as the cause of anomalous behavior when electrodeposited Sn is used in a Li cell

Candidate		**Analysis**
Cell Component	Solvent	Test using different solvents (e.g.: EC:DEC, PC, EC)
	Li-salt	Test using different Li-salts (e.g.: $LiClO_4$, $LiPF_6$, $LiBF_4$)
Cycling Parameter	Discharge Current Density	Cycle at different discharge current densities
	Recharge Cut-Off Voltage	Cycle at different recharge cut-off voltages
Electrodeposition Parameter	Bath Type	Electroplate from different Sn baths (all Sn baths mentioned in Table 2-1).
	Deposition Current Density	Test different deposition current densities.
	Concentration of Leveling Agents	Vary the concentration of leveling agents in plating bath.
Other	H_2O trapped in film	Thermal Gravimetric Analysis (TGA)
	Large O_2 content	Mössbauer spectroscopy

Due to the large amount of data generated during this search only pertinent results will be discussed. A partial discussion of the experiments is given in [4.14]. It was found that the recharge cut-off voltage and discharge current density both played an important role in the existence of AHVIC. The effect of recharge voltage will be discussed first. Figure 4-4 shows the voltage vs. capacity for a Li/electroplated-Sn cell

where the recharge cut-off voltage was kept below 1.4 V (unlike the cells in Figure 4-3, which were cycled to 1.6 V) and cycled a dozen times. No anomalous high-voltage irreversible capacity was observed. Note that in Figure 4-1 the recharge voltage was also kept below 1.4 V. With further testing it was found that anomalous high-voltage irreversible capacity could be avoided if the recharge cut-off voltage was below 1.4 V.

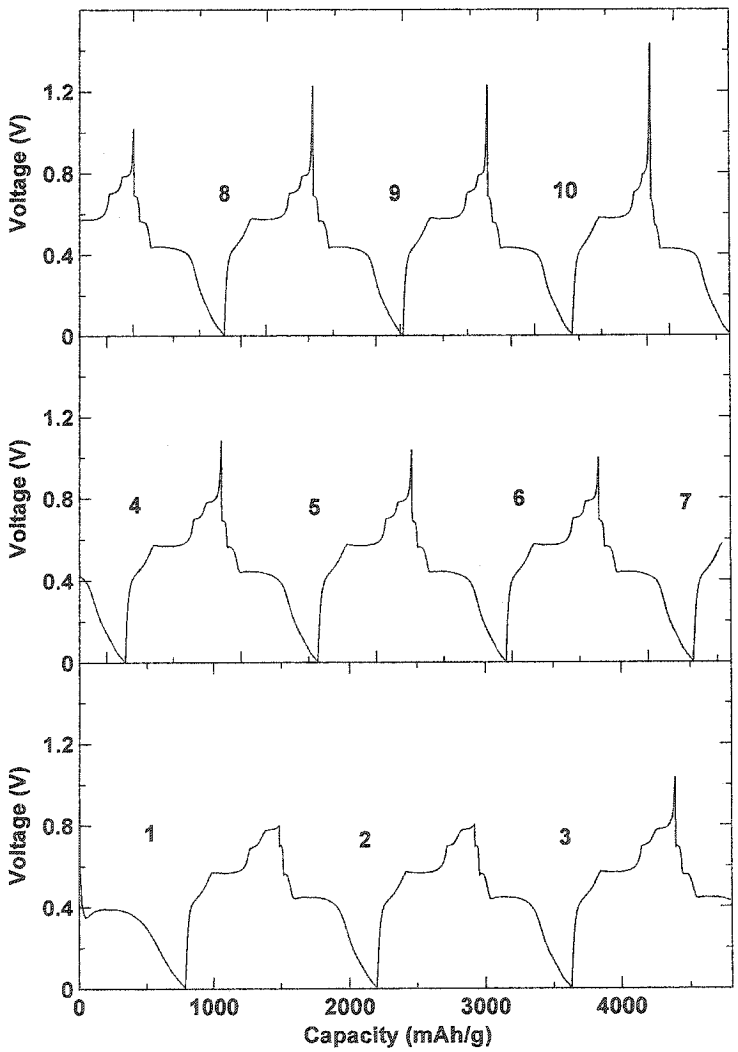

Figure 4-4 Voltage vs. capacity for a Li/electroplated Sn cell where the recharge cut-off voltage was kept below 1.4 V

The effect of discharge current density will be discussed next. Figure 4-5 shows irreversible capacity vs. specific current for Li-Sn cells with electrodes prepared from a SnTech solution (Table 2-1). Above 0.8 V, Li is not reacting with Sn. Capacity above 0.8 V is probably due to decomposition of electrolyte. Unlike the reaction of Li with Sn, the reaction of Li with electrolyte is irreversible. Panel a) is a plot of irreversible capacity observed during the first discharge vs. specific current. Panel b) is a plot of the sum of irreversible capacity for all cycles (usually the first two or three) vs. specific current.

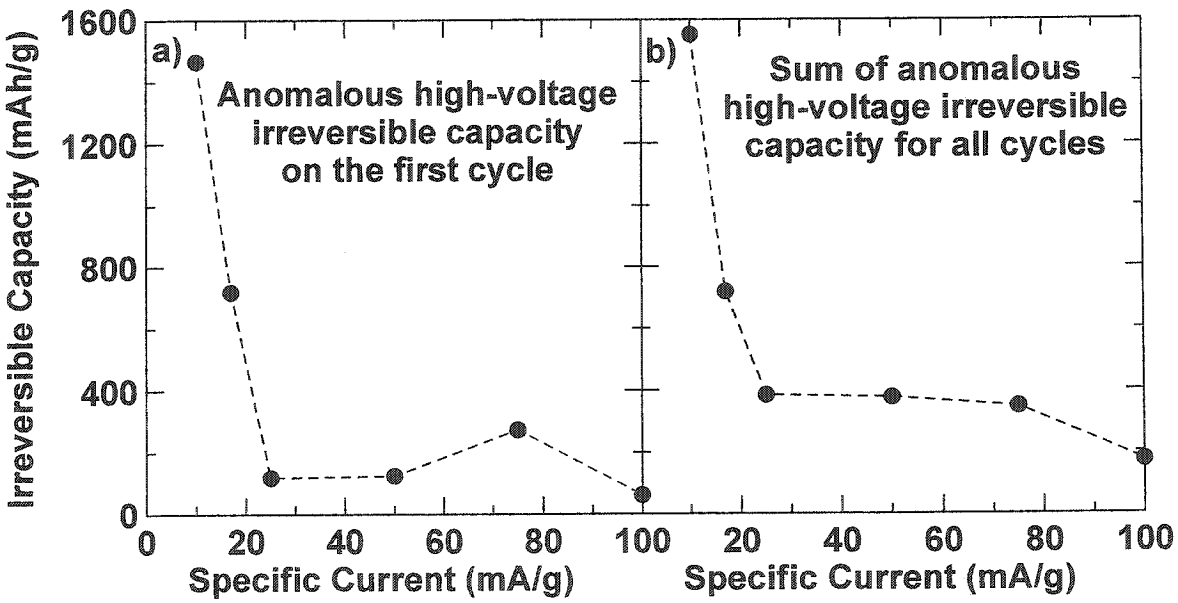

Figure 4-5 Anomalous high-voltage irreversible capacity vs. specific current for Li-Sn cells with electrodes prepared from a SnTech solution

There is an obvious relationship between the specific discharge current and the presence of anomalous high-voltage irreversible capacity. An increase in specific current results in a decrease in anomalous high-voltage irreversible capacity. We try to understand this behavior using the following speculative model. Sn has a unique morphology on the

atomic scale that acts as a catalyst for the decomposition of electrolyte. The electrolyte decomposes until a thick layer is built up, thus blocking the catalytic surface and preventing subsequent decomposition. The layer of decomposed electrolyte also serves to inhibit the diffusion of Li, decreasing the overall capacity. Sometimes the irreversible capacity is observed during the first discharge, we believe in cases where a very clean Sn surface exists. If the Sn surface is "dirty" then it can be "cleaned" during a charge-discharge cycle. For example, during such a complete cycle, thin layers of Sn oxides will be converted to Sn and Li_2O. If the cell voltage is raised high enough, all the lithium is removed from the Sn and the clean catalytic surface is exposed. If the cell voltage is kept below 0.8 V, (as in the first few cycles of Figure 4-4) then Li-Sn alloys are still present and the catalytic surface is not.

The catalytic decomposition must occur at some finite rate. During decomposition a layer of decomposed products builds up on the surface of the catalytic Sn inhibiting diffusion of lithium. Consider two cells, one cycled at a high rate, and the other cycled at low rate. The cell cycled at a high rate should have less anomalous high-voltage irreversible capacity than the cell cycled at a slow rate. Given that the catalytic conversion proceeds at a finite rate, when lithium is supplied to the surface at a rate greater than the rate of catalytic conversion, some of the Li will alloy with the Sn, changing the surface chemistry. The Li-Sn alloy surface does not have the same catalytic properties as "clean" Sn, so decomposition stops. Similarly, when the cell is charged above 1.5 V all of the Li has been removed forming a “clean”, catalytic Sn surface.

To test this hypothesis electroplated Sn cells were cycled at varying charge-discharge rates. Figure 4-5 shows the effect of cycling current density on anomalous high-voltage irreversible capacity.

It should be noted that this behavior has never been reported by the authors mentioned at the beginning of this chapter [4.1-12]. We were the first to report the behavior and offer an explanation for its existence. Sn-based electrodes are frequently used in the development of advanced negative electrode materials for Li-ion batteries, therefore it is of paramount importance to understand everything about the behavior of Sn in a Li-cell.

4.1.3 Anomalous high-voltage irreversible capacity observed in Li-cells made from sputtered and powder Sn electrodes

After the discovery of anomalous high-voltage irreversible capacity in electroplated Sn electrodes we wondered why this behavior had not been observed in other Sn-based electrodes, such as sputtered Sn films, or composite electrodes made from Sn powder. A large recharge voltage, greater than 1.4 V, is required to induce the catalytic decomposition of electrolyte. Previous studies used a lower recharge voltage than 1.4 V, typically 0.9 or 1.1 V. A series of cells using Sn electrodes prepared by both sputter and composite methods were prepared and cycled above 1.4 V. The results from these cells will be discussed next.

Figure 4-6 shows voltage versus capacity for a Li-cell made from a Sn powder composite electrode. A small amount of anomalous high-voltage irreversible capacity is observed near 1.4 V (remember this behavior is not expected as discussed in Figure 4-1).

Note that the irreversible capacity associated with the formation of SEI on the Sn powder composite electrode is insufficient to account for ~100 mAh/g of specific capacity observed in Figure 4-6. A SEI was formed on the electrode in Figure 4-1, yet no capacity is observed at 1.4 V.

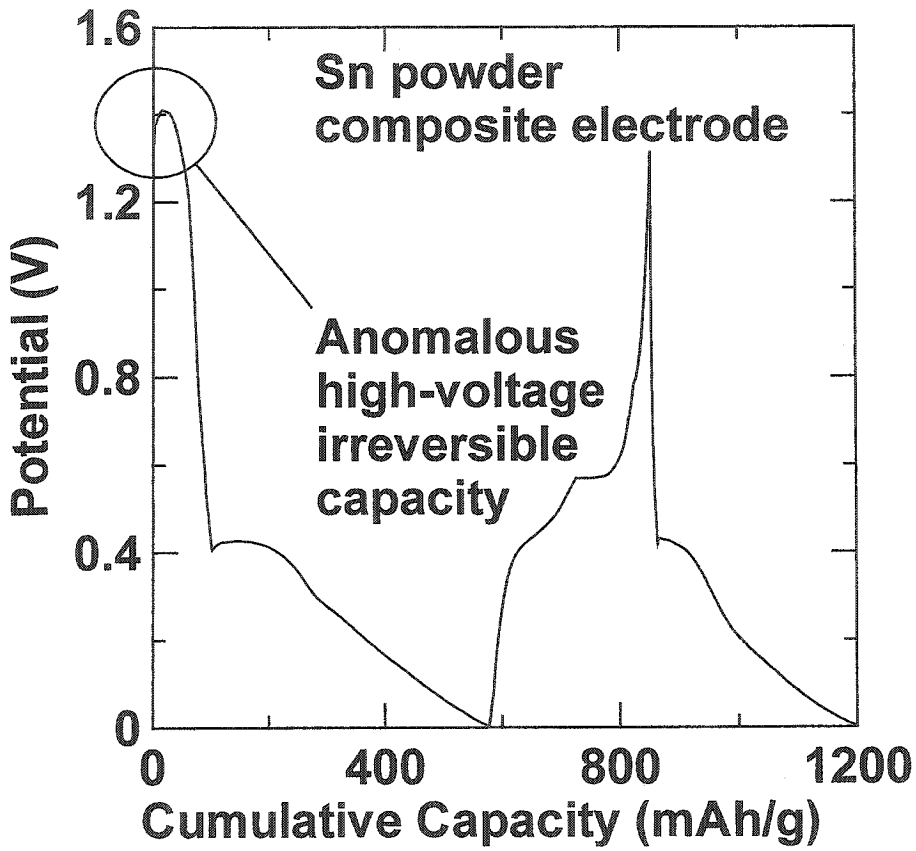

Figure 4-6 Anomalous high-voltage irreversible capacity in a Li-Sn powder composite electrode cell

Sputtered Sn was tested next. Two electrodes were cut from the same sputtered film and charged to different voltages, one above 1.4 V (to 1.6 V) and one below (to 0.8 V). The results in Figure 4-7 clearly identify the effect of recharge voltage on the existence of anomalous high-voltage irreversible capacity. Figure 4-7 shows that anomalous high-

voltage irreversible capacity is present in the sputtered Sn electrode cycled above 1.4 V, but not in the electrode cycled to 0.8 V.

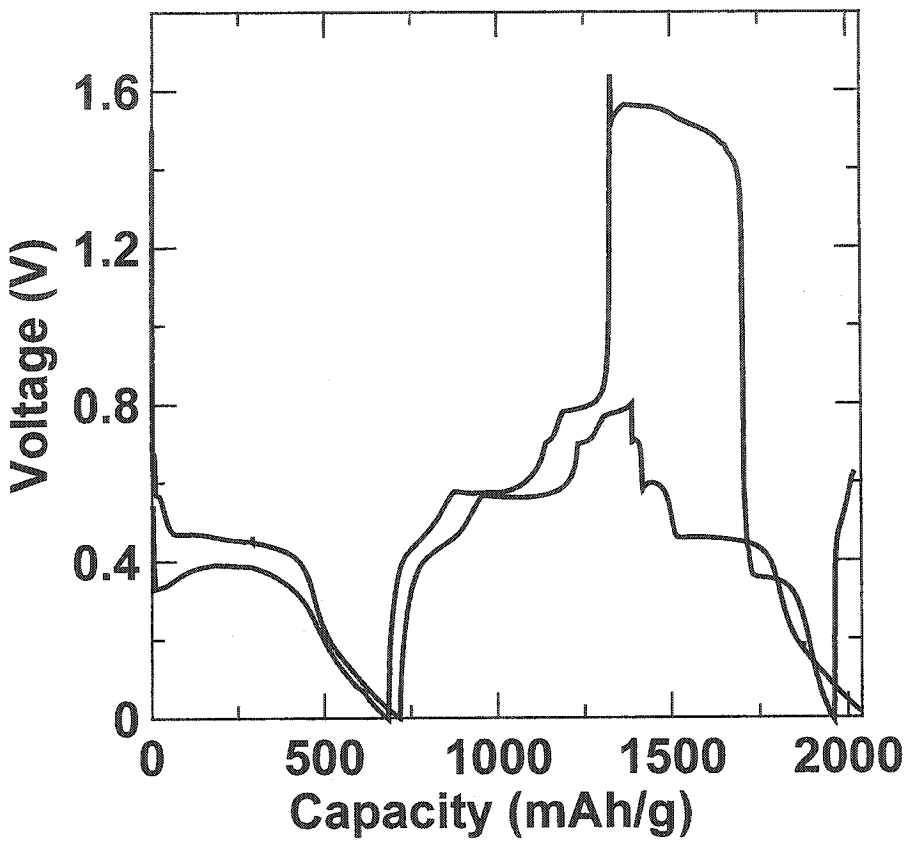

Figure 4-7 Anomalous high-voltage irreversible capacity observed in sputtered Sn electrodes cycled above 1.4 V, but not in sputtered electrodes cycled to 0.8 V

The study of electrodeposited Sn as a negative electrode in Li-cells was expected to take a few weeks, instead, it ballooned into a year-long project. Although the study was time intensive, the results are very important to anyone working with Sn-based negative electrode materials. Now that the cause of anomalous high-voltage irreversible capacity was better understood, it was time to proceed to the next phase of the project, electroplated nanocomposites.

4.2 The bronze-age

Alloys have been proposed and studied as negative electrodes in lithium batteries for many years [4.1-5]. Studies of Li-alloys suggest that the best cycling life can be obtained when two-phase co-existence regions between alloys of different composition can be eliminated [4.15-16]. These two-phase regions appear as plateaus in the voltage-capacity relations of Li/alloy electrochemical cells. It was shown that electrode materials made of Sn grains on the order of nanometer dimensions did not display these two phase regions and offered good cycle life [4.15-16]. The materials in [4.16] were made by high-impact mechanical alloying and the materials in [4.15] were made by sequential sputter deposition. Neither of these production methods is likely suitable for large-scale, low-cost production of nanostructured electrode materials.

Electrodeposition has been used to prepare many types of nanostructured materials [4.17-24]. In [4.24] nano-structured Cu-rich Cu-Sn alloys were successfully deposited from a simple aqueous bath. It was our goal to prepare nanostructured materials incorporating Sn by pulsed electrodeposition from a single, multi-component plating bath along the lines described in [4.24]. As a first step we learned to electrodeposit smooth, shiny, Sn films only several nanometers thick, using Lucent's SnTech line of electroplating baths. The ability to deposit nanometer-thick films is essential for the fabrication of nano-composites, so Lucent's SnTech line was used exclusively. When used as working electrodes in Li/Sn cells, electroplated Sn showed anomalous irreversible capacity during early cycles. The anomalous behavior is discussed in the previous section.

All deposits were performed galvanostatically. By controlling the pulse length and current density it is possible to accurately control the Cu:Sn stoichiometry. Consider a solution of Sn^{+2} and Cu^{+2} ions with a relative concentration of 100:1. $Cu^{+2}(aq) + 2e^{-} \leftrightarrow Cu(s)$ has a more positive standard reduction potential (+0.342 V SHE) than $Sn^{+2}(aq) + 2e^{-} \leftrightarrow Sn(s)$ (–0.137 V SHE). Therefore, Cu will deposit at a more positive potential than Sn. The lower the current density, the more positive the potential is at the cathode. At sufficiently small current densities the potential at the cathode is sufficiently large so that Cu, but not Sn, will deposit. This enables a pure layer of Cu to be deposited. At larger current densities (large negative potentials) Sn will readily deposit, and so will Cu. Given a 100:1 difference in molarity, the Cu deposition is limited by diffusion, while the Sn deposition is less limited. At large current densities, the difference in concentrations encourages a deposit of mostly Sn with trace amounts of Cu. By alternating between high and low current density pulses, in theory, layers of pure Cu and mostly Sn are sequentially deposited.

At low current densities the deposit grows slowly, so, to obtain a film of alternating Cu/Sn layers of equal thickness, the low current density pulse would have to be much longer than the high current density pulse. The length of each pulse was calculated assuming 100% current efficiency. It was also assumed that pure Cu is deposited during the low current density pulse and pure Sn during the high current density pulse. These assumptions are most certainly wrong, as discussed in section 2.2.4. However, it will not be a major concern. The Cu:Sn ratio in the deposit can be measured later using an electron microprobe. The pulse lengths (t_{Pulse}) are then determined by the

molar mass (M_M), density (ρ), desired thickness (T), number of electrons needed to reduce the metal ion (n), Faraday's constant (F) and current density (j) as follows:

$$t_{pulse} = \frac{nTF\rho}{M_M j}$$

These pulse times are used in the Visual Basic program to trigger the Keithley to switch between current densities.

Potentiostatic deposition was not used because the overpotential at the cathode changes during deposition, as the potential varies so does the current density. It is therefore difficult to obtain alternating layers of equal thickness when the current density is constantly changing.

The original goal of this research was to produce nano-composites via pulsed electrodeposition in a single bath. Figure 4-8 shows the x-ray diffraction pattern of a deposit obtained by pulsed deposition in a single bath where the molarity of Cu is 100× less than the molarity of Sn.

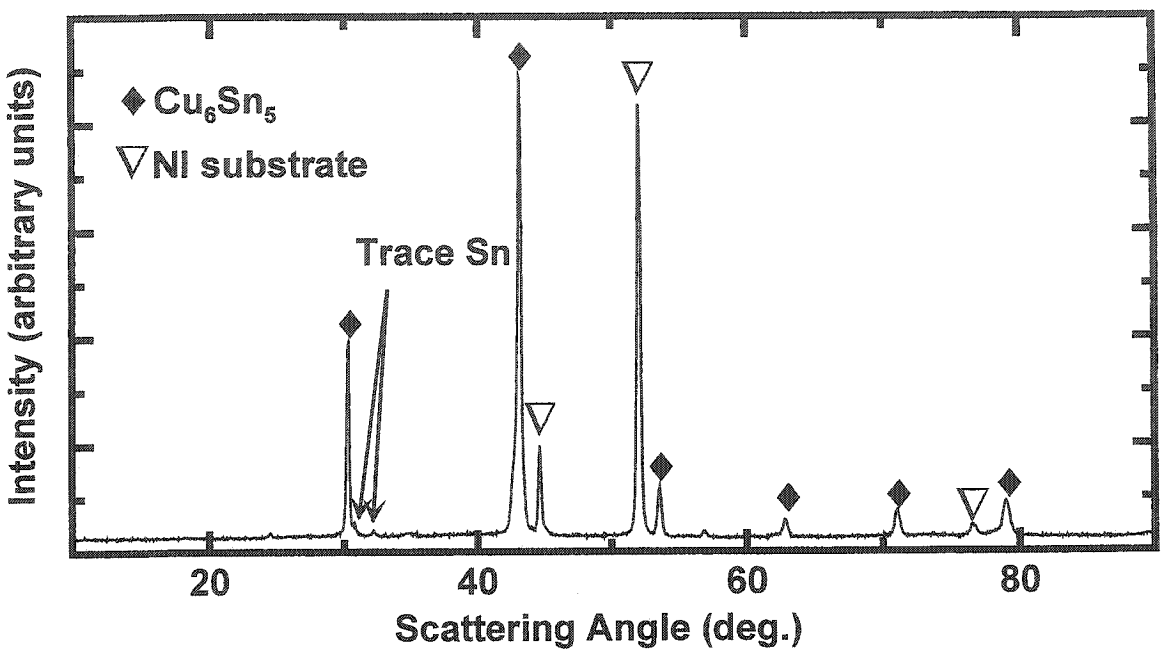

Figure 4-8 X-ray diffraction pattern of a Cu_6Sn_5 film electroplated by pulsed deposition onto a nickel substrate. Pulse current densities were 0.08 mA/cm^2 and 4.00 mA/cm^2

Note the crystallinity of the deposited film as indicated by the sharp Bragg diffraction peaks. A nanostructured material would not have a well-ordered crystal structure since long-range ordering is suppressed by the succession of layers. If layers of Sn and Cu were sequentially deposited at, say, 5 nm intervals then a super-structure peak would be present at a scattering angle of approximately 1.0° using Cu x-ray radiation. Although XRD data below 10° is not presented in Figure 4-8, no such super-structure peak was observed. The deposit is not super-structured, that is, it is not nano-structured and it is not a compositionally modulated alloy (CMA) as desired. In fact the diffraction pattern is well matched by that of Cu_6Sn_5, with a trace amount of Sn. Cu readily alloys with Sn. We believe that significant and complete interdiffusion of Sn and Cu occurs within the film even though layers of different composition were deposited. Production of Sn-rich nanostructures using a Cu/Sn single bath is highly improbable this way.

Instead, the performance of Cu-Sn alloys as working electrodes in Li/Cu-Sn cells as a function of Cu:Sn stoichiometry was investigated. Cu_6Sn_5 films are easily deposited from an aqueous solution containing Cu salt, Sn salt and supporting leveling agents. By varying pulse deposition parameters, a mixture of Cu-Sn alloys can be obtained. When the electrodeposited samples have more than 45% atomic Sn, a mixture of Cu_6Sn_5 and pure Sn phases is expected in accordance with the Cu-Sn phase diagram [4.25]; such is the case in Figure 4-8. By the end of the section it will be shown that as the Sn content in the electrode material is increased, the specific capacity increases at the expense of capacity retention. All references to Cu_6Sn_5 refer to the η'-Cu_6Sn_5 phase.

To deposit films of varying Cu:Sn stoichiometries it was found that the Cu:Sn ratio in the plating bath wasn't as important as the pulse deposition parameters. Small variations in pulse deposition parameters greatly affected the Cu:Sn ratio in the deposited film, whereas small variations in the Cu:Sn ratio in the bath had little effect on film composition. It is possible to control the stoichiometry of the plated deposit using a number of approaches. In one approach, we used the fact that electroplated Sn will exchange with Cu^{2+} in the reaction: $Sn + Cu^{2+}\ (aq) \leftrightarrow Cu + Sn^{2+}\ (aq)$. To verify that this reaction occurs, a film was deposited in the same SnTech plus Cu sulfate solution as described above (1.6 M Sn^{+2} Lucent SnTech + 0.016 M $CuSO_4 \cdot 5 \bullet H_2O$) using a constant current density of 4.0 mA/cm^2. The electrodeposited film was then taken half way out of solution. The top half was exposed to air, and the bottom half was exposed to the plating solution. Figure 4-9a shows a photograph of the film after the lower half had soaked in the plating bath for 24 hours. Figure 4-9b shows the XRD analysis of the top half of the

film revealing Sn and the Ni substrate while Figure 4-9c shows a XRD analysis of the bottom half of the film after soaking.

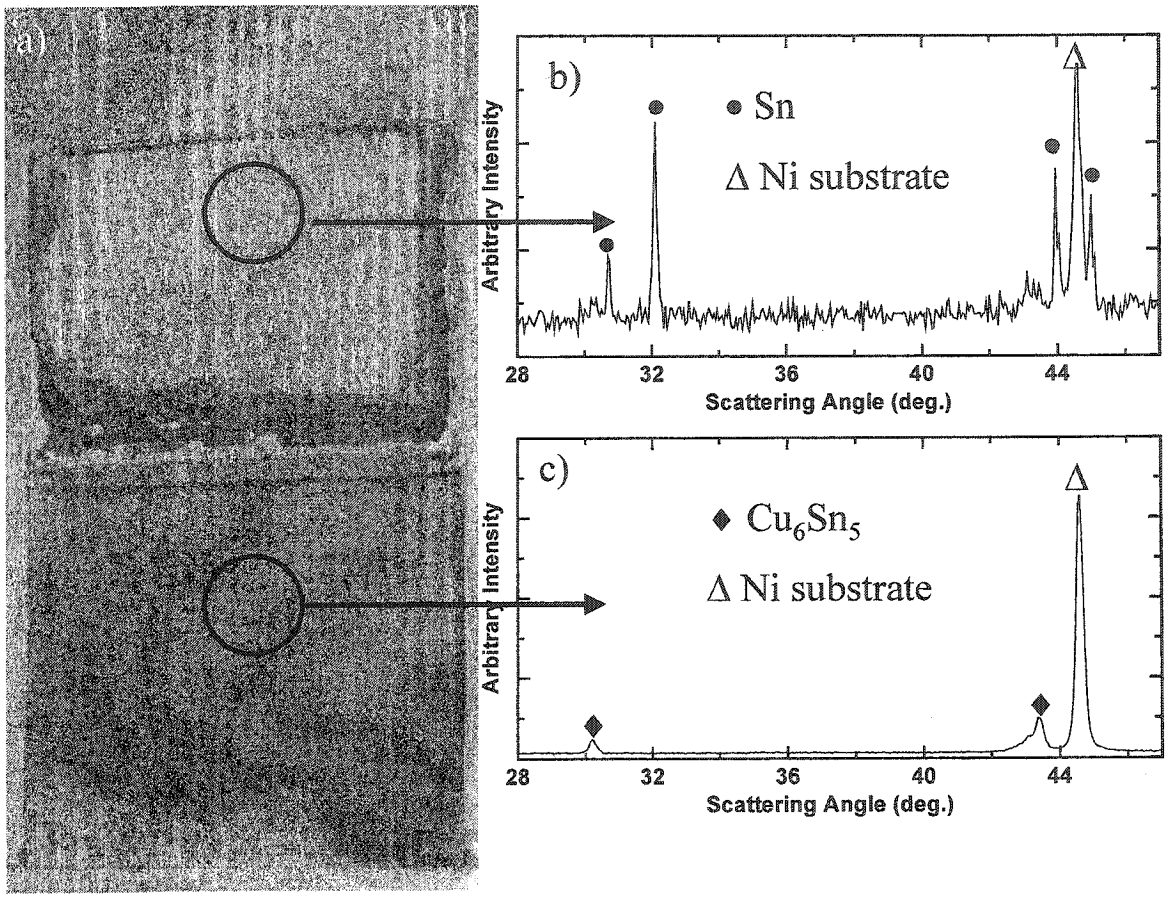

Figure 4-9 Panel a) is a picture of a 5 μm thick film electroplated at a constant current density of 4.0 mA/cm^2 in a 1.6 M Sn^{+2} Lucent SnTech + 0.016 M $CuSO_4 \cdot 5H_2O$ bath. After deposition, half the film was removed from the plating solution and exposed to air. The bottom half-remained in solution overnight. Panel b) is the x-ray diffraction pattern of a sample taken from the top half of the film. Panel c) is the x-ray diffraction pattern of a sample taken from the bottom half of the film after soaking overnight in the plating solution

The entire bottom half has been converted from Sn to Cu_6Sn_5 by the exchange reaction given on the previous page. No Sn phase is present in the bottom half of the film. The

high rate of Cu interdiffusion suggests that films plated using pulsed methods will not have composition variation through their thickness.

To control film stoichiometry the following method was used: Pulse plating conditions set to give nominal 100 nm thick Sn and Cu layers were selected. The amplitude of the low current pulse was varied in the range from 0.08 to 0.20 mA/cm^2 while the high current pulse amplitude was fixed at 4.0 mA/cm^2. The time taken for the low current pulse varies by more than a factor of two over this range, which gives different amounts of time for the exchange reaction to proceed before the plated Sn layers are "buried" under electroplated Cu. Thus, films plated under these conditions with the smallest amplitude of the low current pulse, end up with the most Cu.

Figure 4-10 shows x-ray diffraction patterns for three films prepared under the conditions described above. The thickness of a typical film was 1 μm.

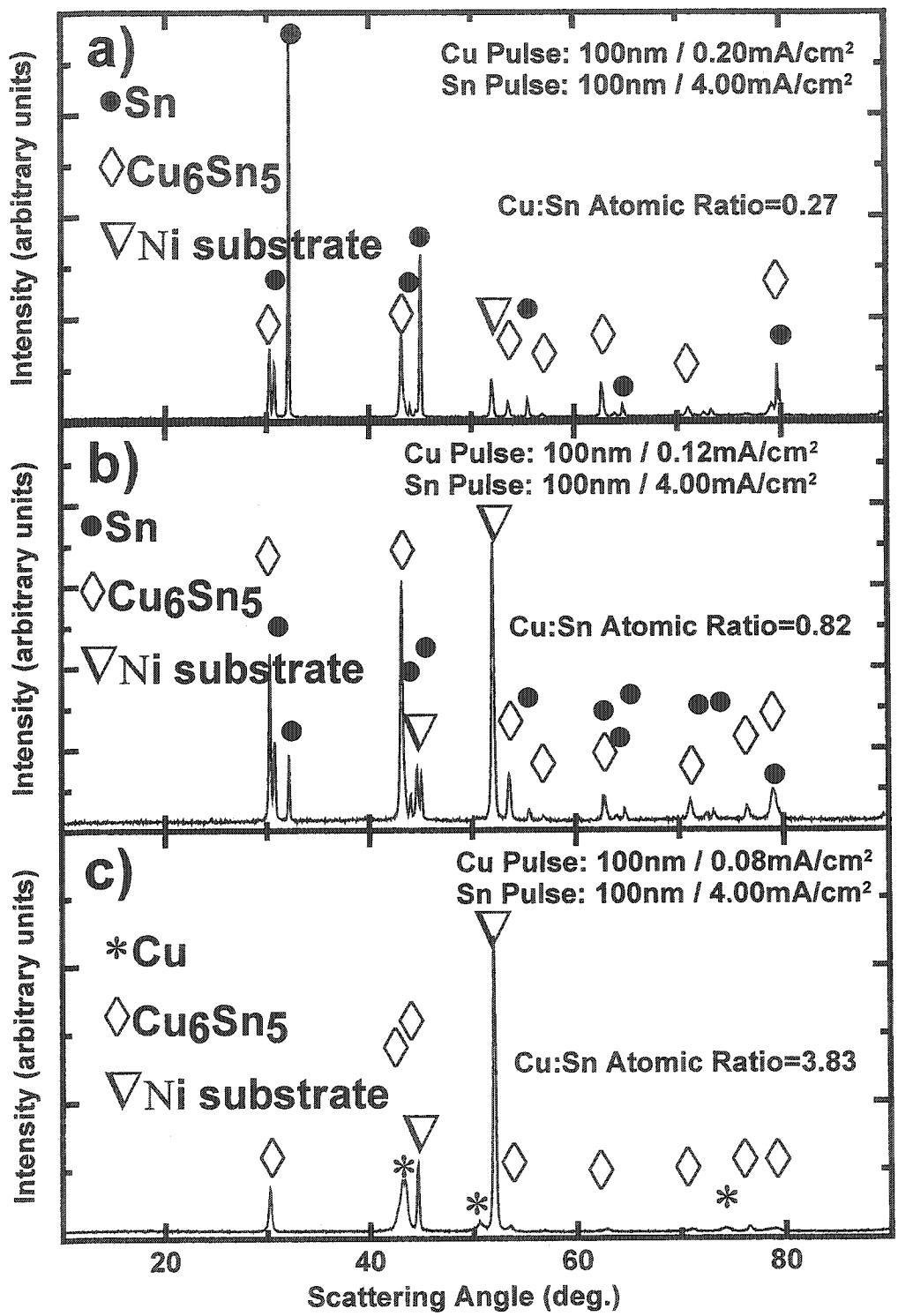

Figure 4-10 X-ray diffraction patterns of three films prepared by pulsed electrodeposition from a Lucent 1.6 M Sn^{+2} SnTech + 0.016 M $CuSO_4 \cdot 5H_2O$ bath. The films were deposited using similar pulse deposition parameters; only the amplitude of the low current density pulse was varied as indicated in the figure legends. The Cu:Sn atomic ratio as determined by EDS is also indicated

All the films contain Cu_6Sn_5 to varying degrees. The films with low current density pulse amplitudes of 0.12 and 0.20 mA/cm^2 also show co-existing Sn, which is expected given their smaller Cu:Sn atomic ratio (see legend) in accordance with the Cu-Sn phase diagram. Energy dispersive spectroscopy (EDS) experiments were conducted on the films to determine average stoichiometry. Table 4-2 shows the EDS results and confirms that the Cu concentration in the films increases when the amplitude of the low current pulse decreases.

Table 4-2 Cu:Sn atomic ratio determined by energy dispersive spectroscopy for electroplated deposits corresponding to the x-ray patterns presented in Figure 4-10

Reference	Cu:Sn Atomic ratio
Figure 4-10a	0.27
Figure 4-10b	0.82
Figure 4-10c	3.83

The Cu-Sn phase diagram is given in Figure 4-11 [4.25]. Using the Cu:Sn atomic ratios obtained by EDS analysis (Table 4-2) the positions on the Cu:Sn phase diagram for the films whose XRD data is given in Figure 4-10 are indicated.

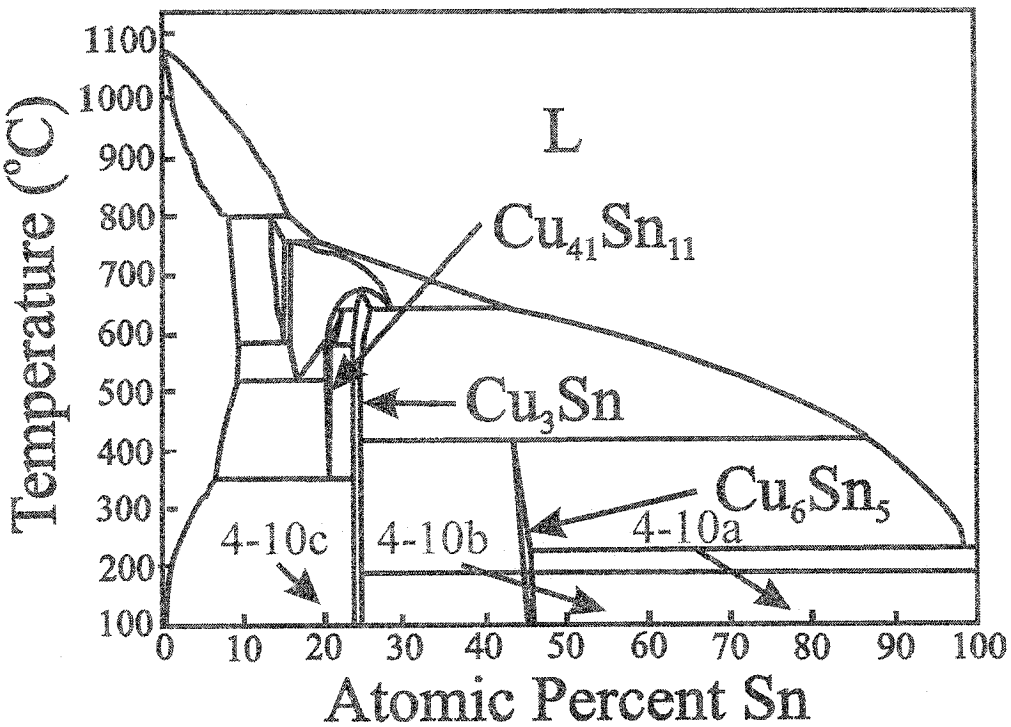

Figure 4-11 The Cu-Sn phase diagram. Using the Cu:Sn atomic ratios obtained by EDS analysis (Table 4-2) the positions on the Cu:Sn phase diagram for the films whose XRD data is given in Figure 4-10 is indicated

The films were deposited at room temperature. The Cu-Sn phase diagram presented in Figure 4-11 begins at 100°C. It is assumed that the phase diagram at room temperature is very similar to that given for 100°C. Figure 4-10a and Figure 4-10b clearly show co-existence of two phases, Sn and Cu_6Sn_5, as expected from their position indicated on the Cu-Sn phase diagram. From the phase diagram, Figure 4-10c should also show co-existing phases, Cu and Cu_3Sn. It does not. Instead, Cu and Cu_6Sn_5 are present. Apparently, the Cu and Cu_6Sn_5 phases are favored by the plating procedure used here, while Cu_3Sn is not.

Voltage versus specific capacity and specific capacity vs. cycle number graphs for a Li/electroplated Cu_6Sn_5 cell are shown in Figure 4-12. The voltage window for the first

three cycles was between 0 and 1.3 V, with a current density of 30 mA/g (72 $\mu A/cm^2$). On the fourth cycle the voltage window and current density were both reduced, to between 0.2 and 1.3 V and to 15 mA/g (36 $\mu A/cm^2$) respectively.

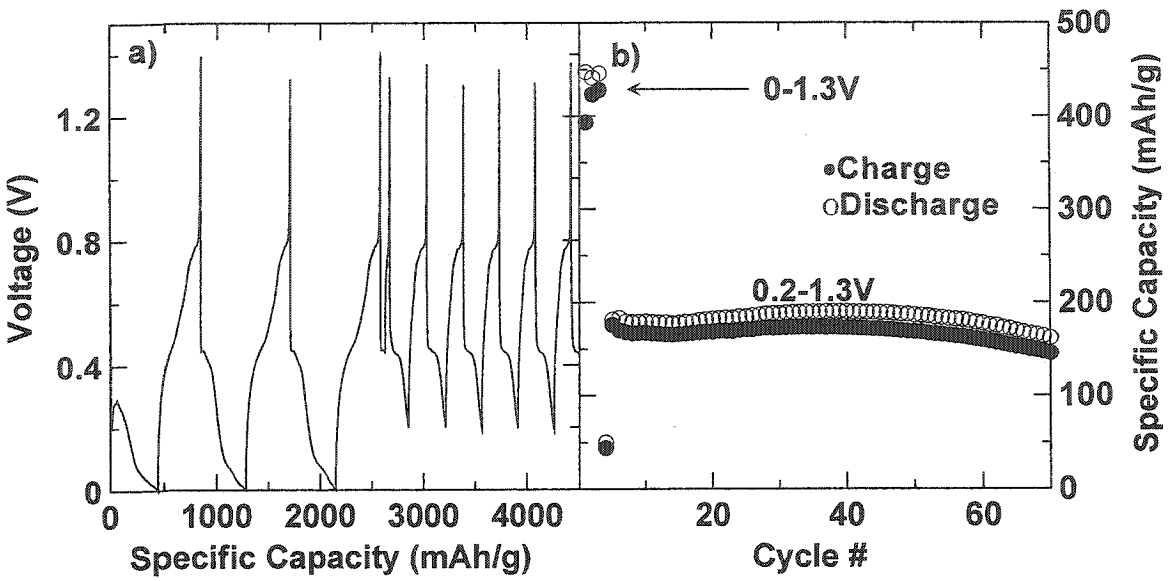

Figure 4-12 Voltage vs. specific capacity and specific capacity vs. cycle number for a Li/Cu_6Sn_5 cell using a Cu_6Sn_5 film deposited from a 1.6 M Sn^{+2} SnTech + 0.016 M $CuSO_4 \cdot 5H_2O$ bath using pulsed deposition at current densities of 0.08 mA/cm^2 and 4.00 mA/cm^2. The voltage window for the first three cycles was between 0 and 1.3 V, with a current density of 30 mA/g (72 $\mu A/cm^2$). During the fourth cycle the voltage window and current density were both reduced, to between 0.2 and 1.3 V and to 15 mA/g (36 $\mu A/cm^2$) respectively

Figure 4-8 shows the x-ray diffraction pattern of the film used to produce the data presented in Figure 4-12. Aside from the Ni foil substrate and trace amounts of Sn, Cu_6Sn_5 is the major phase present. When cycled between 0 and 1.3 V, the cell had a capacity of approximately 450 mAh/g. When the voltage window was limited to between 0.2 and 1.3 V the capacity was reduced to approximately 170 mAh/g. In [4.26-27] it was shown that by limiting the voltage window, capacity retention is improved by limiting Cu

expulsion. The data presented above agree with the results presented in [4.27]. For more information regarding phase structure and electrochemical performance of Cu_6Sn_5 alloys in Li cells refer to [4.27].

Note that anomalous, high-voltage irreversible capacity (discussed in section 4.1) was not observed. This was true for all the Cu-rich Cu-Sn electrodes tested. Cells cycled well above 2.0 V did not show the AHVIC observed in pure Sn cells. The presence of Cu seems to eliminate the catalytic activity of Sn. This is a simple and effective way to avoid the catalytic behavior.

Figure 4-13 shows the specific capacity versus cycle number for two Li/Cu_6Sn_5 cells. Both cells were made from a Cu_6Sn_5 film deposited in a 1.6 M Sn^{+2} SnTech + 0.016 M $CuSO_4 \bullet 5H_2O$ bath using pulsed deposition at current densities of 0.08 mA/cm^2 and 4.00 mA/cm^2 (the XRD analysis of this film is given in Figure 4-10c). Two samples were cut from the film and made into Li/Cu_6Sn_5 cells.

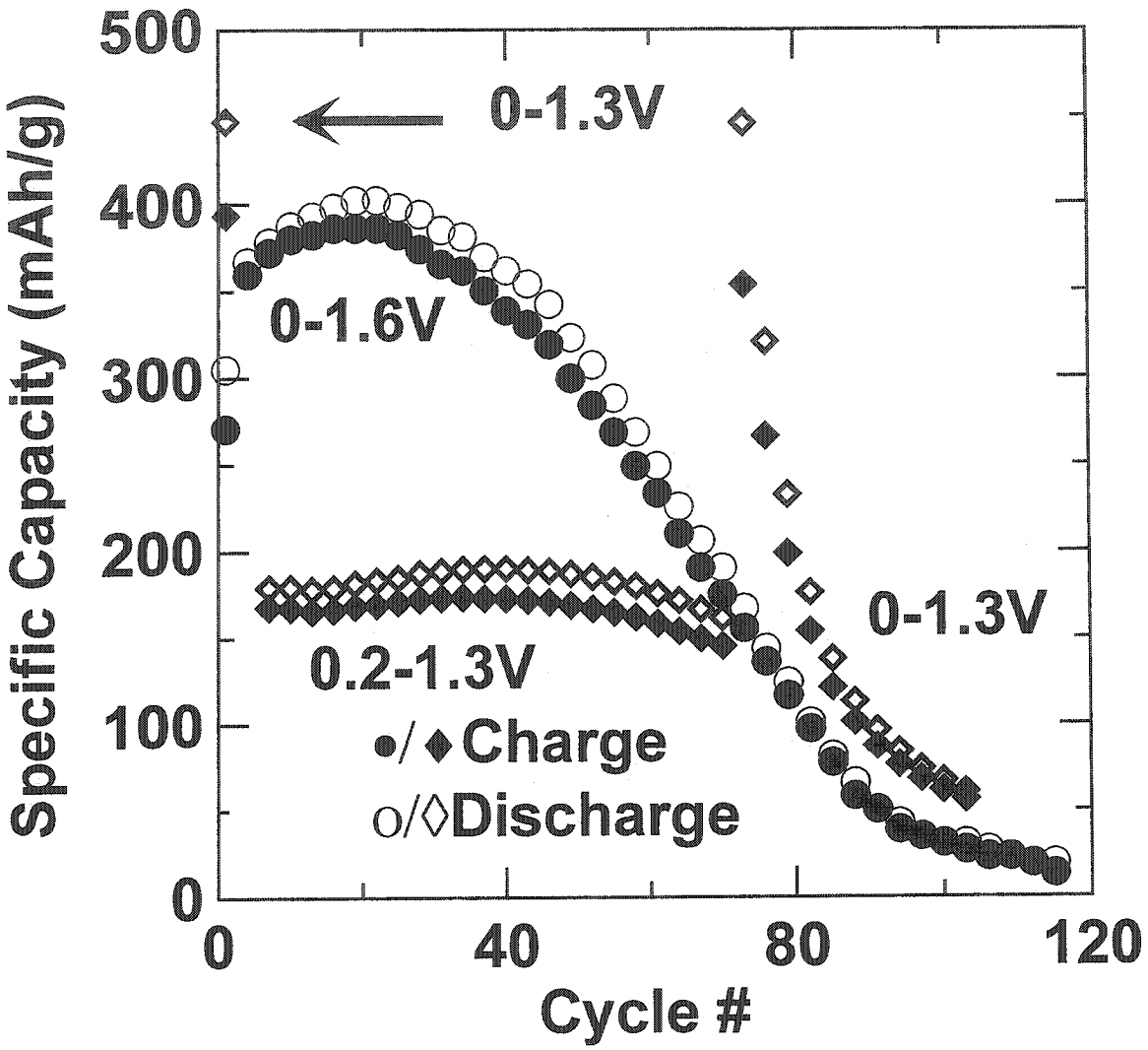

Figure 4-13 Specific capacity vs. cycle number for two Li/Cu_6Sn_5 cells using different voltage windows. Both cells were made from a Cu_6Sn_5 film deposited in a 1.6 M Sn^{+2} SnTech + 0.016 M $CuSO_4 \cdot 5H_2O$ bath using pulsed deposition at current densities of 0.08 mA/cm^2 and 4.00 mA/cm^2. The cell represented by diamond-shaped data points was initially cycled between 0 - 1.3 V at 30 mA/g (72 μA/cm^2). The voltage window and current density were then reduced to 0.2 - 1.3 V and to 15 mA/g (36 μA/cm^2) respectively. The cell represented by circular data points was cycled between 0 - 1.6 V at 98.9 mA/g (210 μA/cm^2)

The cell represented by diamond-shaped data points was initially cycled between 0 - 1.3 V at 30 mA/g (72 μA/cm^2), resulting in a capacity of approximately 450 mAh/g. The voltage window and current density were then reduced to 0.2 - 1.3 V and to 15 mA/g

(36 $\mu A/cm^2$) respectively, resulting in a capacity of about 170 mAh/g. The cell represented by circular data points was cycled between 0 - 1.6 V at 98.9 mA/g (210 $\mu A/cm^2$). A peak capacity of ~400 mAh/g was observed around cycle #20. Capacity dramatically declines after ~40 cycles. By contrast, the capacity was much better for the cell cycled between 0.2 and 1.3 V. When the voltage window for the latter cell was increased from 0.2 - 1.3 V to 0 - 1.3 V (cycle #72), the specific capacity increased from about 150 to about 500 mAh/g, then fell below 100 mAh/g within about 15 cycles. These results show the same trend as the data presented in [4.27] for powdered Cu_6Sn_5 samples.

Figure 4-14 shows the discharge capacity versus cycle number for two Li/(Cu-Sn) cells cycled between 0 and 1.6 V. The electroplated films used were the ones whose x-ray patterns are shown in Figure 4-10a and Figure 4-10c.

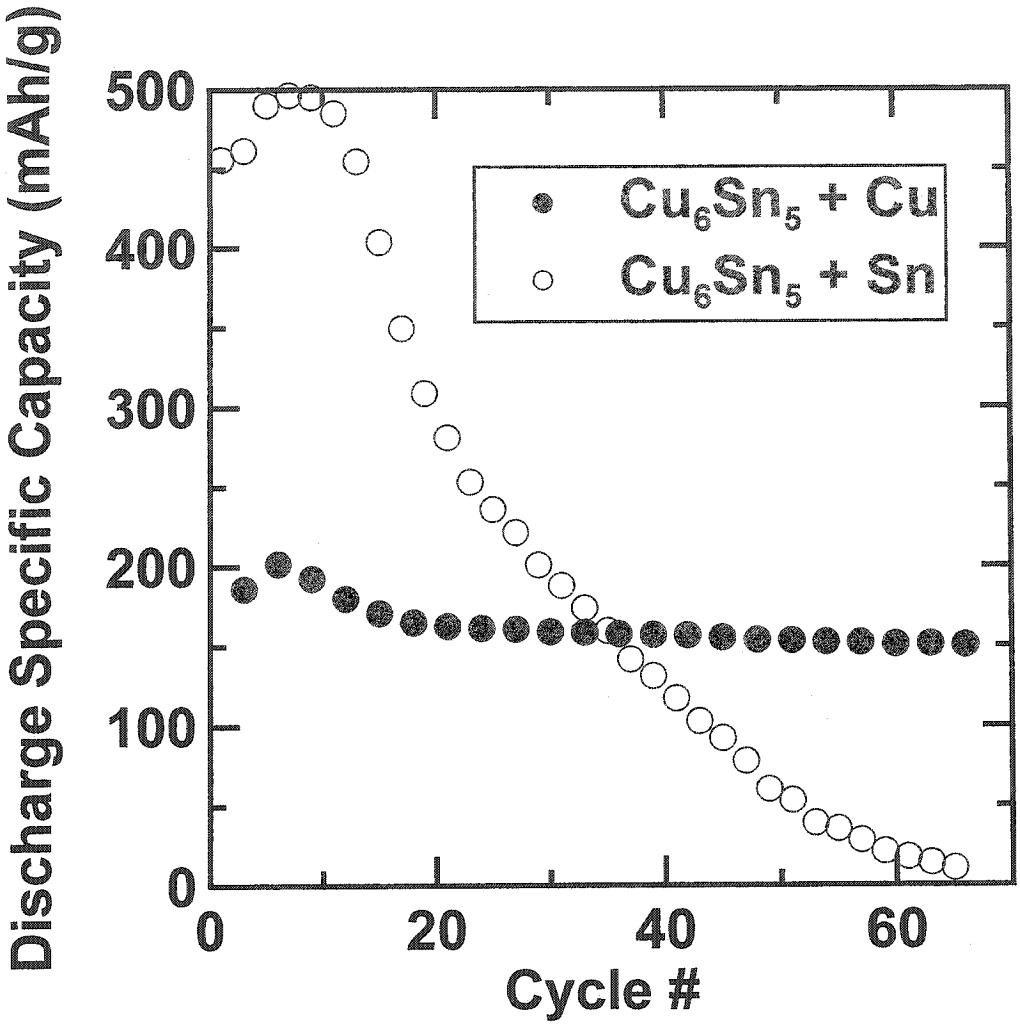

Figure 4-14 Capacity vs. cycle # data from two Cu-Sn/Li cells with different Cu:Sn ratios

The film described by Figure 4-10c consists of two phases: Cu_6Sn_5 and Cu, while the film described by Figure 4-10a is a mixture of Cu_6Sn_5 and Sn. The cell represented by the solid circles (low Sn content) in Figure 4-14 (x-ray in Figure 4-10c) was cycled at 19.7 mA/g (49.2 $\mu A/cm^2$) between 0 and 1.6 V. The cell represented by the hollow circles (high Sn content) in Figure 4-14 (x-ray from Figure 4-10a) was cycled at 84.7 mA/g (379 $\mu A/cm^2$) between 0 and 1.6 V. As the Sn content increases, the specific capacity increases at the expense of capacity retention. The data set corresponding to the

largest Sn content has a peak specific capacity of ~500 mAh/g (Figure 4-14, hollow circles). By cycle #40 the capacity was reduced to ~100 mAh/g, an 80% loss of capacity. As Sn content is reduced, specific capacity suffers while capacity retention improves (Figure 4-14, solid circles). The data set corresponding to Cu_6Sn_5 plus Cu (Figure 4-14, solid circles) had a much lower specific capacity, peaking at approximately 200 mAh/g. By cycle #40 capacity was reduced to ~160 mAh/g, a 20% loss of capacity. The more Cu in the film the better the capacity retention, and the lower the specific capacity.

This section showed that the the addition of Cu to a Sn electrode greatly improved its cyclability, at the expense of specific capacity. Furthermore, anomalous high-voltage irreversible capacity is not observed. It was shown that the specific capacity and cyclabilty of a Cu-Sn electrode can be tuned by selecting the Cu-Sn content. However, the optimal composition capable of both large capacity cycling with good cyclability has not necessarily been discovered. In fact, we have tested only a few possible compositions in the rich Cu-Sn phase diagram. The next task is to determine which Cu-Sn alloy has the largest capacity with acceptable cyclability.

4.3 Combinatorial Electrodeposition

In section 4.2 it was shown that the capacity and cyclability of Cu-Sn/Li cells is highly dependent on the composition of the Cu-Sn electrode. The obvious question to ask is: "Which composition makes the best electrode?" The traditional way of doing things would be to fabricate a range of individual Cu-Sn alloys with varying compositions and test them one at a time. This is time consuming and expensive.

Instead, a combinatorial material science strategy was adopted, whereby numerous compositions are fabricated in a single experiment.

Sputter or vapor deposition is typically used to perform combinatorial material science [4.28-32]. A film is deposited where the atomic ratio between atom A and B (or A, B, C if desired) varies as a function of position along the sputtered film. For example, alternating layers of Sn and Mo can be deposited on a substrate where the Sn:Mo ratio varies as a function of position on the substrate. Individual coupons from the film would be cut and tested in Li cells to determine which Sn:Mo ratio resulted in the best cycling performance. The process of fabricating a series of similar materials in a single experiment is sometimes referred to as combinatorial materials synthesis. This is a powerful research tool.

We wanted to combine the power of combinatorial material synthesis with the simplicity of electrodeposition.

4.4 A combinatorial library of Cu-Sn alloys

In the sections to follow the development of combinatorial electrodeposition methods for use in the study of advanced metal-alloy electrodes for Li-ion batteries will be discussed.

4.4.1 Electroplating strategy

In order to prepare the composition-spread library of Cu-Sn alloys, several requirements must be satisfied. Since Cu deposits at a more positive potential (0.342 V vs. SHE) than Sn (-0.137 V vs. SHE) and therefore more easily, the Sn concentration in solution should be much larger than that of Cu. The bath should have poor "throwing"

power. The bath constituents determine throwing power. An example of a bath with poor throwing power is the bronze pyrophosphate bath given in Table 2-1 (Bronze 2). By using a Hull cell and a bath with poor throwing power the current density will vary along the length of the working electrode (refer to Figure 2-8). This ensures that the thickness of the deposit varies with position on the substrate foil. Finally, pulsed deposition is used to create the composition-spread. A series of on-off pulses are used. Primarily Sn is deposited during the on pulse. During the off pulse Cu^{+2} ions from solution ion-exchange with Sn atoms (this is sometimes called immersion plating), according to the reaction: $Cu^{+2}(aq) + Sn(s) \leftrightarrow Cu(s) + Sn^{+2}(aq)$. Table 4-3 shows the SHE reduction potentials for Cu, Sn and the Cn-Sn exchange reaction. A negative ΔG in Table 4-3 indicates spontaneity. A deposit like that shown in Figure 4-15 is created.

Table 4-3 Standard hydrogen electrode (SHE) potentials and change in free energy for the electrodeposition of Cu and Sn

Reaction	SHE Potential (V)	ΔG (eV) / atom
$Sn^{+2} + 2e \Rightarrow Sn$	-0.137	0.274
$Cu^{+2} + 2e \Rightarrow Cu$	0.342	-0.680
$Sn + Cu^{+2} \Rightarrow Sn^{+2} + Cu$		-0.954

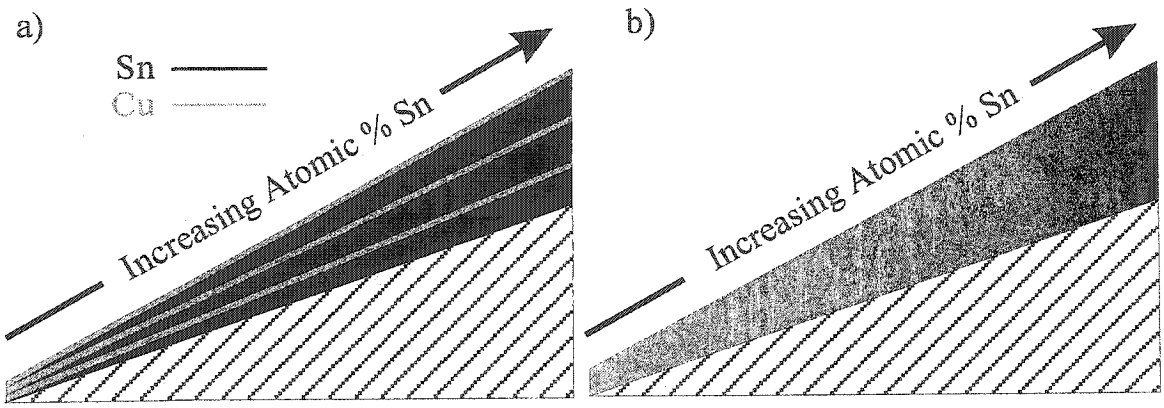

Figure 4-15 a) A schematic of the film structure expected using on/off pulsed deposition in a Hull Cell with a Sn pyrophosphate solution containing a small amount of Cu pyrophosphate in the absence of solid-state interdiffusion. b) A schematic of the actual film stoichiometry due to interdiffusion

Figure 4-15a shows layers of Sn-rich material deposited during the on pulses, whose thickness varies along the length of the substrate electrode, and layers of ion-exchanged Cu deposited during the off pulses, whose thickness is constant along the length of the substrate electrode. In our deposition experiments, the on-pulse/off-pulse sequence is repeated hundreds of times to deposit a film several micrometers thick. During the on-pulse, the deposited layer thickness is estimated to range between 1.3 and 4.7 nm along the length of the substrate. Examinations of the film using small angle x-ray scattering (SAXS) showed that a composition modulated superlattice structure was not formed. Presumably, this is because the Cu-rich and Sn-rich layers are eliminated by interdiffusion. Therefore, Figure 4-15b shows a more realistic schematic of the deposited film after Cu-Sn interdiffusion occurs.

Figure 4-16 shows that the procedure described above deposits a film where the average stoichiometry varies along the length of the substrate.

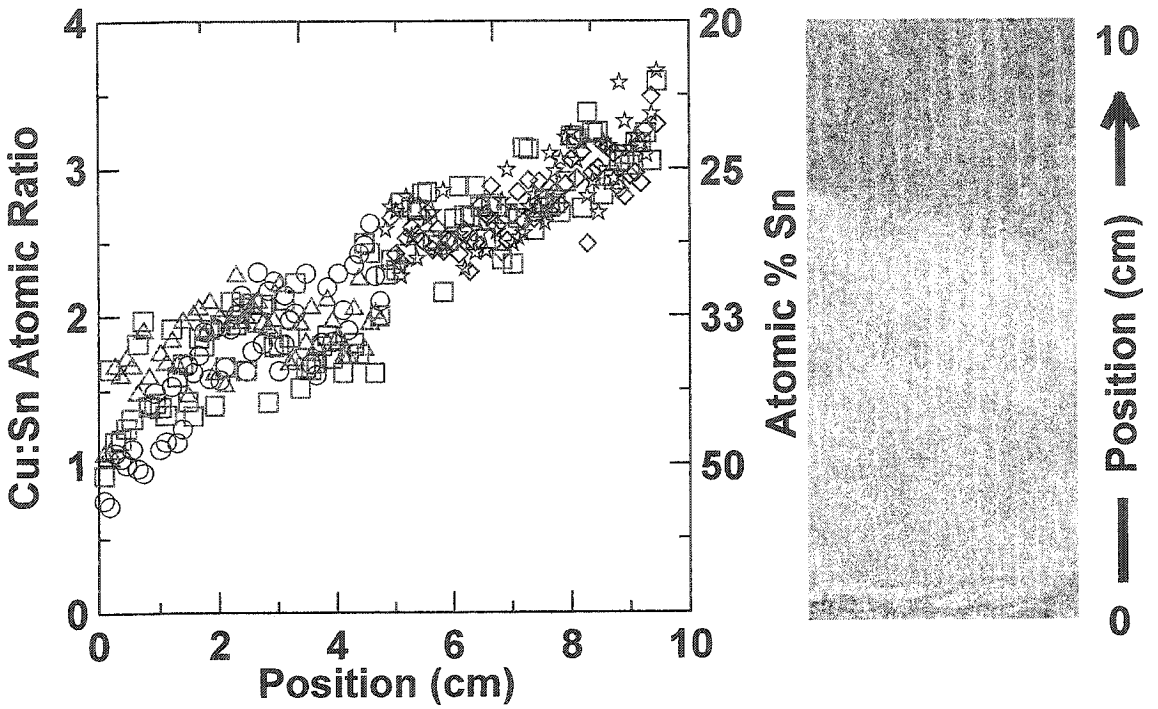

Figure 4-16 Cu:Sn atomic ratio and atomic % Sn as determined by electron microprobe analysis versus position on the electrodeposited film. The various symbols correspond to six separate scan lines measured along the film. An optical image of the deposited film is shown on the right

Each EDS data point in Figure 4-16 represents a 40 μm × 40 μm area. In that area many crystallites are sampled simultaneously and each crystallite does not necessarily have the same composition. Figure 4-17 shows an electron micrograph of the surface of the film with squares indicating the approximate size of the probe beam.

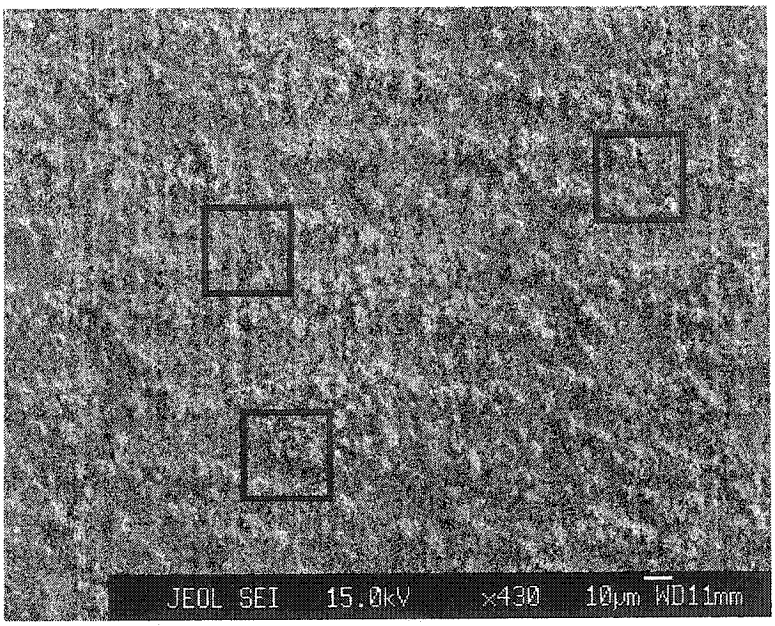

Figure 4-17 An SEM image of the deposited film. The size of the 40 μm electron probe beam is indicated by the squares. Different numbers of large crystallites are sampled from place to place along the film, causing scatter in the electron microprobe data of Figure 4-16

For the three indicated positions of the squares there are varying numbers of large crystallites present. Large crystallites are rich in Sn, so if the beam is analyzing an area with a large number of crystallites, a large Sn concentration will be detected. Instead, if the beam is sampling an area with very few crystallites the Sn concentration will be low. Between adjacent points the number of crystallites being analyzed can vary. This variation can result in a significant difference in the Cu:Sn atomic ratio between adjacent points, causing scatter in the data, as seen in Figure 4-16. Nevertheless, it is clear that the average stoichiometry inferred from Figure 4-16 varies in a roughly linear manner.

4.4.2 Discussion

Figure 4-16 shows that a film where the Cu:Sn atomic ratio varies along the length of the film has been deposited. Using the electron microprobe results the atomic percent Sn can be determined along the length of the film (approximated in Figure 4-16, right ordinate). Then, the composition of the film can be mapped onto the Cu-Sn phase diagram (Figure 4-18). The double-headed arrow in Figure 4-18 shows the range of compositions sampled by the deposited film. In theory, using our deposition procedure, any compositional range could be easily sampled.

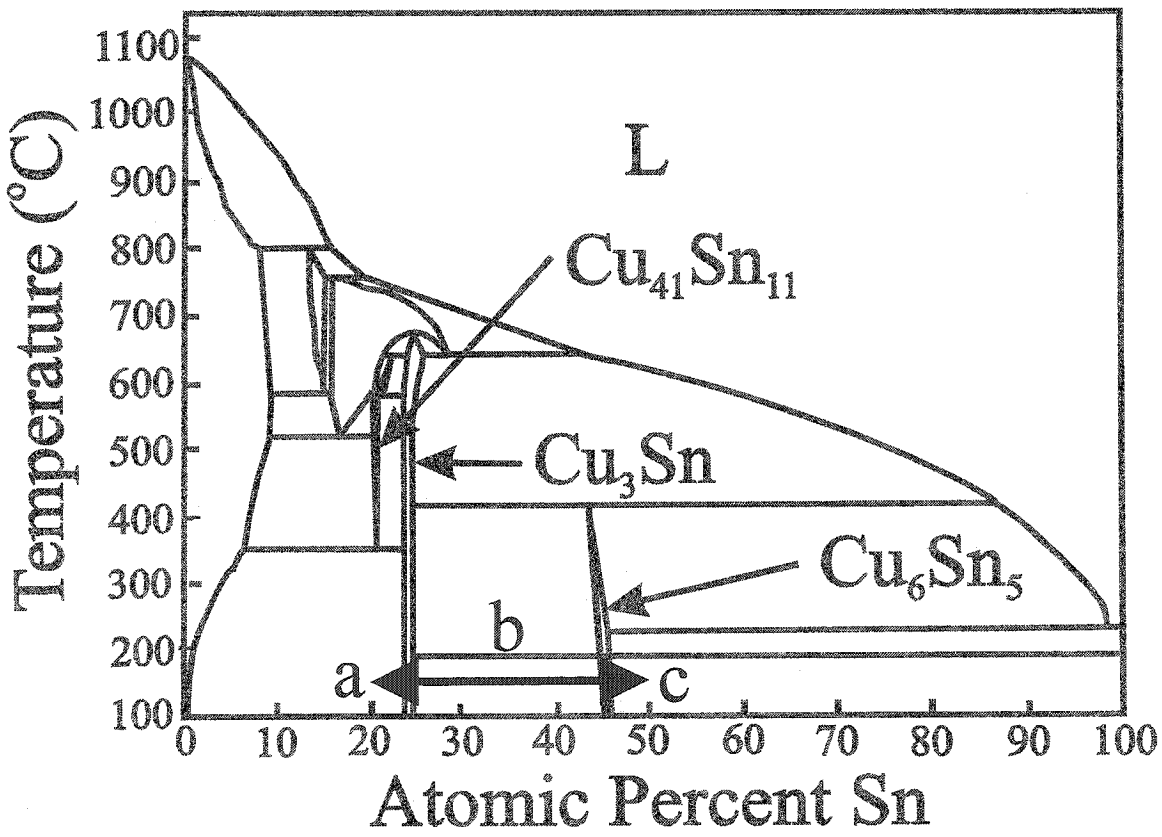

Figure 4-18 The Cu:Sn phase diagram. The double-headed arrow indicates the region of phase space sampled by the film (Figure 4-16, right hand side) deposited in the Hull cell using on/off pulsed deposition. Three compositions labeled a, b and c are considered for focused study

Electrodeposition was performed at room temperature, however the tabulated phase diagram only extends as low as 100°C. It is assumed that the phase diagram at 21°C is identical to that at 100°C. All samples in this section were either prepared and studied at room temperature or were annealed at 200°C under argon. Between 20 and 200°C, the arrow in Figure 4-18 passes through five distinct regions: Sn + Cu_6Sn_5, Cu_6Sn_5, Cu_6Sn_5+Cu_3Sn, Cu_3Sn and Cu_3Sn + Cu.

Three positions in the phase diagram (Figure 4-18) were chosen for focused study: a high Cu content (Figure 4-18a), a high Sn content (Figure 4-18c) and an intermediate area (Figure 4-18b). According to the phase diagram, Figure 4-18a should correspond to co-existing phases of Cu_3Sn + Cu. Figure 4-18b should correspond to co-existing phases of Cu_6Sn_5+Cu_3Sn. Figure 4-18c should correspond to co-existing phases of Sn + Cu_6Sn_5. The entire film was annealed under argon at 200°C for two hours, then x-ray diffraction patterns were taken along its length (top to bottom in Figure 4-16).

Figure 4-19 shows XRD patterns taken from the positions labeled a-c in Figure 4-18, correspondingly labeled a-c. XRD patterns taken from pure Sn and known Cu-Sn alloys are superimposed onto those XRD patterns. Known Cu-Sn alloys were obtained by melt-spinning. $Cu_{41}Sn_{11}$, Cu_3Sn and Cu_6Sn_5 alloys were prepared by mixing high-purity (>99%) Cu and Sn powders in the proper stoichiometric ratios and then were melt spun by Andy George. XRD analysis was then performed on the melt-spun samples.

In Figure 4-18a co-existing Cu_3Sn + Cu phases are expected from the phase diagram, but they are not observed. Instead, the $Cu_{41}Sn_{11}$ phase, which does not extend down to room temperature in Figure 4-18, is present. Apparently, $Cu_{41}Sn_{11}$ is favored by the pulsed deposition process described above, rather than Cu or Cu_3Sn. The peak near

42° in Figure 4-19a is thought to arise from a Cu phase containing a small amount of dissolved Sn. In Figure 4-19b, the $Cu_{41}Sn_{11}$ phase is present once again, where Cu_3Sn is expected. The fact that films fabricated by electrodeposition do not exactly follow the equilibrium conditions present in a phase diagram at a specified temperature is not surprising, since electrodeposition does not occur under equilibrium conditions. The $Cu_{41}Sn_{11}$ phase is in the right stoichiometric range in the Cu-Sn phase diagram to appear in Figure 4-19a and Figure 4-19b, but is not expected at lower temperatures. As discussed, the Cu_3Sn phase is not expected at high Cu content. $Cu_{41}Sn_{11}$ is expected instead of Cu_3Sn, therefore the XRD pattern presented in Figure 4-19b should show co-existing phases of $Cu_{41}Sn_{11}$ and Cu_6Sn_5. Figure 4-19b does show co-existing phases of $Cu_{41}Sn_{11}$ and Cu_6Sn_5. Furthermore, at position c in Figure 4-18, co-existing Cu_6Sn_5 and Sn is expected, as verified by the diffraction pattern in Figure 4-19c. Electron microprobe results and XRD results agree with the Cu-Sn phase provided that the $Cu_{41}Sn_{11}$ phase is expected at high Cu content.

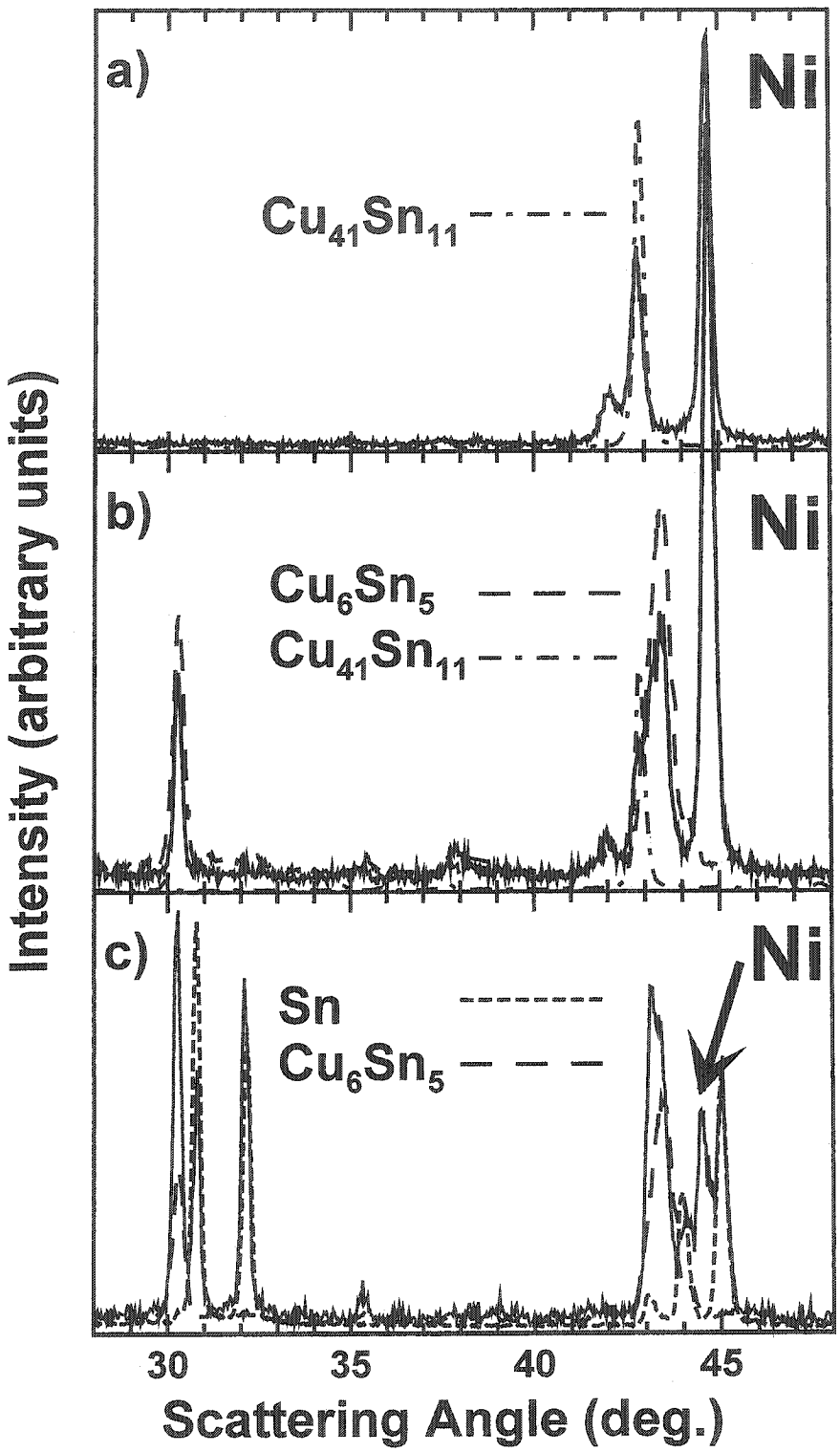

Figure 4-19 X-ray diffraction patterns of portions of the film corresponding to positions a-c in Figure 4-18. Known Sn and Cu-Sn alloy XRD patterns are superimposed on the data for comparison

Figure 4-20 shows XRD patterns along the length of the composition-spread film starting from the bottom (that is, the part of the film closest to the counter electrode during deposition) up to the top of the film (furthest from the counter electrode during deposition and therefore Cu-rich). The patterns that were the subject of the focussed study in Figure 4-19 (labeled a-c) are indicated in Figure 4-20. The XRD patterns at the bottom of the film are rich in Sn. As the patterns progress up the film, towards the Cu-rich end of the film, peaks from the XRD pattern of Sn steadily decrease and disappear approximately one-third of the way up. Approximately two-thirds up the film, peaks from the Cu_6Sn_5 phase also disappear. Correspondingly, XRD peaks of Cu-rich alloys begin to emerge. There is a smooth transition between Sn-rich and Cu-rich alloys.

In Figure 4-20 the scan below labeled scan b (or 10 scans up from the bottom) has an unusual double peak near 44.6°. A single peak is expected due to the Ni substrate, as observed in the other scans. The double peak is the result of an experimental error. Double-sided tape is used to secure the electrodeposited film to the XRD sample holder during x-y measurement-move operations. In this case, the film did not properly adhere to the tape and part of the film peeled. Due to peeling the x-ray beam effectively sampled the same film at two different heights. This resulted in the double peak pattern seen near 44.6°, as well as slight broadening of the peaks at lower angles.

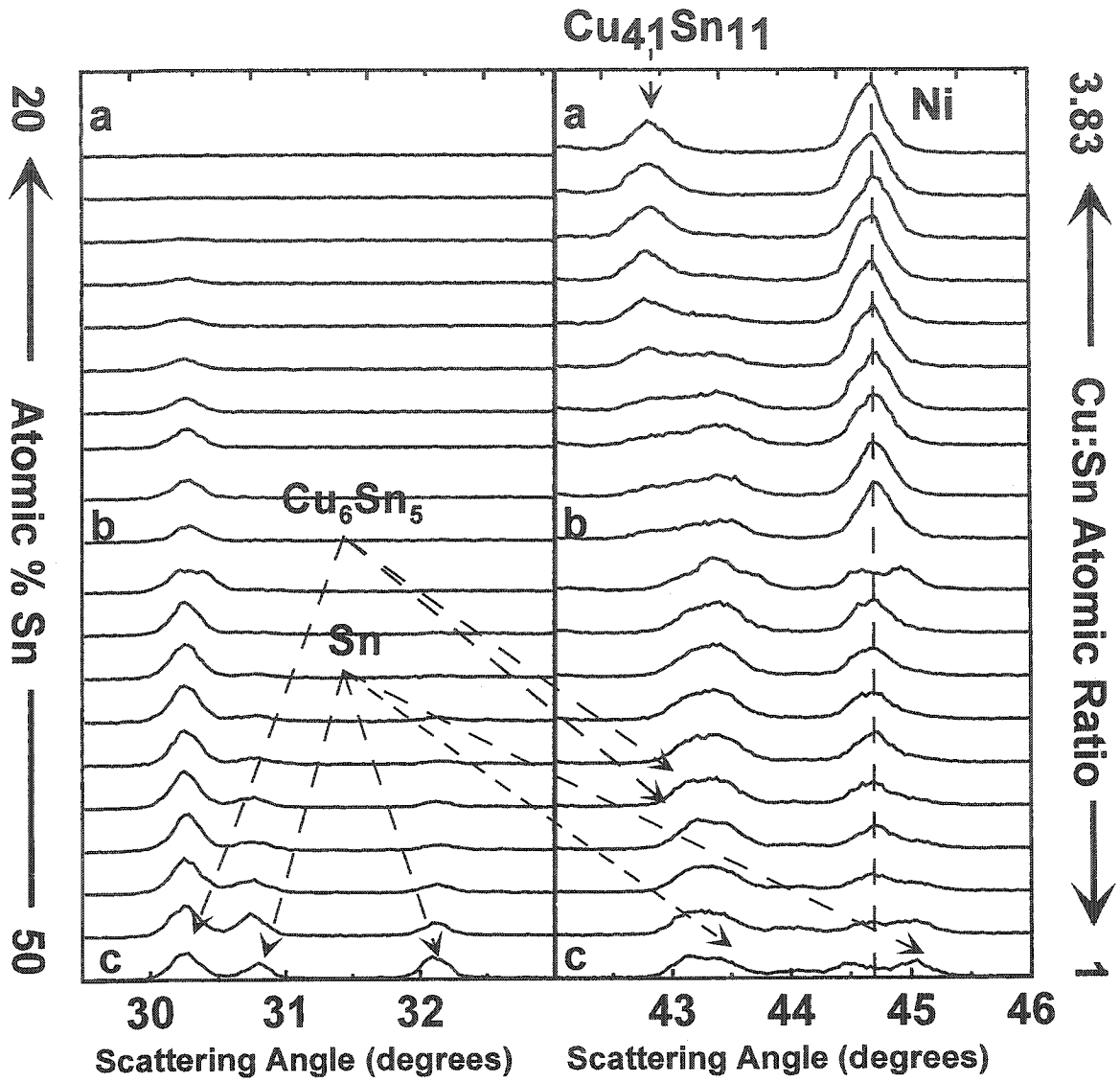

Figure 4-20 Twenty XRD patterns measured at equal spacing along the length of the film. The Cu content increases from bottom to top. Sn-rich phases are observed at the bottom of the film, while Cu-rich phases are observed at the top. Bragg peaks from known phases are indicated

Li/Cu-Sn coin cells were then constructed from circular electrodes punched from various places on the film. Figure 4-21 shows specific capacity vs. cycle number and voltage vs. capacity for five selected electrodes taken along the length of the film. Each cell was cycled between 0 V and 1.2 V. Figure 4-21a and Figure 4-21b correspond to an

electrode taken from the Sn-rich end of the film. Figure 4-21i and Figure 4-21j correspond to an electrode taken from the Cu-rich end of the film. The trends in Figure 4-21 are obvious and expected. It is well known that Sn-rich compounds exhibit large capacity but poor capacity retention [4.1]. It has also been shown that pure Cu-Sn intermetallic phases like Cu_6Sn_5 exhibit lower capacities than Sn-rich materials, but have dramatically improved capacity retention [4.26-27]. Figure 4-21c-h progressively illustrate the effect of increasing Cu content. It shows that high Sn content films have higher capacity and poor capacity retention while high Cu content films have lower capacity and dramatically improved capacity retention. The extra Cu acts like "glue" to hold the electrode together. The addition of Cu limits the total volume expansion of the electrode thereby reducing loss of capacity due to cracking and pulverization.

The data represented in Figure 4-21 was obtained from cycling five electrodes with five different compositions. The approximate compositions for each electrode, expressed in atomic % Sn, are indicated in Figure 4-21. Solid dots in Figure 4-21 represent discharge capacity, hollow dots represent charge capacity. Theoretical discharge capacity can be calculated from atomic % Sn. Theoretical discharge capacity for each cell is indicated by an arrow.

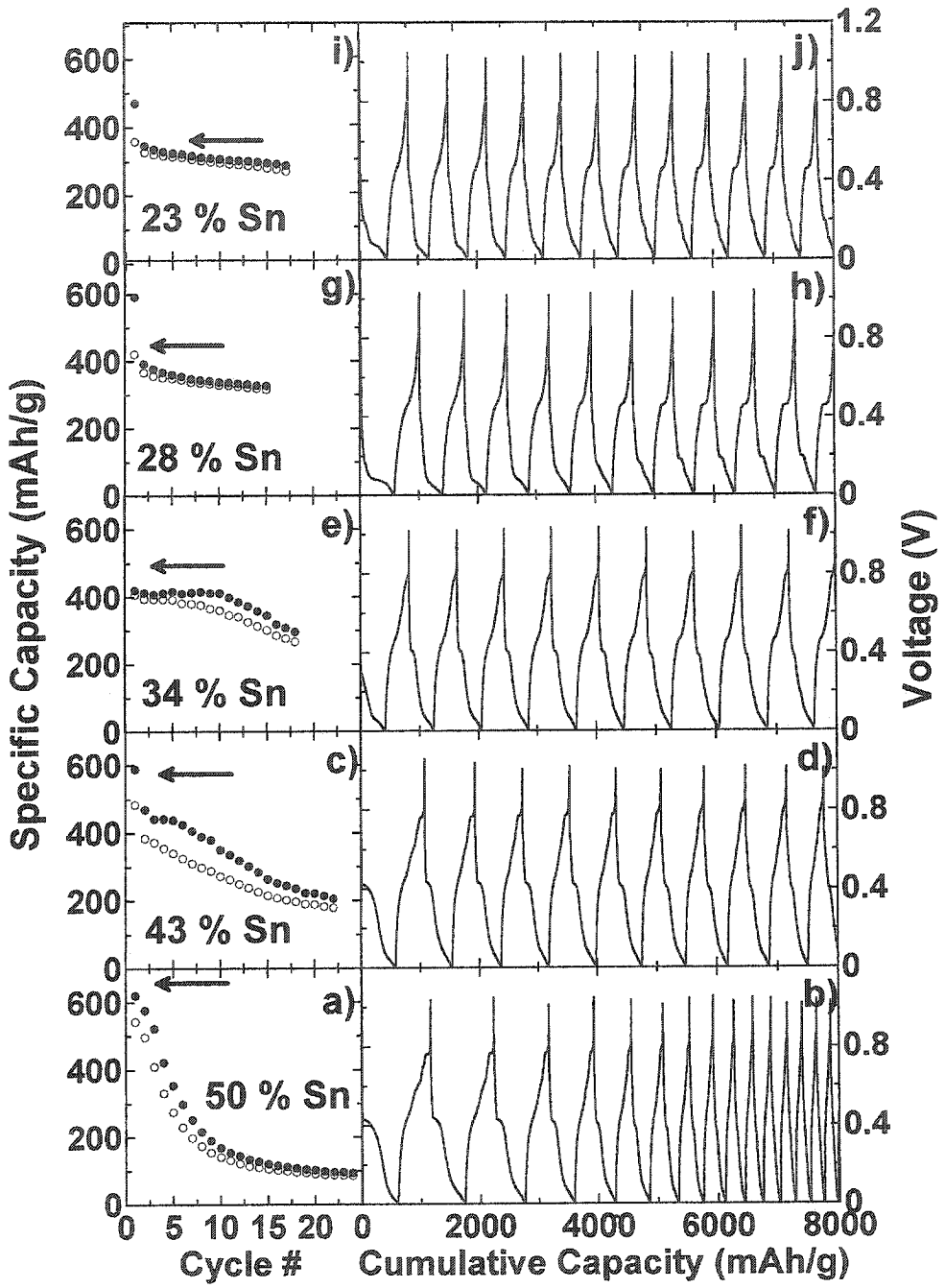

Figure 4-21 Capacity versus cycle number and voltage versus capacity for five Li/Cu-Sn cells where the electrodes were sequentially cut along the length of the electrodeposited composition-spread film. The Cu content increases from bottom to top. The specific capacity decreases with increasing Cu content with a corresponding increase in capacity retention. The theoretical discharge capacity for each cell is indicated by an arrow

Using electrodeposition, a combinatorial library of binary $Cu_{1-x}Sn_x$ alloys has been successfully deposited from a single bath in a single run. The Cu:Sn atomic ratio varies almost linearly along the length of the film. Electron microprobe and XRD data agree with the Cu-Sn phase diagram except that the high temperature $Cu_{41}Sn_{11}$ phase was observed in place of Cu_3Sn. Electrochemical studies of Li/Cu-Sn cells show that Sn-rich regions of the film (e.g.: $Sn_{0.5}Cu_{0.5}$) exhibit high capacity (~600 mAh/g) but poor capacity retention. Cu-rich compounds (e.g.: $Sn_{0.2}Cu_{0.8}$) exhibit lower capacity (~300 mAh/g) with dramatically improved capacity retention. From this data set the composition exhibiting both good cyclability and high capacity would be approximately 28 atomic % Sn.

In the next section the power of combinatorial electrodeposition will be applied to a different binary alloy system, Cu-Zn

4.5 The Cu-Zn system and scalabilty of combinatorial electrodeposition

Combinatorial electrodeposition is easily applied to other binary systems. Next, the scalability of combinatorial electrodeposition methods will be explored using brass alloys as an example.

Seven Cu-Zn alloys with different compositions were prepared, in bulk, by one-at-a-time electrodeposition methods. The composition and structure of these alloys are compared to alloys prepared by combinatorial methods. It will be shown that Cu-Zn alloys prepared using combinatorial methods via electrodeposition are representative of bulk alloys prepared by one-at-a-time methods. The brass bath from Table 2-1 was used to deposit both individual alloys and the composition-spread film.

4.5.1 Results

All deposition runs used a Zn anode as the counter electrode since the solution is predominantly Zn (23:1 molarity Zn:Cu). To prepare the Cu-Zn composition-spread film a current of 75 mA was applied to the Hull cell discussed in section 2.2.4 for 0.9 hrs (note this is not pulse plating, as was used in the Cu-Sn system). Due to the geometry of the Hull cell and poor throwing power of the pyrophosphate bath, a current density gradient was established along the length of the oblique angled electrode.

The deposition potential was low enough to deposit both Cu and Zn. Cu (0.342 V vs. SHE) has a more positive standard hydrogen electrode (SHE) reduction potential than Zn (-0.763 V vs. SHE), so it will deposit preferentially. However, the Zn concentration is much higher than Cu (23:1 Zn:Cu). At the low current density end of the film (long, thin arrow in Figure 2-8), Cu ions have ample time to diffuse in from bulk solution and replace the ions being deposited. At the high current density end of the working electrode (short, thick arrow in Figure 2-8) the molarity difference between Cu and Zn becomes more significant. Cu is deposited at its limiting current density but Zn is not. Cu ions slowly diffuse in from the bulk solution while ample Zn ions are available for deposition. Zn is preferentially deposited simply because there isn't enough Cu around. Alloys deposited at the high-current density end of the film will be rich in Zn while alloys deposited at the low-current density end of the film will be rich in Cu, and the area between should show a smooth variation in composition.

The method is very similar to the pulse plating method used in section 4.4.1, and the results are the same, compositional variation along the length of the working electrode.

This approach has been explored before using a rotating cylindrical Hull cell (RCHC) [4.33]. Our results are unique because a RCHC was not used, the binary system studied is Cu-Zn (rather than Cu-Ni), and the structure and stoichiometry of an electrodeposited composition-spread library of binary alloys is compared to bulk electrodeposited samples prepared by bulk, one-at-a-time conventional methods.

Seven different bulk samples were prepared in the parallel electrode cell discussed in section 2.2.4 using on/off pulsed electrodeposition. Note that compositional variation is not expected since the electrodes are parallel. The same pulsed waveform was used to deposit individual bulk alloys, only the length of the off pulse was varied. A 100 mA pulse was applied for 6.09 s followed by an off pulse, ranging from 0 to 36 s. Two thousand cycles were performed corresponding to a theoretical thickness of 20 μm if only Zn is deposited. Obviously both Cu and Zn will be deposited, but it's a good approximation. 20 μm thick films are considered bulk compared to the 1-2 μm thick films deposited in the composition-spread library. During the on pulse both Cu and Zn are deposited. Cu ions near the working electrode are quickly consumed due to their low concentration. During the off pulse Cu ions from the bulk solution diffuse in to replace the Cu consumed during the on pulse. Cu ions eventually diffuse onto the surface of the working electrode and ion-exchange with deposited Zn. The longer the off pulse the more Cu ions will diffuse to the electrode, the more Cu will exchange with Zn and the higher the Cu content in the deposited film. By varying the length of the off pulse the Cu

content in bulk deposited films can be controlled. This is important because we wanted to compare thin-film alloys deposited in the composition-spread library, where Cu content varies as a function of position, with alloys prepared by one-at-a-time bulk deposition methods.

In this study the maximum amount of Cu depleted from the bath is approximately equal to a pure Cu film 10 μm thick. After depositing that much Cu there would still be 67.4% of the original concentration of Cu remaining in the bath. Therefore, Cu content should not significantly vary with thickness of the deposited film.

Figure 4-22 is a plot of Zn/Cu atomic % vs. position along the substrate prepared by combinatorial electrodeposition. The position is measured from the top (low current density end) of the film to the bottom (high current density end) of the film. The composition-spread is approximately linear for the first five centimeters, then the data become more scattered. The increased scatter is attributed to peeling of the film near the bottom, high current density end of the film. The limiting current density of both Cu and Zn ions may have been reached at the high-current density end, resulting in hydrogen evolution, which would also explain why, on average, the composition does not vary significantly.

Cu-Zn films can be made using both combinatorial electrodeposition methods and individual, one-at-a-time, bulk methods; the next step will be to compare the two.

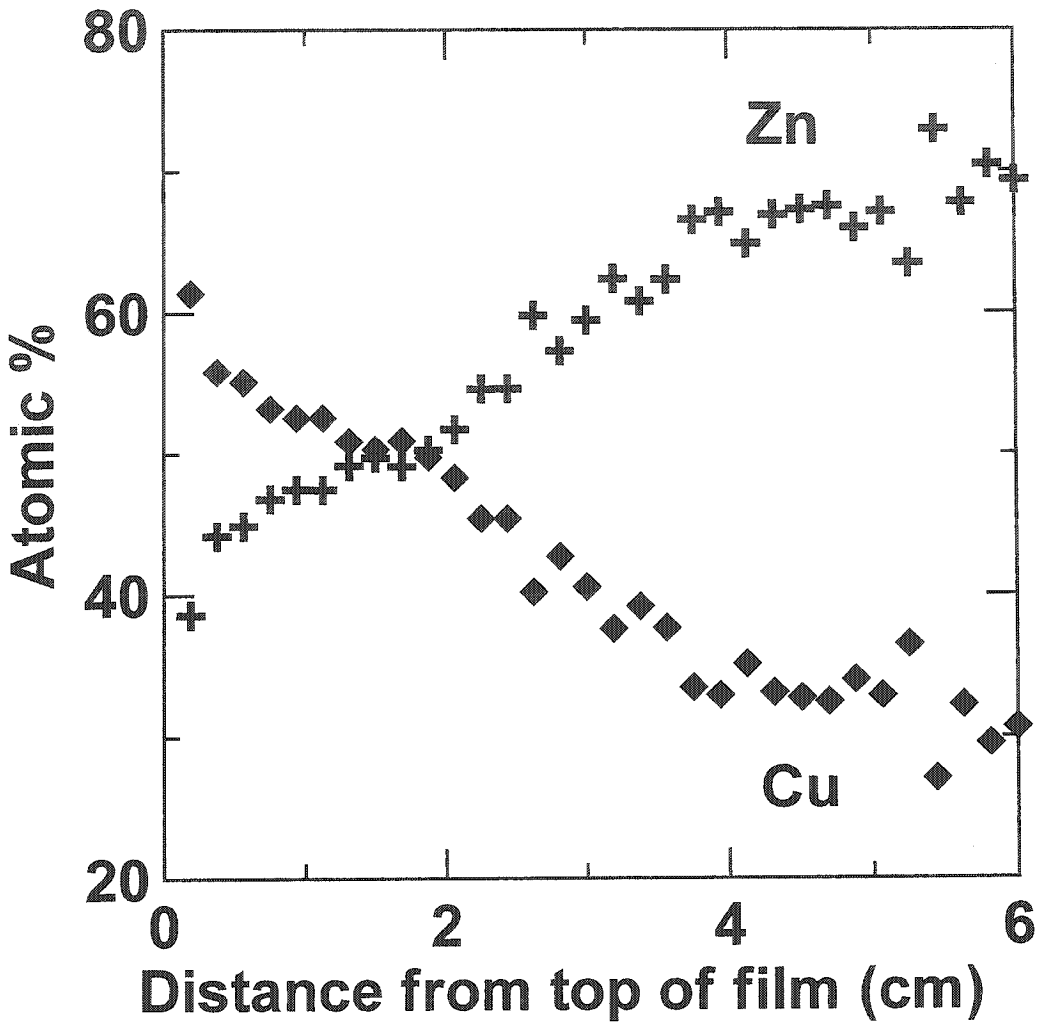

Figure 4-22 Atomic percent Cu or Zn vs. distance from top of film. The film was deposited galvanostatically in the Hull cell presented in Figure 2-8

A second composition-spread library of Cu-Zn alloys was deposited for gravimetric analysis. Peeling at the high current density end of the film was still an issue but extra care was taken to ensure the peeling flakes were not lost. Figure 4-23 shows gravimetric data for seven discs punched from the composition-spread electrodeposited film. 1.32 cm diameter (0.5″) discs were sequentially punched along the length of the film and then weighed. Punch position, from the top of the film, is plotted vs. mass of deposited film (total mass minus nickel substrate mass). The average thickness is given

on the right ordinate represented by open circles. Thickness was calculated using an average Cu-Zn alloy density of 8.1 g/cm^3. Thickness variation is almost linear.

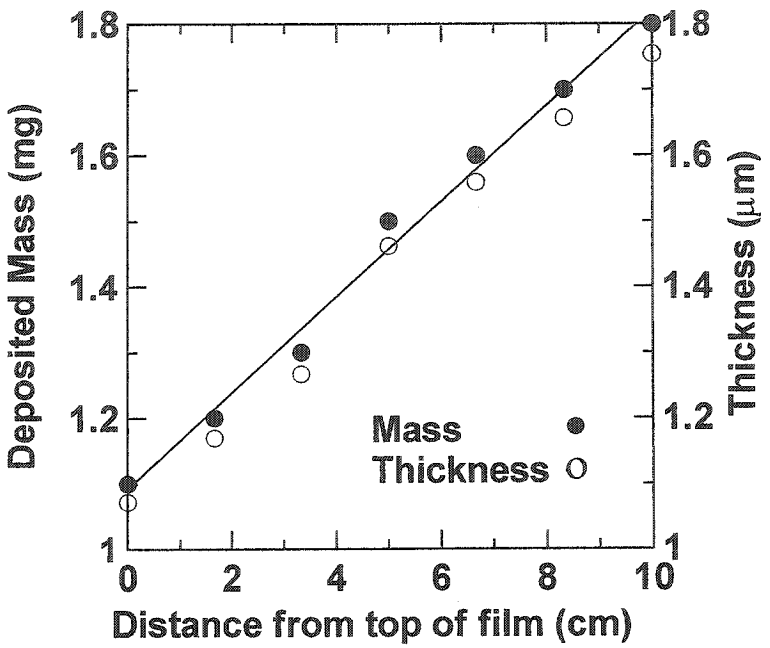

Figure 4-23 Deposited mass and thickness vs. distance from top of film. A second composition-spread Cu-Zn film was deposited in the Hull cell and punches were then cut from the film and weighed

Figure 4-24 consists of three panels with different scattering angle ranges and 12 XRD scans per panel. Each scan was taken sequentially along the length of the composition-spread electrodeposited library of Cu-Zn alloys. Three ranges were selected for detailed analysis corresponding to peak positions of known Cu-Zn alloys. To the right of the figure are two columns indicating scan number and the approximate Zn content in atomic percent. The approximate Zn content can be inferred from Figure 4-22 by measuring where each XRD scan was taken relative to the top of the film.

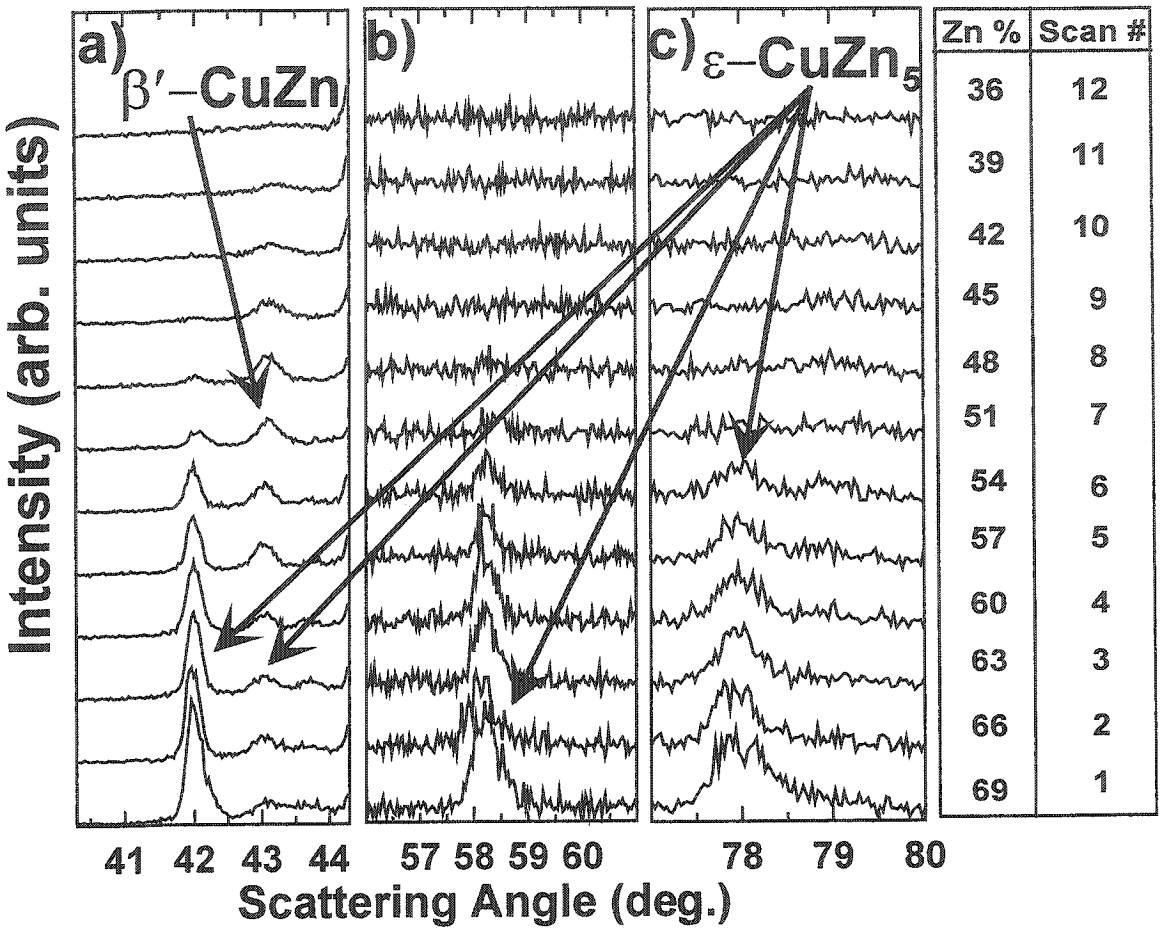

Figure 4-24 Twelve XRD scans taken sequentially along the composition-spread Cu-Zn film deposited in the Hull cell. Three scattering ranges are selected for focused study

Figure 4-25 is the Cu-Zn phase diagram [4.25]. A double-headed arrow indicates the area of phase space sampled by the composition-spread electrodeposited film. Short bars indicate the discrete regions of phase space sampled by the seven electrodeposited bulk alloys. Note that all films were deposited at room temperature. The vertical placement of the bars and double-headed arrow does not represent fabrication temperature. The vertical placement is for illustrative purposes only.

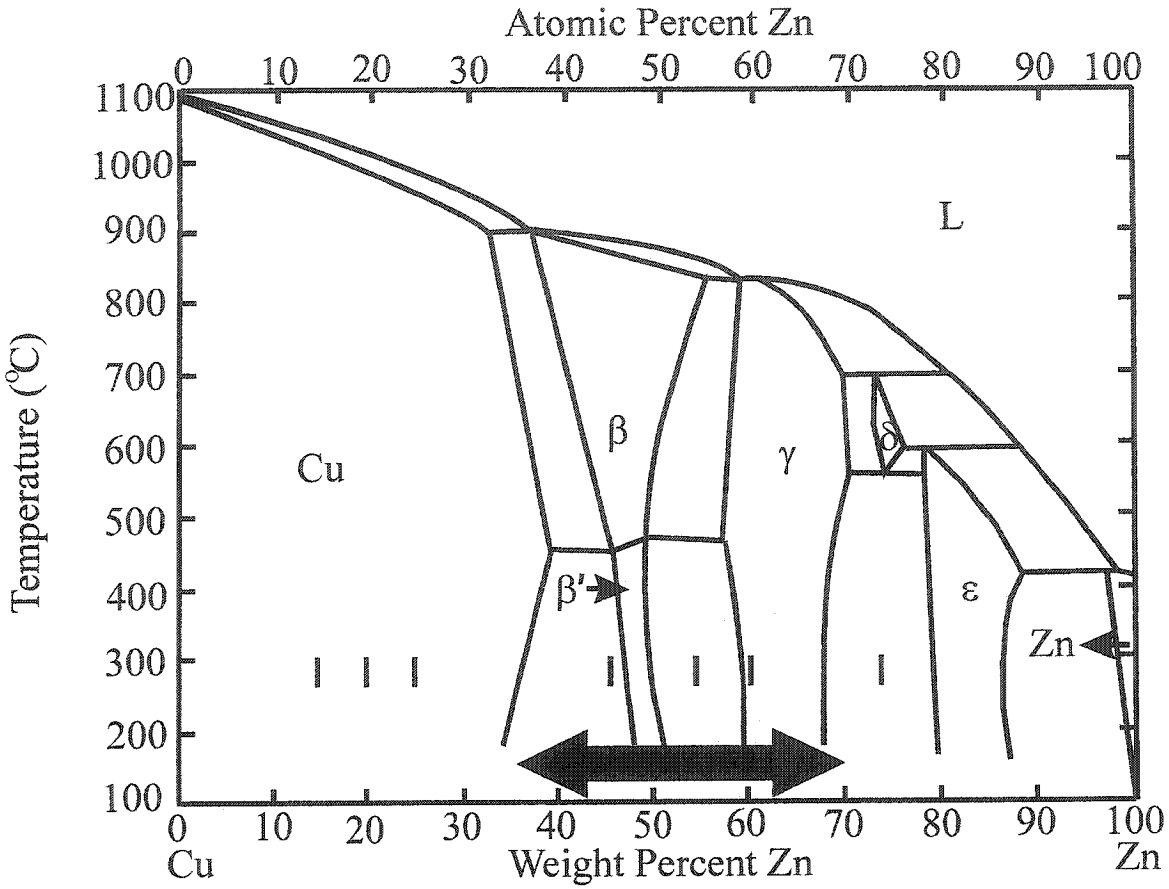

Figure 4-25 The Cu-Zn phase diagram. The double headed arrow represents the range of compositions sampled by the film deposited in the Hull cell. Short bars indicate the discrete regions of phase space sampled by bulk films prepared by one-at-a-time methods. Note that all films were deposited at room temperature. The vertical placement of the double-headed arrow and bars is for illustrative purposes only

Figure 4-26 shows powder XRD patterns for the seven different Cu-Zn alloys prepared by one-at-a-time pulsed electrodeposition methods. The column on the left indicates the off-pulse duration and the column on the right indicates atomic percent Zn. Since a thick film was deposited most of it could be scraped off the nickel substrate. The recovered material was ground in an agate pestle and mortar. Typically, a few milligrams of powdered material could be obtained from each sample, more than enough for powder XRD and electron microprobe analysis. Powder XRD patterns of an electrodeposited

film are superior to patterns obtained when the film is attached to the substrate because the film could be highly oriented. The pattern at the bottom of Figure 4-26 agrees well with the ε-$CuZn_5$ phase. As the off pulse is increased, Cu content also increases because Cu has more time to exchange with Zn, this corresponds to moving up Figure 4-26. The ε-$CuZn_5$ phase recedes and is replaced by the Cu-rich β′-CuZn phase. Further up the film (becoming more Cu-rich) the β′-CuZn phase also recedes, replaced by a Cu phase with a solid solution of Zn.

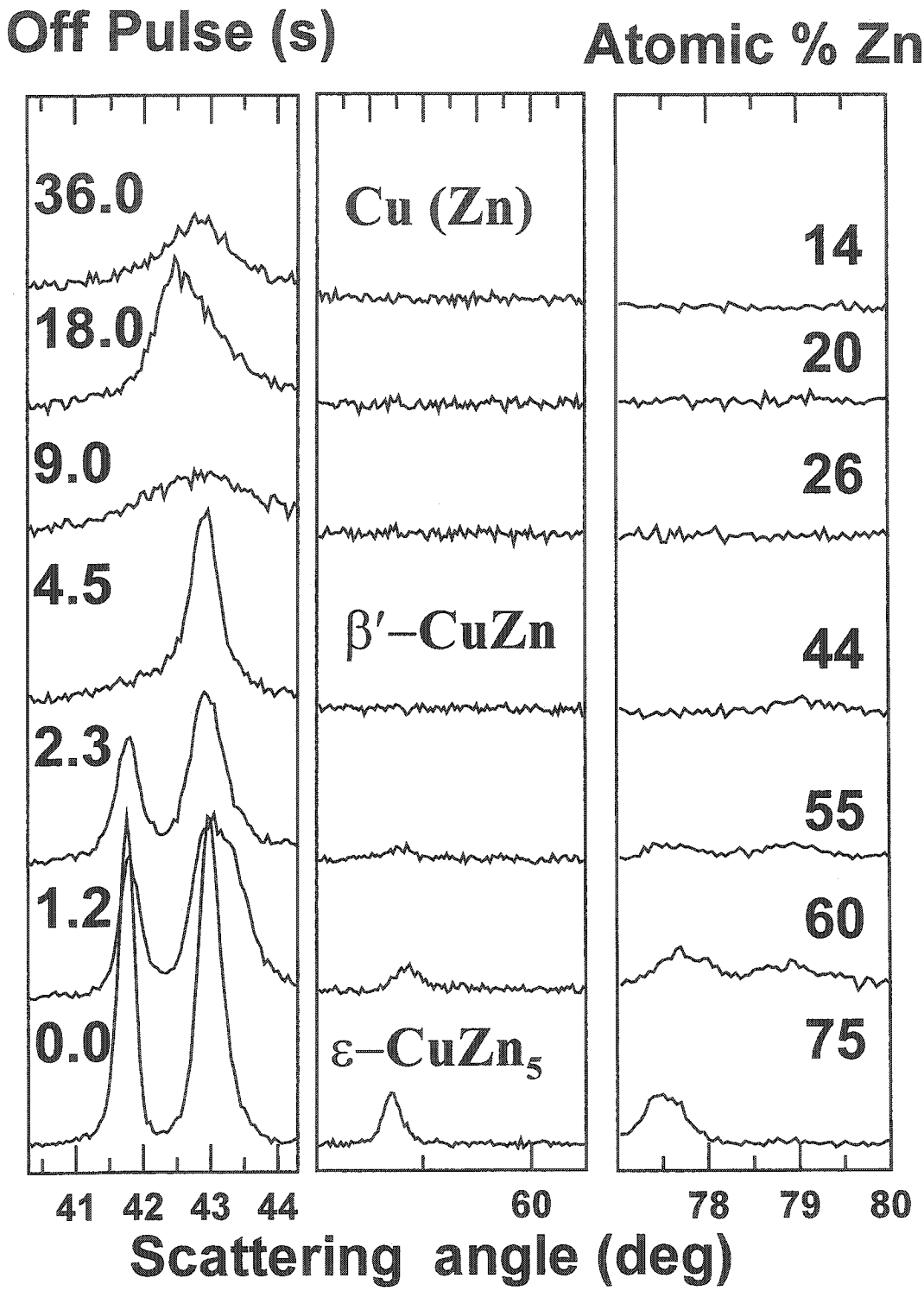

Figure 4-26 XRD patterns of seven individual Cu-Zn bulk films prepared by conventional one-at-a-time methods. The rightmost column represents the Zn composition in the film determined by EDS. The column on the left represents the length of the off pulse used in the pulsed deposition waveform

The effect of Cu content on crystallographic structure of the deposited alloy was explored in two different ways. 1) Compare the crystal structure of electrodeposited films obtained from two different baths with significantly different Cu molarities. Figure 4-27a shows XRD patterns for two films deposited the same way from two different baths where the only difference is in the Cu molarity, 0.056 M vs. 0.013 M Cu sulfate. 2) Compare the crystal structure of electrodeposited films obtained from the same type of bath but deposited at different current densities. XRD patterns for two films obtained from the same type of bath and deposited at different current densities (3.6 mA/cm^2 vs. 0.7 mA/cm^2) are presented in Figure 4-27b.

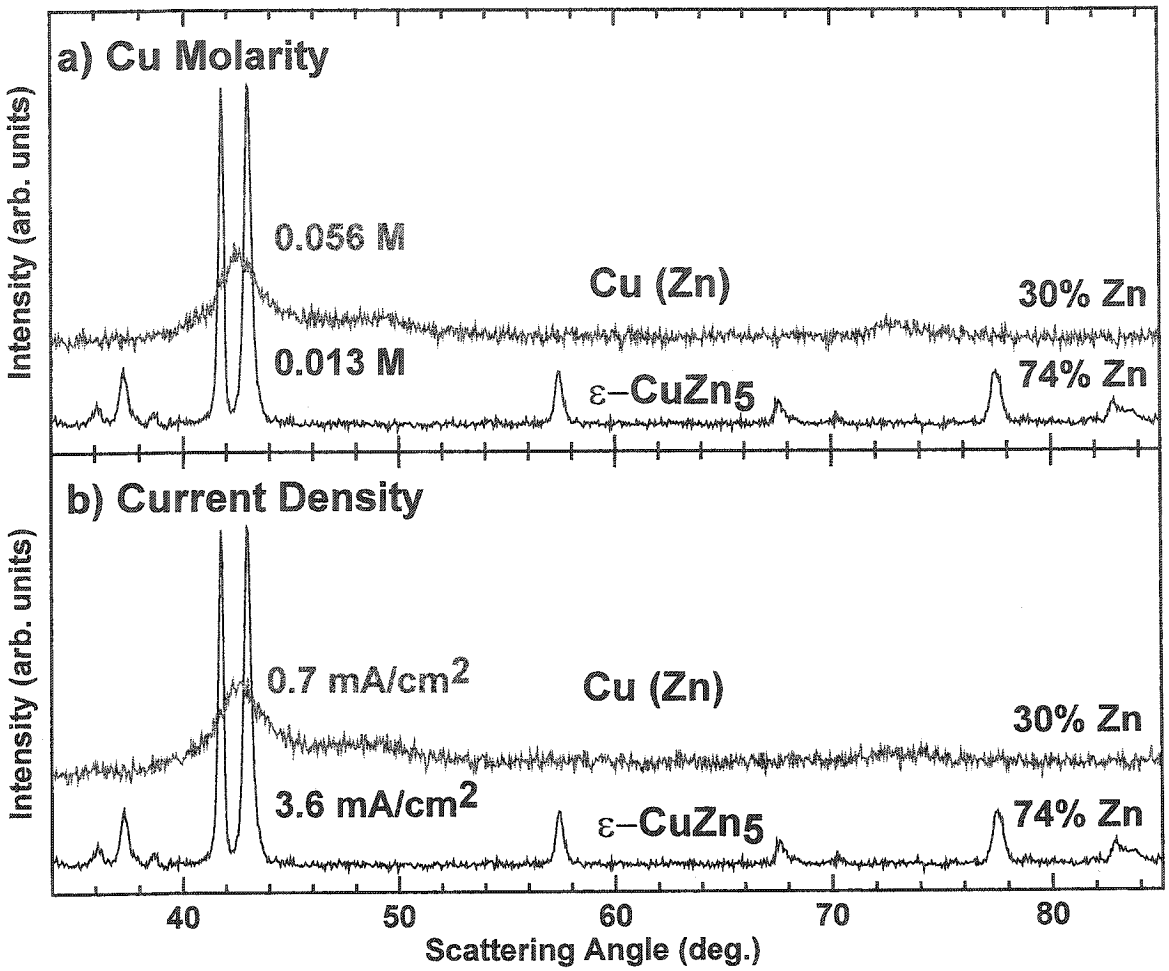

Figure 4-27 XRD patterns of Cu-Zn films. Panel a) represents two films deposited from two separate baths where the only difference is the Cu concentration. Panel b) represents two films deposited from the same type of bath but at different current densities

4.5.2 Discussion

Figure 4-22 shows that a composition-spread library of Cu-Zn alloys was successfully electrodeposited from a single bath in a single run where composition varies as a function of position. This method of creating a library of binary alloys is powerful for many reasons: 1) Deposition occurred at standard conditions with simple equipment. The most complicated and costly item in the setup is a programmable current source. However, that could be replaced by a "D" cell. If the current source was replaced by a D

cell the total cost of the experiment would be in the order of a few dollars. 2) The composition-spread alloy library was deposited in less than an hour, and the entire experiment took less than an hour and a half, including preparation time. In that time over one third of the Cu-Zn phase diagram was sampled. 3) By changing any number of variables (e.g.: current density, Zn:Cu molarity, Hull cell dimensions, temperature, pH, agitation) one can change the region of phase space sampled by the film. 4) All components are inexpensive and readily available. 5) The method can be extended to many other binary systems. 6) The method is simple, and 7) It will be shown that the method is scalable. That is, a material deposited in the composition-spread library could be easily made by bulk deposition methods, which are fast and inexpensive.

Figure 4-22 shows that composition smoothly varies as a function of position in the composition-spread electrodeposited library of alloys. Figure 4-24 shows that the crystal structure also smoothly varies as a function of position. The bottom scan in Figure 4-24a suggests a multi-phased structure, since there is a strong peak at 42.0° and a "smear" of peaks between 42.5° and 44.0°. By the third scan up from the bottom in Figure 4-24a two peaks near 43.0° and 43.8° are readily identified. Peaks due to the ε-$CuZn_5$ phase are expected at 42.2°, 43.4°, 57.6° and 77.8° (Figure 4-24a, b, c lower scans). Although the peaks in Figure 4-24 do not line up with the exact theoretical values, they are very close. Furthermore, these peaks account for four of five peaks observed in Figure 4-24, scan #3. The alloy in scan #3 (from the bottom) is approximately 63% Zn. From the phase diagram in Figure 4-25 this corresponds to the γ-Cu_5Zn_8 region. Unfortunately, γ-Cu_5Zn_8 has only one strong peak, at 43.3°, making it difficult to isolate given the two strong peaks of ε-$CuZn_5$ at 42.2° and 43.4°.

Electrodeposited alloys do not necessarily follow the phase diagram. Electrodeposition is a non-equilibrium process. This has been observed before in [4.34] and discussed in section 4.4.2. In scan #1 (Figure 4-24), the presence of γ-Cu_5Zn_8 is possible but dubious. Subsequent scans show the intensity of the ε-$CuZn_5$ peaks diminishing as we move up the film (up Figure 4-24), in scan #6 (from the bottom) the peaks near 57.6° and 77.8° are essentially gone and the peaks at 42.0° and 43.6° are significantly reduced, suggesting the ε-$CuZn_5$ phase is receding.

Scan #9 (from the bottom) shows that ε-$CuZn_5$ is almost completely gone, replaced with a new phase with a single peak near 43.0°, this is no doubt the β'-CuZn phase. Presence of the β'-CuZn phase near the bottom of the film accounts for the fifth peak, near 43.0°, that cannot be attributed to ε-$CuZn_5$. Scan #9 has a Zn content of approximately 45%. According to the phase diagram β'-CuZn should be the only phase present, as observed. The Zn content is further reduced toward the low-current density end of the film (up Figure 4-24), and the β'-CuZn phase seems to disappear almost entirely by scan #12. Figure 4-24 shows how the structure smoothly varies along the length of the film. It is reasonable to conclude that the structural variation is a consequence of the change in composition, especially since there is some agreement with the phase diagram. However, since the current density varies along the length of the film, so does the thickness, we need to determine whether the structural and compositional variation is a function of thickness and not just composition.

Although the presence of γ-Cu_5Zn_8 has not been ruled out completely, we do not believe it is present in the electrodeposited film. We believe that the β'-CuZn and ε-$CuZn_5$ phases sufficiently describe both the XRD and EDS data.

Figure 4-26 shows that the structure of bulk films prepared by one-at-a-time methods is highly dependent on the duration of the off-pulse, supporting the concept of aqueous Cu exchanging with deposited Zn. The bottom scan matches well to the ε-$CuZn_5$ phase, as does the Zn content relative to the phase diagram. The middle scan with 44% Zn matches well to β′-CuZn, which is expected from the phase diagram. With 44 atomic % Zn the phase diagram suggests co-existence of two phases β′-CuZn and a solid solution of Zn in Cu. The top scan represents nano-structured Cu. In this region the phase diagram indicates a solid solution of Zn in Cu. A smooth variation is observed, starting with ε-$CuZn_5$ travelling through the β′-CuZn phase and ending with nano-structured Cu. Note that once again the presence of γ-Cu_5Zn_8 cannot be confirmed, nor explicitly denied. Apparently, the formation of the electroplated γ-Cu_5Zn_8 phase is not favorable.

Figure 4-24 and Figure 4-26 show that structure has a strong dependence on Cu content in the film, which is expected given the number of different phases in the Cu-Zn phase diagram. Figure 4-27 further supports the importance of Cu content on the structure. By lowering the current density, Cu ions have more time to diffuse to the electrode and deposit. Figure 4-27b shows that the film deposited at 3.6 mA/cm^2 has a much higher Zn content (74 %) than the one deposited at a lower current density (0.7 mA/cm^2, 30 % Zn). It's interesting to note that the 74 % Zn film is much more crystalline than the 30% Zn film. According to the phase diagram the 30 % Zn film is a solid solution of Zn in a Cu matrix. Long-range ordering may be inhibited by the solid solution, hence the XRD pattern in Figure 4-27. Figure 4-27a shows that the film obtained from the high Cu molarity (0.056 M) bath has a much higher

Cu content (74 %) compared to the film obtained from the lower Cu molarity (0.013 M, 30 % Zn) bath. The higher the Cu concentration the more quickly Cu will diffuse to the working electrode, and more Cu will deposit. Figure 4-27 shows that bulk, nano-structured Cu-Zn alloys can be deposited by two different conventional electrodeposition methods (galvanostatic and pulsed). It would be easy to scale the process and deposit kg, rather than mg, of material. Unfortunately, the importance of scalability is often overlooked.

A composition-spread library of Cu-Zn alloys has been deposited from a single bath in a single run where composition and structure varies smoothly as a function of position. The film was prepared simply, inexpensively and quickly. The composition-spread library follows the Cu-Zn phase diagram except the γ-Cu_5Zn_8 phase is not observed. The crystal structure and composition of alloys deposited in the composition-spread library is representative of bulk alloys prepared by one-at-a-time methods. This means that a material discovered using the combinatorial electrodeposition method discussed here, could be used to find and optimize a material that could then be fabricated using conventional, one-at-a-time bulk deposition methods. Compared to competing technologies the road from discovery to mass production would be relatively easy. Therefore, it has been shown that a combinatorial method via electrodeposition embodies, and even extends, the advantages of combinatorial material science: faster, better, cheaper, simpler and scalable.

4.6 Ternary combinatorial electrodeposition

To the author's knowledge, this is the first time ternary combinatorial electrodeposition has been reported in writing. The accolades of combinatorial methods has been discussed previously, the cost advantages in using electrodeposition to fabricate composition-spread films of binary alloys has also been discussed. The next logical step was to invent a method by which a composition-spread library of ternary alloys could be fabricated. In particular, the library should be fabricated in such a way that the variation of two elements are anti-parallel to one another, so that a large range of different compositions can be sampled, such as in the Cu-Sn and Cu-Zn examples. The composition variation of the third element should be orthogonal to the first two, thereby sampling the largest region of ternary phase space possible. The method developed to fulfill these requirements will be discussed in the following sections.

Before ternary alloys could be deposited a composition-spread library of binary alloys had to be deposited first. As discussed in section 4.4-5, it is very easy to electrodeposit composition-spread libraries of binary alloys. In sections 4,4-5 the Cu-Sn and Cu-Zn systems were discussed. Given our success with the Cu-Sn and Cu-Zn binary systems, we chose to work on the Cu-Sn-Zn ternary system. For reasons to be discussed later, a composition-spread library of Sn-Zn alloys had to be deposited first. Deposition of a composition-spread library of Sn-Zn alloys will be discussed next.

4.6.1 Sn-Zn

A different binary system was investigated, Sn-Zn. A composition-spread Sn-Zn film was deposited in the same way that the composition-spread Cu-Zn film was

prepared. A potassium pyrophosphate solution with poor throwing power was used where the concentration of Zn was much higher than Sn (Table 2-1, Sn-Zn). A 100 mA current was applied to the Hull cell (refer to section 2.2.4) for 6.28 hrs. Note that a Hull cell 4 cm wider (11.5 cm vs 7.5 cm) than the one discussed in section 2.2.4 was used. As with the Cu-Zn system the composition of the deposited film varied with current density, which varied as a function of position along the working electrode in the Hull cell. The compositional variation of Sn with position was anti-parallel to Zn, as desired.

Figure 4-28 shows compositional data for two electrodeposited Sn-Zn films prepared as discussed above. Composition varies as a function of distance from the top of the film in a Hull cell where the top of the film is defined by Figure 2-8. Ni was used as the substrate. Atomic % Ni is also plotted vs. distance in Figure 4-28b. Note that in a Figure 4-28b large variation (almost 80% of composition space) is achieved using a very simple method.

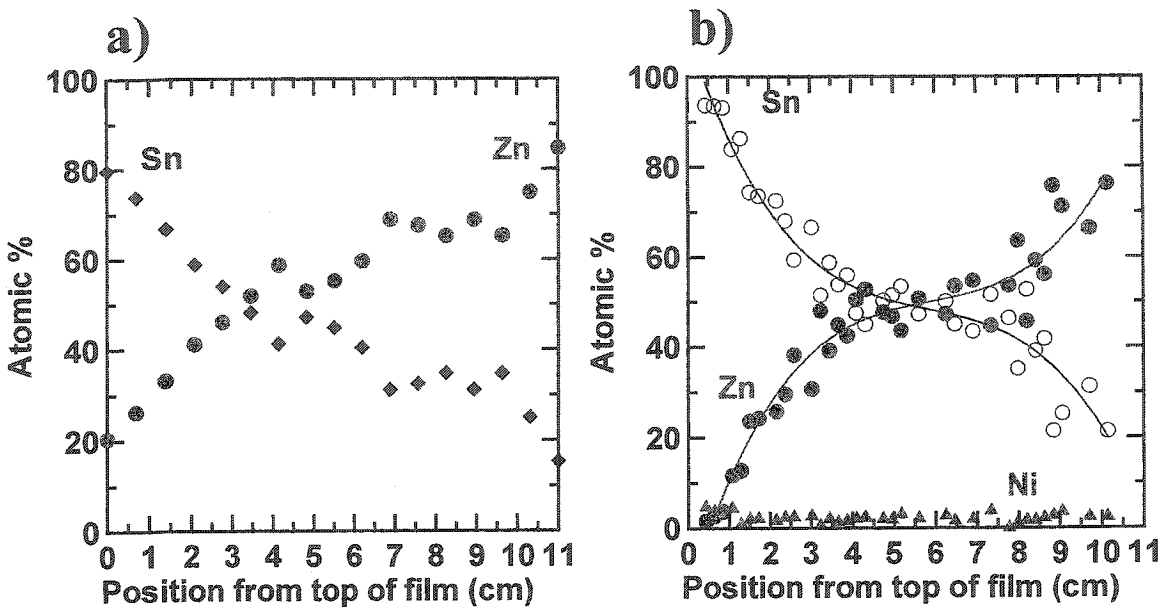

Figure 4-28 Compositional variation of Sn, Zn and Ni as a function of position from the top of the film

Figure 4-29 shows that structure also varies as a function of position. The XRD patterns on the right approximately line up with the area from which they were obtained on the film on left. Note that the image of the film on the left shows a variation in color from top to bottom, suggesting compositional variation.

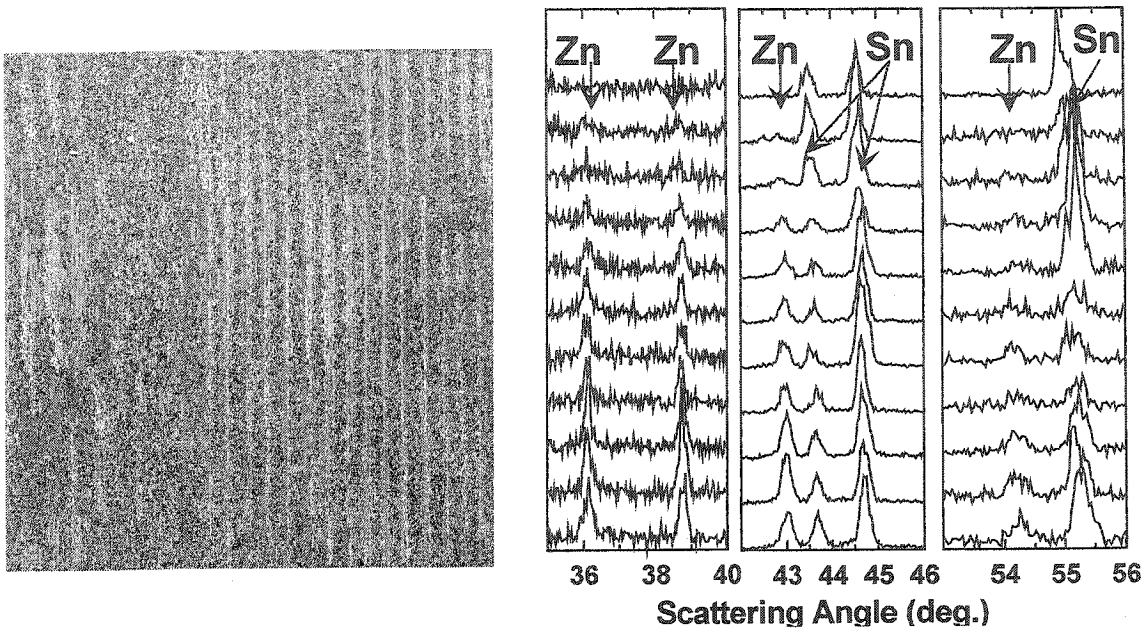

Figure 4-29 Structural variation of a composition-spread Sn-Zn film as a function of position. The XRD patterns on the right approximately line up with the area from which they were obtained on the film on the left

The XRD patterns are easily understood. Sn and Zn do not form binary alloys, as expected from the simple, eutectic phase diagram in Figure 4-30 [4.25]. The x-ray diffraction pattern of Zn recedes as we go from the bottom (Zn-rich) to the top (Sn-rich) of the film, as expected from Figure 4-28. The Sn phase, however, is prevalent throughout. This may be related to the high atomic number of Sn making it better at diffracting x-rays compared to Zn. Although not obvious in the XRD diagrams of Figure 4-29, the variation in Sn content as a function of position is evident from Figure 4-28. A film has been deposited where the composition of two elements varies anti-parallel to one another as a function of position. The next challenge is to introduce a third element, whose composition varies orthogonal to the other two (Sn and Zn).

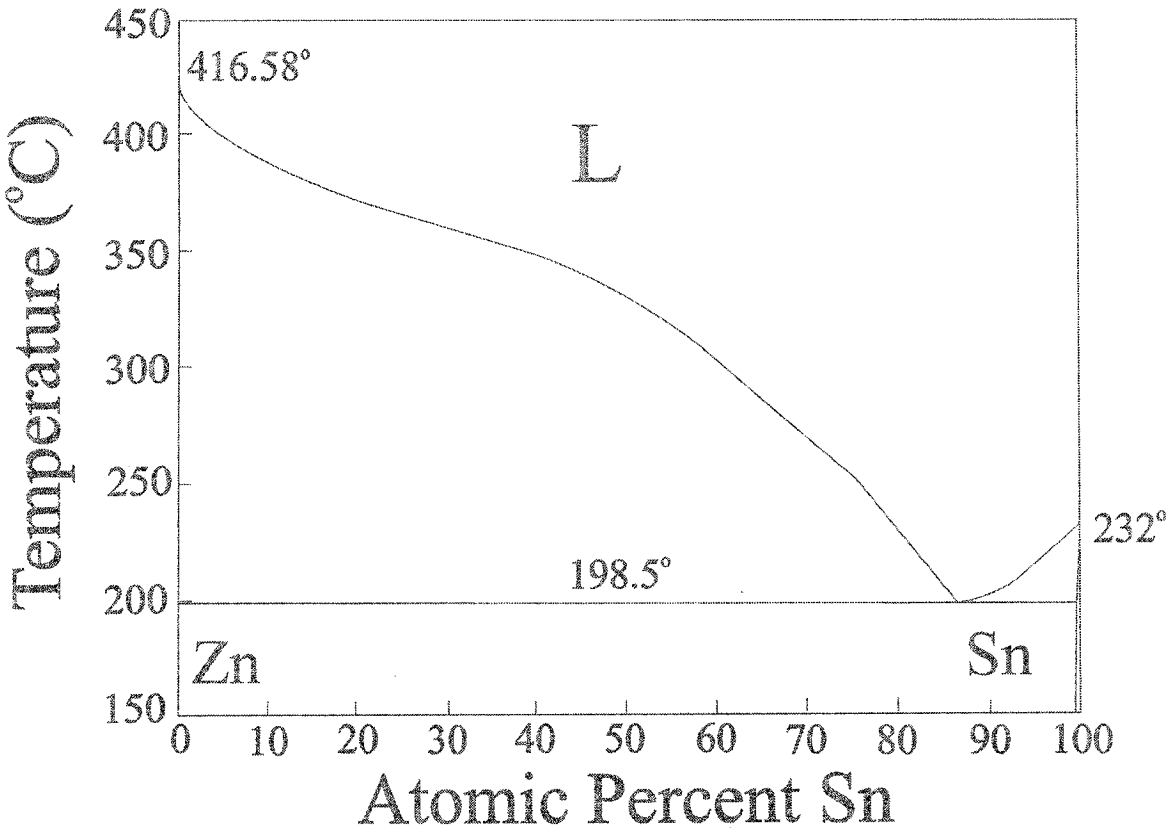

Figure 4-30 The Sn-Zn phase diagram

4.6.2 Dripped immersion plating

The choice of a Sn-Zn system was not arbitrary. A binary, composition-spread film was needed that would accept a third element whose composition varies orthogonal to the compositional variation of the first two. Furthermore, we wanted to use a simple, inexpensive approach. This was accomplished using immersion plating. Both Sn and Zn will ion-exchange with aqueous Cu ions, as indicated by their relative SHE reduction potentials in Appendix 2. The original Sn-Zn film is rotated 90° counter clockwise (as viewed from Figure 4-29) and placed in an empty container. A weak Cu sulfate solution (3 mM $CuSO_4 \bullet 5H_2O$) is slowly dripped into the empty bath. To achieve a slow, constant drip of Cu sulfate solution over time a peristaltic pump was required. Unfortunately, one

was not immediately available. Unwilling to wait and pay for a new peristaltic pump, a Tsunami Blaster X water gun was purchased. The Tsunami Blaster X is manufactured and distributed by Six Flags Theme Parks International. It is readily available in local stores such as Walmart and Canadian Tire. The water gun was easily modified to act as a variable peristaltic pump. A picture of the modified super soaker is shown in Figure 4-31. The water flow is easily adjusted by controlling the driving voltage or tubing size. The Tsunami Blaster X is designed to run off of four AA batteries (6 V) and requires a current of approximately 1 A. For simplicity, the modified pump was powered by a nearby PC. The PC power supply provides 5 V and 1 A of consistent power.

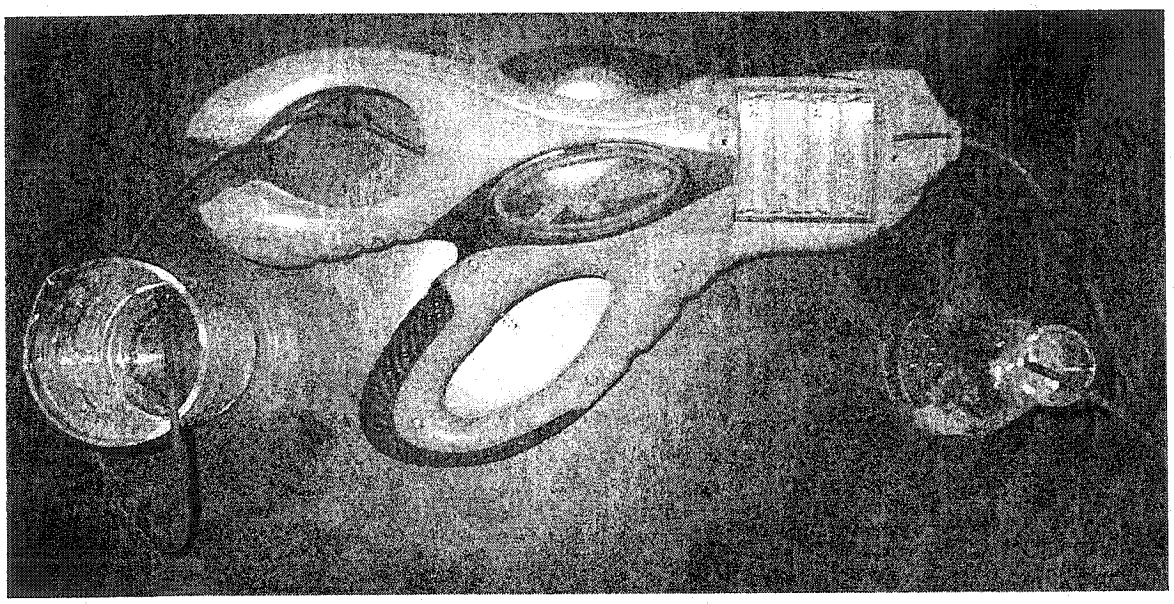

Figure 4-31 Modified Tsunami Blaster X water gun used as an inexpensive and convenient peristaltic pump

The solution is dripped into the container until the film is almost completely immersed. Approximately 1 cm of the film is left untouched by solution. The dripping process takes about twelve hours. The film is then removed from solution and rinsed in

distilled water. Since aqueous Cu ions will exchange with both electrodeposited Sn and Zn, the bottom of the film (remember it's been rotated 90° compared to the left-hand side of Figure 4-29) will be exposed to solution the longest, and therefore contain the most Cu (and the least Sn/Zn). Similarly, the top part of the film will experience the least amount of exchange. In fact, the very top will experience none at all. This way, a compositional variation of Cu is established orthogonal to the variation of Sn and Zn, as desired. For clarification, Figure 4-32 shows a schematic of the immersion plating timeline.

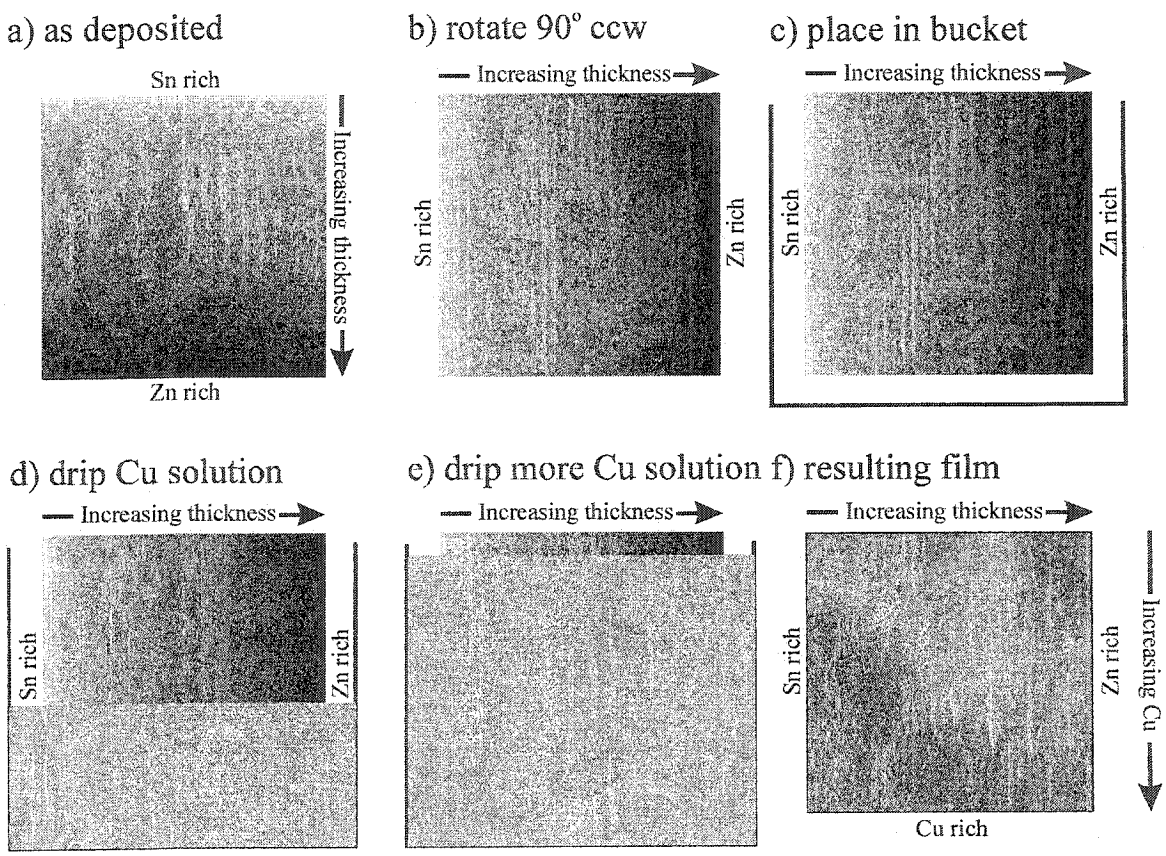

Figure 4-32 Schematic of the immersion plating timeline

4.6.3 Compositional variation

EDS measurements were performed on the film and the results for all three elements (Cu, Sn, Zn) are presented in the form of contour plots in Figure 4-33. The orientation of the contour plots is the same as the orientation of the film in Figure 4-32f. Overall, the structure of the contour plots is expected. Remember that the Zn-rich end of the film will be thicker than the Sn-rich end, because the current density was highest there. Similarly, it is expected that the exchange of Cu occurs uniformly from left to right (thin to thick) and increases from bottom to top. However, the compositional variation of Cu from left to right will not be linear. The film is thicker at the Zn-rich end compared to the Sn-rich end. Since an equal amount of Cu is expected to exchange from left to right, the change in atomic fraction Cu will be largest at the thin, Sn-rich end. Therefore, the highest Cu content is expected at the bottom, Sn-rich end of the film. Similarly, the Sn content will be low, because Sn has been exchanged for Cu. Since the dripped solution did not reach the top of the film, little to no Cu is expected. The top-left hand corner should therefore show the largest atomic fraction Sn. The top-right hand corner of the film will show the highest concentration of Zn and the bottom right-hand corner will show less Zn than the top right because some of the Zn has been exchanged for Cu. All of these predictions are confirmed by the contour plots in Figure 4-33.

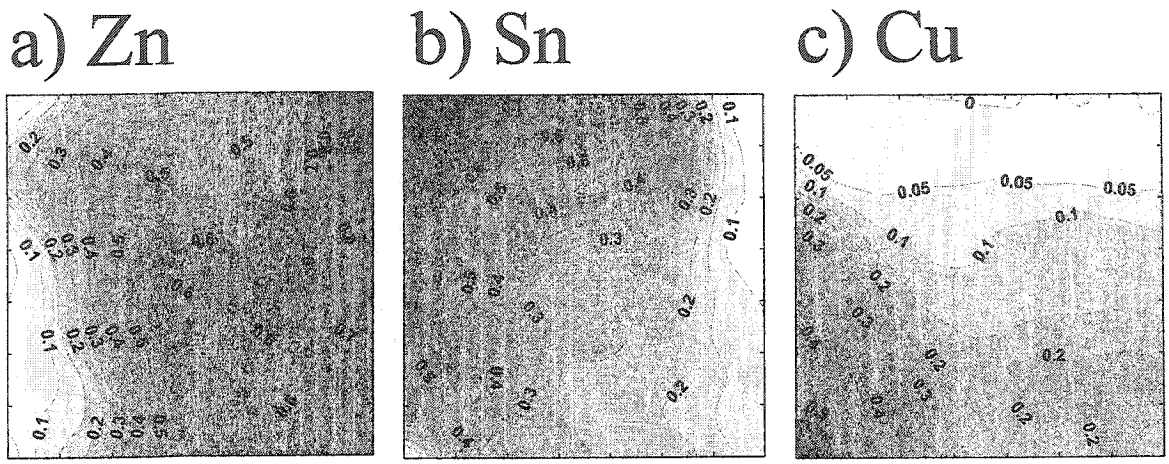

Figure 4-33 Contour plots showing compositional variation for all three elements, Cu, Sn and Zn

At this point it will be useful to consider a phenomenological model to further understand the contour plots presented above.

4.6.4 Phenomenological model

To model immersion plating of the electrodeposited Sn/Zn film, discussed in section 4.6.1, some of its characteristics should be examined. To ensure reproducibility, numerous Sn/Zn films like the ones discussed in Figure 4-28 and Figure 4-29 have been deposited and characterized. The variation in thickness and composition as a function of position is negligible between films. There is a thickness gradient from left to right, as shown in Figure 4-32f. To determine the variation of thickness with position, small coupons are punched from the film (thick to thin) and weighed. Each coupon has a well-defined area and the thickness of the underlying Ni substrate is known. The coupons are weighed and the mass of the substrate subtracted, then, given the area of the punch and making an educated guess about the density of the deposited material, the thickness can

be determined. The educated density guess is simply the average density of the two species, 7.31 g/cm^3 for Sn and 7.13 g/cm^3 for Zn. The analysis yields a thickness variation between ~1-4 μm.

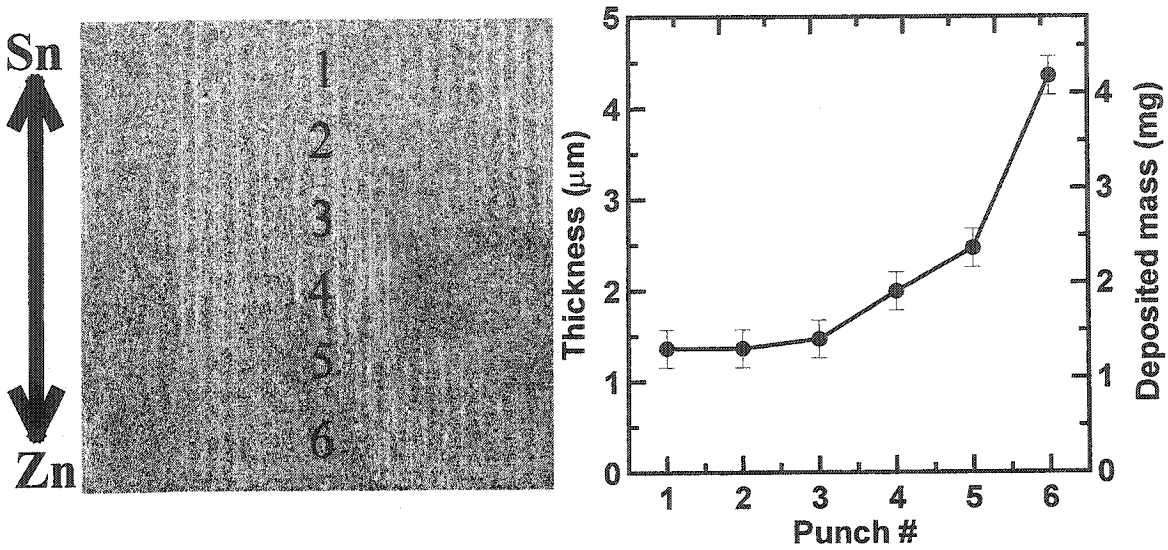

Figure 4-34 Thickness of deposited film vs. punch number

A second set of punches was taken vertically as viewed from Figure 4-32b. The punches weighed approximately the same indicating that thickness variation top to bottom is negligible (~5%). The stoichiometric variation of Sn and Zn as a function of position is known from EDS data, both before (similar to Figure 4-28a) and after immersion plating (Figure 4-33). The film used in the immersion plating experiment had a Sn/Zn composition gradient between 20 and 80 atomic % (80% Sn, 20% Zn at the thin end and 20% Sn 80% Zn at the thick end). The atomic composition gradient was approximately linear, as in Figure 4-28a. During the immersion process Sn and Zn exchange with aqueous Cu ions. Unfortunately, the dissolution rate of Sn and Zn with Cu is unknown. However, it is expected that the amount of Cu exchanged from top to

bottom (given the film shown schematically in Figure 4-32f) should be approximately linear, since the Cu solution was dripped at a constant rate. The information above allowed a simple model of the immersion process to be built using Microsoft Excel.

A square theoretical film was constructed whose thickness varies from left to right. The thickness of the experimental film discussed above varied between ~1 and 4 μm. Correspondingly, the theoretical model varies from 100 to 400 units. A schematic of the theoretical film is given in Figure 4-35. Figure 4-35 shows a schematic of both the x-y and x-z planes. The color gradient from white to black corresponds to the compositional gradient. White corresponds to Sn-rich and black to Zn-rich. The theoretical film is modeled after the film shown in Figure 4-32b.

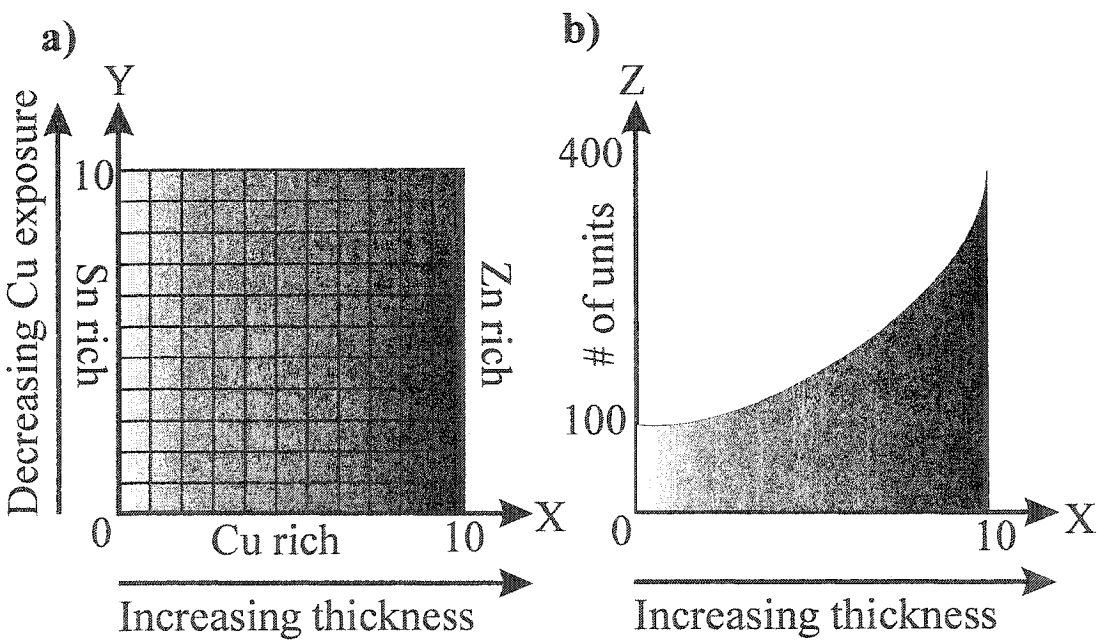

Figure 4-35 Schematic of the theoretical film in both the x-y and x-z planes

Before immersion in the Cu-containing bath thickness and composition do not vary in the y direction (Figure 4-35a), but they do vary in the x direction. The variation in atomic percent Sn/Zn is between 20 and 80%. To model the variation in thickness and atomic fraction the number of Sn units is kept constant at 80, and the Zn content increases with x. Since the change in atomic percent Sn/Zn is approximately linear from left to right, and the Sn content remains fixed at 80 units, Zn units must be added non-linearly. This is reflected schematically by the x-z graph in Figure 4-35b. Note that Figure 4-35b is very similar to the thickness plot in Figure 4-34. Starting from 0 and moving in the positive x-direction there will be 11 steps. The number of Zn units added per step (Zn_{added}) is modeled by equation 4.6.4-1:

$$Zn_{added} = \frac{80}{0.8 - 0.06 \cdot n_x} - 80 \qquad (4.6.4\text{-}1)$$

where n_x is the number of steps in the x direction. The theoretical film uses 11 steps in both the x and y directions. The # of Zn units starts at 20 at x = 0, and is a maximum (320) at x = 10. At x = 0 there are 80 Sn units and 20 Zn units, corresponding to 80 atomic % Sn, as desired. At the thick end there are still 80 Sn units, and 320 Zn units, corresponding to 80% Zn, as desired. Hence, both thickness and compositional variation are established with variations similar to the film discussed in section 4.6.1. The next task is to model the immersion plating of Cu.

Using a simple model we hoped to reproduce the contour plots in Figure 4-33. Two models were constructed. Both are based on the theoretical film shown in Figure 4-35. To successfully reproduce the results in Figure 4-33 some assumptions were made about the immersion process. The exchange rates of Sn and Zn with Cu are unknown. The models assume that they are equal. As discussed above, the number of Cu units

exchanged from left to right should not vary. In our first model this assumption was made. The bottom left-hand corner of Figure 4-33c shows approximately 60 atomic % Cu. To model 60 atomic % Cu using the construct of the theoretical film shown in Figure 4-35, 60 units of Cu would be exchanged. Before Cu is exchanged, the bottom left-hand corner of Figure 4-35a has 100 units; 20 Sn and 80 Zn. Sixty units of Cu are exchanged and the exchange rate of Cu with Sn and Zn is equal, therefore $20 \cdot \frac{60}{100} = 12$ units of Zn are exchanged and $80 \cdot \frac{60}{100} = 48$ units of Sn are exchanged. After exchange of Cu there are 60 units of Cu, 8 units of Zn and 32 units of Sn, or, 60 atomic % Sn, 8 atomic % Zn and 32 atomic % Sn. From the contour plots in Figure 4-33 these numbers make sense.

Since the Cu solution was dripped at a constant rate it is assumed that the exchange of Cu will vary linearly with y (as described in Figure 4-35). Dripping stopped just before the solution reached the top of the film, so no exchange of Cu is expected at y=10. This is easily modeled using equation 4.6.4-2:

$$Cu_{exchanged} = 60 - 6 \cdot n_y \qquad (4.6.4\text{-}2)$$

Where $Cu_{exchanged}$ is the number of Cu units exchanged and n_y is the number of steps in the y direction, starting at 0. In the x direction the number of Cu units exchanged is constant. At y = 10 no Cu is exchanged, as desired.

Units of Zn and Sn are being exchanged for Cu. It was assumed that the exchange rate of Cu with Sn is the same as the exchange rate of Cu with Zn. Therefore, an equal proportion of each species will be exchanged. This is easily modeled using

equation 4.6.4-3. Since the exchange rates of Sn and Zn are equal, only Sn is indicated. The equation is the same for Zn:

$$Sn_{exchanged} = Sn_{units} \cdot \frac{Cu_{exchanged}}{Sn_{units} + Zn_{units}} \qquad (4.6.4\text{-}3)$$

where $Sn_{exchanged}$ is the number of Sn units exchanged, $Cu_{exchanged}$ is the number of Cu units exchanged (determined by equation 4.6.4-2), Sn_{units} is the number of Sn units before the exchange, and Zn_{units} is the number of Zn units before exchange. It is easy to keep track of the number of Cu, Zn and Sn units left after immersion using Microsoft Excel, the model of the theoretical film, and equations 4.6.4-2 and 4.6.4-3. Contour plots are generated using data from the spreadsheet. Figure 4-36 shows contour plots generated using the results from the first model:

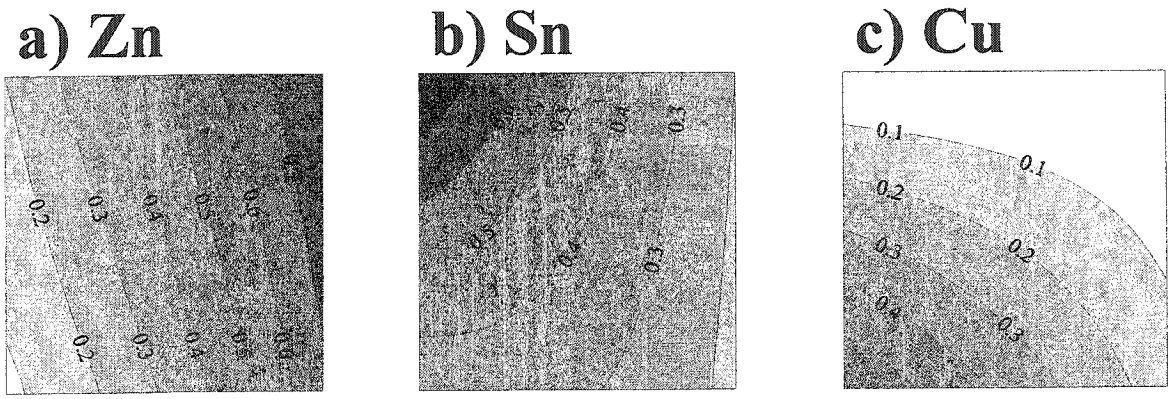

Figure 4-36 Cu-Sn-Zn contour plots generated using the results from the first model

The contour plots in Figure 4-36 do not exactly match the contour plots shown in Figure 4-33. However, the overall structure of the contour plots generated by the model is encouraging. As in Figure 4-33 the variation of atomic % Zn is almost linear and

slightly slanted to the right. Sn is concentrated in the top left hand corner and decreases outwards, as expected. Compared to Figure 4-33 the model predicts too much Sn in the bottom left and far right. Atomic % Cu is high at the bottom left and decreases towards the top right, as expected. Also, the curvature of the contour plots decreases from left to right, as seen in Figure 4-33.

An attempt was made to improve the model by considering that the exchange rate may vary with film thickness. In the first model an equal amount of Cu was exchanged from left to right. In the second model the number of exchanged Cu units depends on both x and y (as defined in Figure 4-35). Consider the bottom of the film in Figure 4-35, where y = 0 and x is allowed to vary. Let us now assume that the number of exchanged Cu units varies linearly from left to right. The model was set up such that 40 units were exchanged at the bottom left, 80 at the bottom right and 60 at the middle of the bottom. For y = 0, the number of exchanged Cu units ($Cu_{exchanged}$) varies as a function of position along the x-axis. The variation is given by equation 4.6.4-4:

$$Cu_{exchanged} = 40 + 4 \cdot n_x \qquad (4.6.4\text{-}4)$$

where n_x is the number of steps in the x-direction, ranging from 0-10 steps.

Given the immersion process used, $Cu_{exchanged}$ will also vary with y. $Cu_{exchanged}$ varies linearly with y. As y increases, the number of exchanged Cu units is reduced. Equation 4.6.4-4 can be modified to take this into consideration. Equation 4.6.4-5 is used to track the number of exchanged Cu units as a function of both x and y:

$$Cu_{exchanged} = 40 + 4 \cdot n_x - (0.4 \cdot n_x + 4) \cdot n_y \qquad (4.6.4\text{-}5)$$

where n_x is the number of steps in the x-direction, and n_y is the number of steps in the y-direction, both range from 0-10 steps. For example, consider the bottom of the film: at x

=y = 0, 40 units of Cu are exchanged. At y = 0 and x = 5, 60 units of Cu are exchanged. At y = 0 and x = 10, 80 units of Cu are exchanged. Half-way up the film, half the number of Cu units are exchanged (compared to the bottom), for example: at y = 5 and x = 0, 20 units of Cu are exchanged, at y = 5 and x = 5, 30 units of Cu are exchanged and at y = 5 and x = 10, 40 units of Cu are exchanged. Similarly, at the top of the film (y = 10) no Cu is exchanged.

Figure 4-37 represents contour plots generated from the results obtained using the second model:

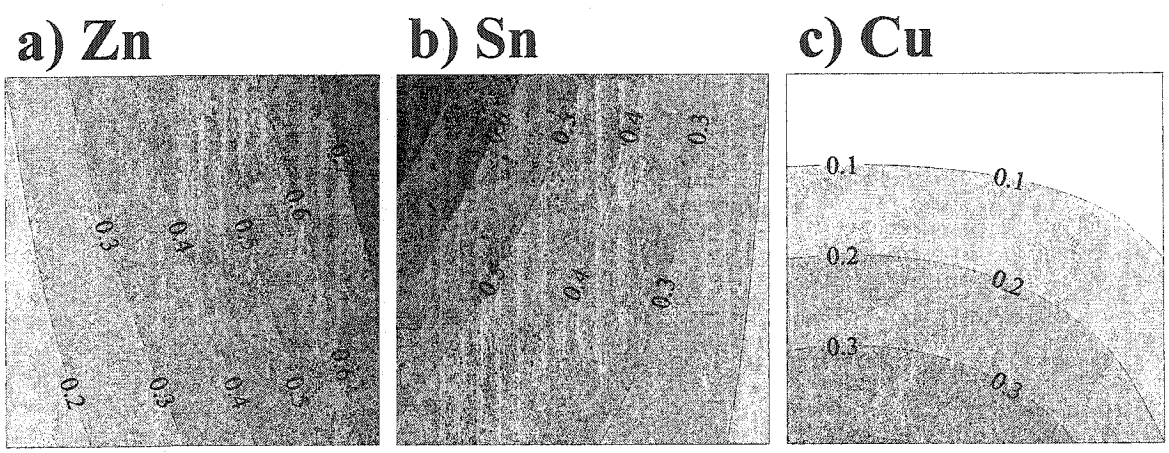

Figure 4-37 Cu-Sn-Zn contour plots generated from the results obtained using the second phenomenological model

Compared to the contour plots generated by the first model (Figure 4-36) the Zn contour plot is almost identical. Overall, the curvature of the Sn contours has been reduced, especially near the bottom left-hand corner. Atomic % Cu is also reduced at the bottom left-hand corner.

The composition versus position maps generated by the two models do not exactly reproduce the experimental composition maps in Figure 4-33. However, the contour plots generated by the models do accurately mimic the general trends seen experimentally. For example, the atomic % Zn varies almost linearly from left to right, as observed in the experimental data. The atomic % Sn is largest in the top left-hand corner, decreases from left to right, and top to bottom, as observed experimentally. The atomic % Cu is largest in the bottom left-hand corner, decreases from bottom to top, and left to right, as observed experimentally. All of these trends are expected given the immersion deposition process.

The model should be improved by a future student. An example of a possible improvement could be the dependence of the Cu ion-exchange rate on the thickness of the film. It is likely that ion-exchange will slow in deeper regions of thick films. However, in its current state the model represents a good starting point for future work.

5 Future Work

5.1 Anomalous high-voltage irreversible capacity in electroplated Sn electrodes for Li batteries

Section 4.1 outlined our discovery of anomalous high-voltage irreversible capacity (AHVIC) in Sn electrodes. A theory regarding the catalytic decomposition of electrolyte by Sn crystallites was proposed as well as a method to avoid it. The catalytic decomposition reaction of Li with electrolyte must proceed at a limiting rate. Furthermore, it was shown that only "clean" (i.e.: unlithiated) Sn had catalytic properties. Therefore, if Li was supplied to the Sn electrode at a rate faster than the catalytic reaction could consume it, the underlying Sn would be converted to its lithiated form, which does not apparently support the catalytic reaction. In [5.1] this phenomena was exploited to aid in the study of volume changes in Sn electrodes.

Although our theory was successful in describing the underlying cause and behavior of anomalous, high-voltage irreversible capacity, it says nothing about the decomposition products. In order to fully understand the catalytic reaction of Li with electrolyte a full chemical analysis should be performed on the decomposition products. In [5.1] it was shown that a film of decomposition products is observed after the presence of anomalous high-voltage irreversible capacity. It should be relatively easy to isolate the film from solution and analyze using XRD, WDS or mass spectrometry. Given the wide-spread use of Sn in advanced electrode materials for Li-ion batteries it is important to

fully understand the cause of anomalous high-voltage irreversible capacity and ways to avoid it.

5.2 Further studies in combinatorial electrodeposition

In four years three different binary systems and one ternary system were studied using combinatorial electrodeposition; Cu-Sn, Cu-Zn, Sn-Zn and Cu-Sn-Zn. The possibility of studying other binary systems is virtually limitless. While electrodeposition excels in operational cost, deposition speed and scalability, it lacks versatility compared to conventional combinatorial fabrication methods, such as sputter deposition. Aqueous electrodeposition is limited to metals that deposit before the breakdown potential of water. Furthermore, some aqueous plating chemistries may not be compatible. Although the Cu-Sn, Cu-Zn and Sn-Zn systems worked well, it may be difficult to deposit, for example, Cr-Zn. Cr is often deposited from a cyanide based solution, while Zn is easily deposited from a simple aqueous bath. Also, their reduction potentials are very close, -0.74 V vs. SHE for $Cr^{+3} + 3e^{-} \rightarrow Cr$ and –0.763 V vs. SHE for $Zn^{+2} + 2e^{-} \rightarrow Zn$, which would make it difficult to deposit one species without also depositing the other.

Combinatorial material science via electrodeposition can be applied to many, but not all, systems. Regardless of the inherent difficulties there are many interesting combinations to explore. Table 5-1 lists common active and inactive metals (with respect to alloying with Li) easily deposited from aqueous solution.

Table 5-1 List of common active and inactive elements (with respect to alloying with Li) that can be deposited from aqueous solution [1.10]

Active	Inactive
Sn	Co
Zn	Fe
Pb	Pd
Bi	Ni
Ag	Cu
Au	Mn
Cd	Cr
Pt	

There are $7 \times 8 = 56$ possible active/inactive binary combinations and ${}_8C_2 = 28$ active/active combinations for a total of 84. There are $8 \cdot ({}_7C_2) = 168$ one active, two inactive ternary compounds, $7 \cdot ({}_8C_2) = 196$ two active, one inactive ternary compounds and ${}_8C_3 = 56$ active/active/active ternary compounds for a total of 420. The sum of possible ternary and binary alloys tops off at 504. Each combination would require extensive research and analysis. As discussed in section 4.2 the performance of a metal-alloy electrode in a Li cell strongly depends on the active:inactive atomic ratio. To determine the optimal ratio numerous experiments would have to be performed, each one requiring an electrodeposited film with a unique active:inactive atomic ratio. Combinatorial material synthesis would greatly accelerate the analysis since a range of active:inactive ratios is sampled in a single electrodeposition run. The motivation to

further explore active:inactive binary alloys is supported by recent results involving Sn:Ni binary alloys which show relatively large capacities (550 mAh/g) with good capacity retention over many (>40) cycles [5.2].

5.3 Amorphous metal alloys

Amorphous negative electrode materials are an attractive alternative to crystalline materials, which exhibit poor cyclability due to cracking and pulverization problems. During lithiation amorphous alloys do not have two-phase regions, therefore there is no volume mismatch between phases and problems associated with pulverization are reduced. Amorphous alloys can be deposited electrochemically [5.3-11], but are not common. Of particular interest are amorphous films containing P, Ni-P in particular. P has a high capacity for alloying with Li (2593 mAh/g), however, most amorphous P alloys have a low P content. A short literature review suggests the highest achievable P content in an amorphous Ni-P film is 32% [5.12]. This is not high enough for practical use in a Li-ion battery. If P content could be increased an amorphous Ni-P electrode may be a viable electrode alternative. Amorphous Ni-Sn-P alloys have also been studied [5.11], however, similar to amorphous Ni-P, the Sn and P contents are not high enough to be useful electrode materials.

Using an amorphous Ni-P plating bath amorphous Ni-P films were deposited. Preliminary results suggest a P content of approximately 25%, it is not obvious how the P content could be increased. Near-amorphous (nano-crystalline) Ni-Zn and Cu-Zn have also been deposited. These alloys should actively alloy with Li due to the presence of Zn, but they do not. This behavior has been seen elsewhere [5.13], and is not understood.

Further study into the inactivity of these alloys is warranted, especially considering the recent interest in amorphous alloys as advanced negative electrode materials.

Amorphous alloys such as Si_xSn_{1-x} are especially interesting due to their large specific and volumetric capacity. Currently these alloys are made by sputter deposition, which is expensive and slow. If amorphous Si_xSn_{1-x} could be made by an inexpensive, scalable method such as electrodeposition they could be mass produced at an acceptable cost and speed. Some other interesting amorphous alloys discussed in the references above are: Co-P, Fe-P and $NiFe_{0.29}P_{0.18}$.

5.4 Another method for ternary combinatorial material synthesis via electrodeposition

In sections 4.4-5 combinatorial material synthesis was performed in a Hull cell to deposit binary phases of Cu and Sn. In section 4.6 combinatorial electrodeposition was extended to a ternary system using immersion plating. To create the ternary film two separate steps were needed. It would be useful to develop a similar process to deposit ternary alloys in a single step. Section 5.2 briefly discusses the combination of ternary alloys that could, in theory, be deposited from an aqueous solution. Pulsed deposition is well suited for a binary system, but not necessarily a ternary system, however, it could be done, consider the modified Hull Cell presented Figure 5-1.

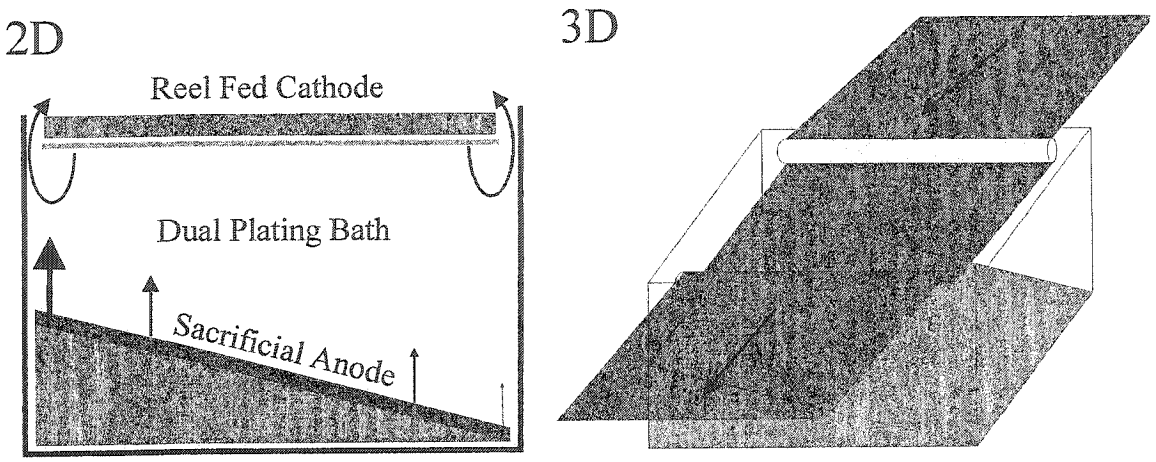

Figure 5-1 Combinatorial electrodeposition of ternary alloys using a reel fed cathode in a Hull cell with a soluble sacrificial anode

At the beginning of the experiment the plating solution would consist of only two species, say Zn and Cu. Zn deposits at a SHE potential of –0.763 V, Cu deposits at 0.342 V. Zn would be the concentrated species since Cu deposits more readily. A pulsed waveform similar to the one used in section 4.4 would be applied to the Hull cell. The first few pulsed waveforms would deposit alternating layers of Cu and Zn. Consider what would happen if Pb is used as the sacrificial anode. As the experiment proceeds, Pb^{+2} ions enter into solution because electrons are being removed from the sacrificial Pb anode and are used to deposit material at the cathode. The concentration of Pb will initially increase as a function of time. Pb deposits at a SHE potential of –0.125 V, it will not deposit during the Cu pulse, but it will deposit during the Zn pulse. The amount of Pb deposited should depend on its concentration in solution.

A Ni foil cathode would be reel fed through the solution. The Cu/Zn layers deposited at the beginning of the experiment would no longer be exposed to the plating solution by the time the Pb concentration was appreciable. This way, the Pb concentration varies as a function of position along the length of the cathode (while the

Cu/Zn concentration varies along the width). Determining the proper Cu and Zn concentrations in the bath would be critical, as well as controlling the rate at which the Ni cathode is fed through the bath. However, if successful, this method of producing composition-spread ternary alloys would be simple, fast and inexpensive, as desired.

5.5 Theoretical Model

Electrodeposition involves a large number of phenomena that are important simultaneously at widely different time and length scales. They represent difficult modeling problems. For example, the reaction rate is typically influenced, but not solely determined by, transport phenomena. Also, the near-surface chemistry usually depends on a number of homogeneous and heterogeneous reactions, and the equilibria among species is often uncertain. In addition, the quality of the deposit is often controlled by adsorption phenomena, surface films and/or molecular-scale events that involve additives which influence the course of lattice modification. An attempt to design a comprehensive model of the interactions of all the phenomena mentioned above would not be practical, but you have to start somewhere.

A model designed from a network of resistors and capacitors in series and parallel may be sufficient to describe complicated galvanostatic voltage profiles. Simple galvanostatic voltage profiles can be modeled using a parallel RC circuit [2.4] shown in Figure 5-2.

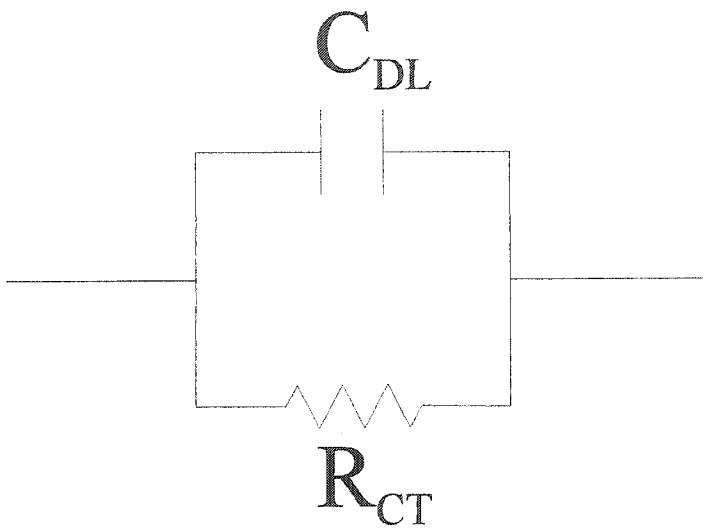

Figure 5-2 Schematic of a parallel RC circuit used to model simple galvanostatic deposition

Where C_{DL} is the double-layer capacitance of the test electrode and R_{CT} is the charge-transfer resistance of the electrode reaction.

It would be particularly interesting to model the current density distribution in a Hull cell. The model could be used to solve future challenges.

5.6 Nanocomposites

Our attempts to fabricate a nanostructured material using electrodeposition have not been successful. During that time our understanding of electrodeposition has grown exponentially. Nanocomposites have been deposited by electrodeposition techniques [4.17-22], but not with the active:inactive combinations we require. Using techniques like dual-bath pulse plating we believe active:inactive nanocomposites can be deposited. A list of possible active:inactive binary alloys can be found in Table 5-1. The search for suitable active:inactive metal-alloys and metal-alloy nanocomposites will proceed in

tandem. Again, the ability to perform combinatorial material science would greatly accelerate the research.

5.7 Masked electrodeposition on a 64 channel combinatorial cell plate

In the last few years the combinatorial material science infrastructure at Dalhousie has grown significantly. One example of this infrastructure is the development of a 64 channel combinatorial electrochemical cell (combi cell) for testing composition-spread libraries of metal-alloy negative electrodes. The success of the 64 channel combinatorial cell plate can be attributed to many people, but the bulk of the work was done by Mike Fleichauer and Tim Hatchard. Furthermore, the supporting software used to analyze the large amount of data produced by such an experiment was developed in house by Mike Fleichauer. Refer to [5.14] for more information. The combi cell allows 64 unique electrode materials to be tested in parallel. Typically, electrode materials of similar, but different, compositions are tested. The data is then analyzed with special attention paid to total capacity and cyclability. Using the software developed by Mike Fleichauer data from all 64 channels can be viewed simultaneously, making it easy to identify trends and select composition ranges where the electrode material has both high capacity and good capacity retention.

Figure 5-3 schematically shows the lead pattern onto which 64 negative electrode materials are deposited and tested in the combi cell.

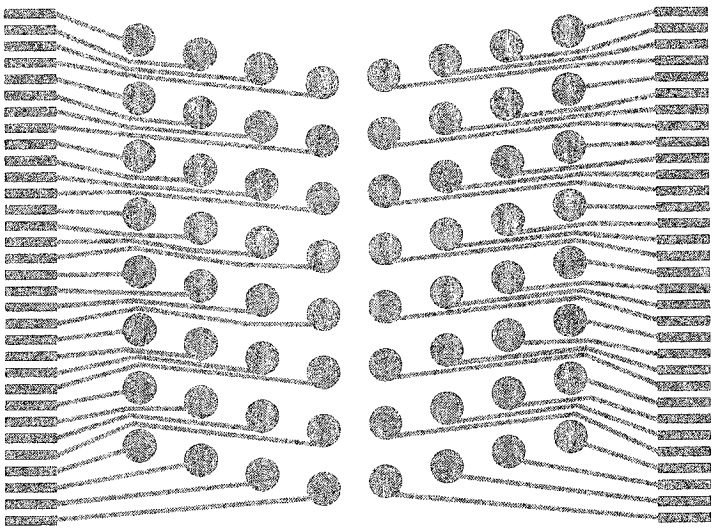

Figure 5-3 Schematic representation of the 64-channel electrode used in the combinatorial cell

The lead pattern is created using sputter deposition and photolithograpy. A thin (~1 μm) Cu layer is sputter deposited onto 3×3″ glass slides. The glass slide is then spun coat with ultra-violet (UV) sensitive photoresist. When the photoresist is exposed to UV light its chemical composition changes such that it can be washed away using acetone. UV light illuminates the slide through a mask that defines the lead pattern. The exposed photoresist is washed away and the underlying Cu is etched using nitric acid. The end product is a glass slide with the electrode pattern shown in Figure 5-3. Note the positions of the electrode pads, they are all staggered from one another. This is done to sample the largest range of binary phase space possible with a small compositional separation between electrodes.

Typically, sputter deposition is used to deposit test electrode material onto the pads and masked deposition is used to ensure the test material is deposited only on the pads and not the leads. The material is deposited in such a way that there is a

composition-spread between adjacent electrodes, for example, electrode #1 may consist of $Cu_{0.9}Sn_{0.1}$ while the electrode beside it, #2, is $Cu_{0.8}Sn_{0.2}$. The performance of electrode materials with similar compositions can be quickly compared, furthermore, trends are readily identified suggesting areas of future research.

To build on the success of the combi cell we wanted to prepare a composition-spread grid of electrodes using combinatorial electrodeposition. Electroplating on the 64 channel lead pattern presented numerous challenges. The masked sputter-deposition technique could not be used in electrodeposition since liquid would leak between the mask and glass slide resulting in deposition on the lead pattern as well as the electrode pads, which is unacceptable. The electrodeposition strategy still required masked deposition but a new technique had to be developed. Our first inclination was to use the photoresist to mask the leads, but not the pads. Unfortunately the resist partially dissolved in the plating bath resulting in deposition on the lead pattern. Using a mask made from plater's tape was also investigated. Two difficulties arose, either the tape did not properly adhere to the glass slide and liquid leaked underneath resulting in deposition on the leads, or, the tape stuck so well that when it was removed it took most of the Cu with it. To be successful, the mask had to have two characteristics: 1) it is easily removed after deposition without damaging the Cu electrode pattern, and 2) capable of protecting the lead pattern during deposition. Numerous candidates were tested including, but not limited to, band-aids, ink, grease, glue, contact-cement (DAP Weldwood product # DAP-00107), and bubble-gum. Unfortunately, none were successful. Jeff suggested the use of coal tar epoxy, which worked quite well. The lead pattern in Figure 5-3 was painted with coal tar epoxy, shown schematically in Figure 5-4.

Before painting, a thin strip of Cu is placed on either side of the glass slide and then joined together at the top effectively short-circuiting all the electrodes in preparation for electrodeposition.

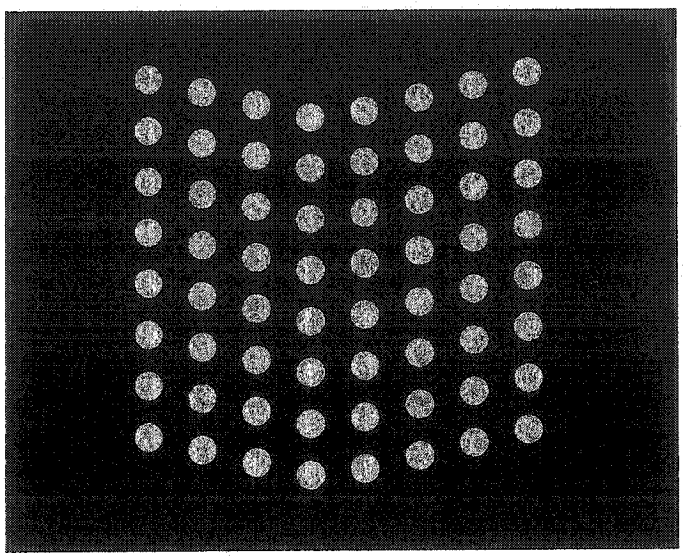

Figure 5-4 Coal tar epoxy painted on the lead pattern shown in Figure 5-3

The Sn-Zn bath used in section 4.6-1 was used to try and deposit a range of Sn-Zn alloys. The glass slide is positioned in the Hull cell in the same configuration as the Ni-foil discussed previously. The configuration should result in a current gradient from top to bottom of the glass slide, resulting in composition variation. Unfortunately, combinatorial electrodeposition on the pads shown above did not result in compositional variation. This is due to two factors: 1) the deposition area is too small, and Sn ions are not consumed fast enough, therefore deposition of Sn is not diffusion controlled and predominantly Sn deposits everywhere; 2) the separation distance between pads acts as a source of Sn ions. Sn ions in the area directly above the pad may be quickly consumed, but they are replaced by neighboring Sn ions above an area where deposition is not taking

place. Several options were considered to overcome these problems. The obvious solution was to increase the current, which would increase current density and therefore the rate at which Sn ions were consumed. Unfortunately we were already working at the maximum output current of the Keithley 236. Another option would be to decrease the Sn content, which whould encourage a larger current density gradient. This was tried without success. Given our previous success with the Sn-Zn pyrophosphate bath and a large surface area (discussed in section 4.6) we decided to increase the surface area by placing a piece of Cu foil over the glass slide such that it covered the painted epoxy but not the pads, shown schematically in Figure 5-5.

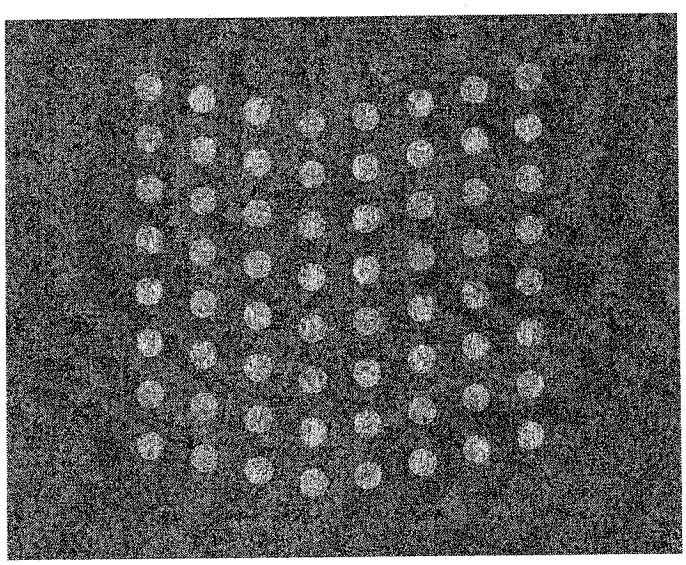

Figure 5-5 Cu foil placed over the coal tar epoxy painted glass slide with punches cut out above the electrode pads

The punches in the Cu foil had to exactly line up with the pads underneath, which could not be done simply by eye. Instead the Cu foil was taped to a regular piece of

paper and then fed though a bubble-jet printer. The same file used to make the masks for photoresist UV exposure was used to print the exact positions of the electrode pads onto the Cu foil. The pattern was then punched from the foil. A schematic of the printed Cu foil is shown in Figure 5-6. Another schematic is shown in Figure 5-7 after the pad positions have been punched out.

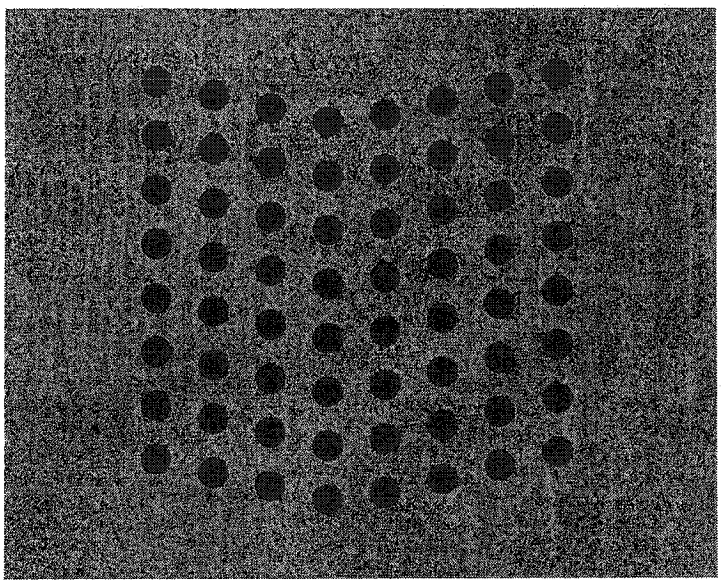

Figure 5-6 Electrode pad positions printed onto Cu foil using a bubble-jet printer

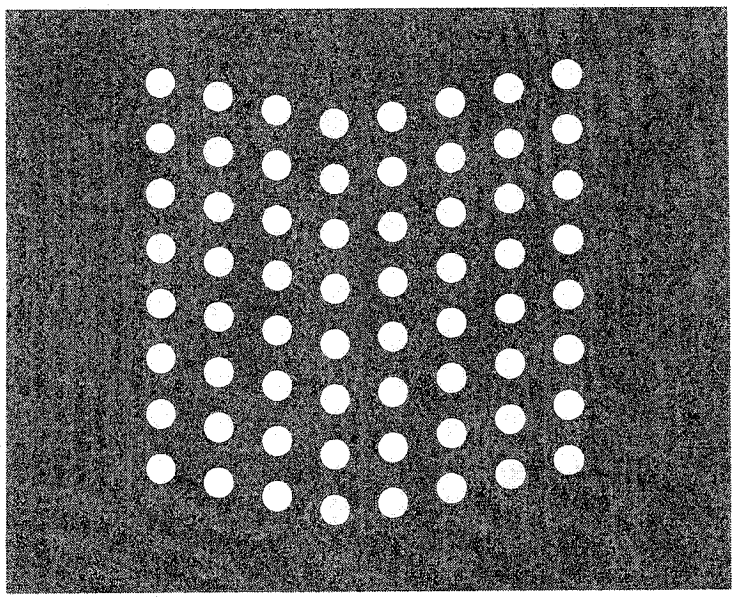

Figure 5-7 Cu foil after the electrode positions have been punched out

Compositional variation was assured when plating on the slide shown in Figure 5-5 because it was as though we were plating on regular foil. A composition-spread was successfully deposited, a schematic of the successful film is given in Figure 5-8.

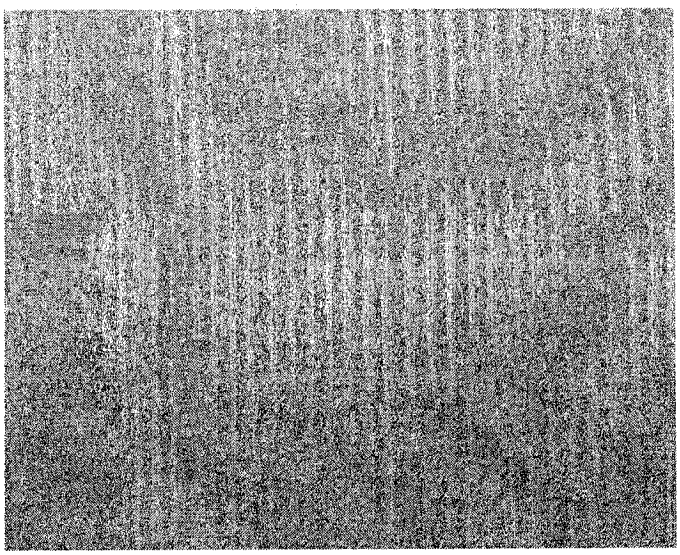

Figure 5-8 Composition-spread film deposited onto the coal tar epoxy painted, Cu foil masked glass slide

The punched Cu foil was then removed and the coal tar epoxy washed off using acetone. The entire process usually took 6-7 hours. If the coal tar epoxy was left to cure longer than 9 or 10 hours it could not be removed using actetone. Also, the coal tar epoxy had to be removed gently, or else the Cu lead pattern would be removed as well. The final electrodeposited lead pattern is presented in Figure 5-9.

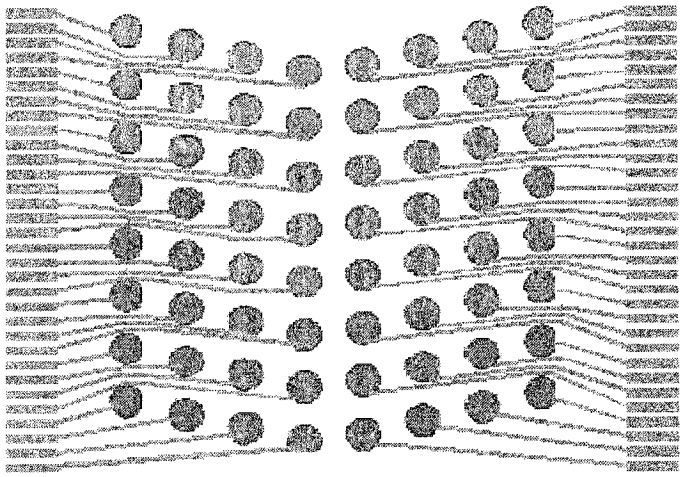

Figure 5-9 Lead pattern with a composition-spread film electrodeposited on the pads only

EDS measurements were performed on the punched Cu foil after electrodeposition and removal from the patterned glass slide. Numerous measurements were made along the left hand side of the film where no punches were removed (e.g.: left hand side of Figure 5-8). The results are presented in Figure 5-10.

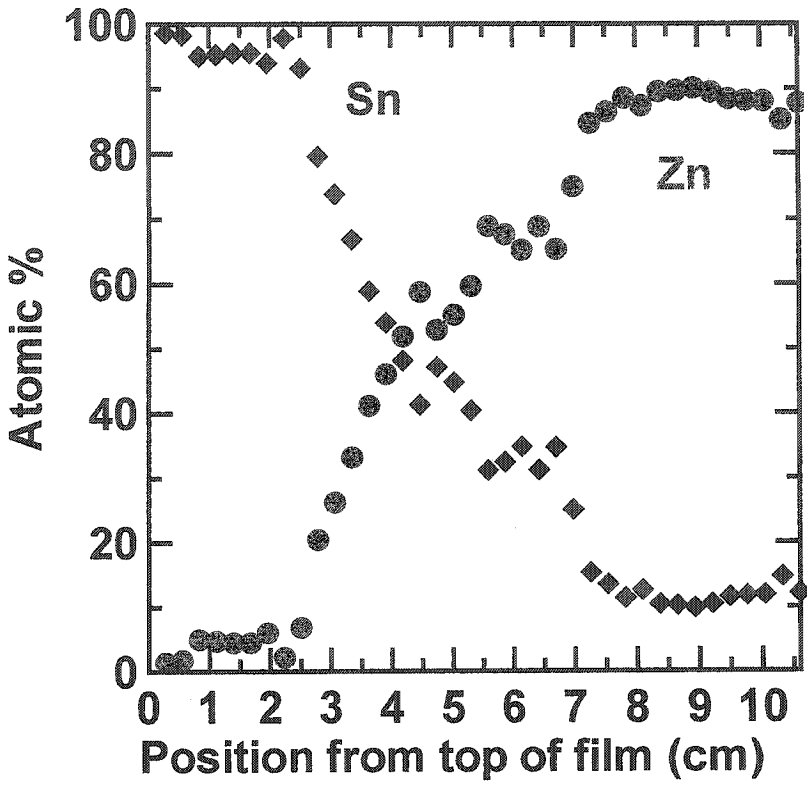

Figure 5-10 EDS measurements along the punched Cu foil after deposition and removal from patterned glass slide

From Figure 5-10 deposition was highly successful in sampling a large region of composition space, almost 90% of composition space was sampled on one film. Furthermore, individual compositions are addressable by the lead pattern. The potential to study 90% of a binary phase diagram in a single experiment is very exciting,

Unfortunately the project stopped there due to time restrictions. A few of these masked-deposition slides have been tested in a full combi-cell with disappointing results. Removal of pieces of the Cu lead pattern during plating and coal tar epoxy removal is a major problem. When the Cu lead pattern is damaged or removed the pad is no longer in electrical contact, rendering it useless. We're confident that these problems could be

resolved with minimal time and effort and the method could be used to quickly and inexpensively deposit composition-spread films ready to test in the combinatorial cell.

6 Conclusions

Below is a concise list of conclusions that can be drawn from the thesis:

- Do not blindly accept the results of a WDS analysis. Make sure the results make sense. If they do not, look for interference due to second order diffraction reflections.
- The Sn-based electrodes we tested displayed relatively low capacity and relatively poor capacity retention, discouraging their use in commercial Li-ion batteries.
- In theory, Sn-based nano-composites will have both high capacity and good capacity retention. They may one-day replace carbon as the negative electrode material in Li-ion batteries.
- Advanced negative electrode materials for Li-ion batteries can be made quickly, simply and inexpensively using electrodeposition.
- Anomalous high-voltage irreversible capacity (AHVIC) has been identified in Sn-based electrodes. AHVIC was observed in Sn electrodes prepared by electrodeposition, sputtering and from powder composites.
- A theory describing the cause of AHVIC has been proposed. Sn acts as a catalyst in the decomposition of electrolyte.
- A theory describing AHVIC is proposed that explains how to eliminate AHVIC. Three ways to avoid AHVIC are: 1) keep the recharge voltage below 1.3 V (vs. Li); 2) cycle the cell at a rate above 76 mA/cm^2 and 3) by alloying Sn with another element (such as Cu).

- We could not fabricate a Cu-Sn nanocomposite using the pulsed electrodeposition method. It's doubtful that a nano-composite could be fabricated this way due to interdiffusion.
- Cu-Sn alloys are easily deposited using pulsed electrodeposition. The composition of the electrodeposited alloy is easily controlled using a pulsed waveform.
- In a Li/Cu-Sn cell capacity retention is improved by raising the discharge cut-off voltage to 0.2 V from 0 V.
- Cu-Sn alloy electrodes rich in Sn displayed large capacity but poor capacity retention. Cu-Sn alloy electrodes rich in Cu displayed low capacity with good capacity retention.
- Combinatorial electrodeposition has been successfully developed and implemented.
- Composition and crystal structure of Cu-Sn alloys vary smoothly along the length of the electrodeposited composition-spread film.
- A composition-spread film of electrodeposited alloys will not necessarily follow the equilibrium phase diagram; since electrodeposition is not an equilibrium process.
- Using our electrodeposition method the formation of the $Cu_{41}Sn_{11}$ phase is favored over Cu_3Sn.
- We found that a Cu-Sn electrode containing 28 atm. % Sn displayed the best tradeoff of high capacity and good capacity retention.
- Combinatorial electrodeposition is easily extended to other binary systems, such as Cu-Sn, Cu-Zn and Sn-Zn.
- Electrodeposition is scalable, materials developed in the lab can be easily mass produced.

- Large regions of composition space are easily sampled using combinatorial electrodeposition.
- Combinatorial electrodeposition has been extended to ternary alloys while preserving the simplicity and inexpensive nature of the process.
- A simple model is sufficient to describe the overall trends observed in the contour plots of the composition-spread electrodeposited ternary film.
- Ingenuity replaces robots and million-dollar machines with water guns and buckets
- There are numerous simple, interesting projects left to be explored using the groundwork we have developed.
- A list of conclusions often ends in disappointment with an uninspiring comment or sweeping generalization exaggerating the significance of the thesis. I will make no such attempt to glamorize this work and leave you with some useful advice: Live for the nights you'll never remember, with the friends you'll never forget..

References

[1.1] J.M Tarascon and M. Armand, Nature, **414**, 359, 2001

[1.2] L. Y. Beaulieu, "Atomic Force Microscopy Studies of the Reaction of Lithium with Amorphous Si-Sn alloys", PhD Thesis, Dalhousie University, Halifax, N.S., 2002

[1.3] M. Obrovac T. Hatchard and J. Dahn, added talk to session C2, 204th Meeting of The Electrochemical Society, 2003

[1.4] J. R. Dahn, U. von Sacken, M. W. Juzkow and H. Al-Janaby, Journal of the Electrochemical Society, **138**, 2207, 1991

[1.5] I.A. Courtney, "The Physics and Chemistry of Metal Oxide Composites as Anode Materials for Lithium-Ion Batteries", PhD Thesis, Dalhousie University, Halifax, N.S., 1999

[1.6] J.O. Besenhard, "Handbook of Battery Materials", Wiley Press, NY, USA, 1999

[1.7] Dr. David R. Lide (editor), "CRC Handbook of Chemistry and Physics 84th edition", CRC Press, 1999

[1.8] N.W Ashcroft and N.D. Mermin, "Solid State Physics", Saunders College Publishing, Orlando, Florida, 1976

[1.9] T. Zheng, "The Physics and Chemistry of High Capacity Carbonaceous Materials for Lithium-Ion Batteries", PhD thesis, Simon Frasier University, Burnaby, B.C., 1996

[1.10] W. G. Moffat, "The Handbook of Binary Phase Diagrams", Genium Publishing Corp., Schenectady, New York, 1990

[1.11] E. Peled, Journal of the Electrochemical Society, **126**, 2047, 1979

[1.12] D. Aurbach, Y. Ein-Eli, O. Chusid, Y. Carmeli, M. Babai, H. Yamin, Journal of the Electrochemical Society, **141**, 603, 1994

[1.13] A. Naji, J. Ghanbaja, B. Humbert, P. Willmann, D. Billaud, Journal of Power Sources, **63**, 33, 1996

[1.14] D. Aurbach, Y. Gofer, B. Nez-Zion, P. Aped, Journal of Electroanalytical Chemisrty, **339**, 451, 1992

[1.15] D. Aurbach, I. Weissman, A. Schechter, H. Cohen, Langmuir, **12**, 3991, 1996

[1.16] D. Aurbach, Y. Ein-Eli, B. Markovsky, A. Zaban, S. Luski, Y. Carrmeli, H. Yannin, Journal of the Electrochemical Society, **142**, 2882, 1995

[1.17] D.D. MacNeil, "Lithium-ion Battery Reactions at Elevated Temperatures", PhD Thesis, Dalhousie University, Halifax, N.S., 2001

[1.18] O. Mao and J.R. Dahn, Journal of the Electrochemical Society, **146**, 414, 1999

[1.19] K.D. Kepler, J.J. Vauger and M.M. Thackery, Electrochemical Solid State Letters, **2**, 307, 1999

[1.20] K.D. Kepler, J.J. Vauger and M.M. Thackery, Journal of the Electrochemical Society, **146,** 1, 423, 1999

[1.21] I.A. Courtney, W. R. McKinnon and J. R. Dahn, Journal of the Electrochemical Society, **146**, 59, 1999

[1.22] I.A. Courtney and J. R. Dahn, Journal of the Electrochemical Society, **144**, 2943, 1997

[1.23] I.A. Courtney, J. S. Tse, O. Mao, J. Hafner and J. R. Dahn, Phys. Rev. B, **58**, 15583, 1998

[1.24] J. Schoonman, Solid State Ionics, **135**, 5, 2000

[2.1] R. Woldsseth, "X-ray Energy Spectroscopy", Kevex Corporation, Burlingame, California, 1973

[2.2] A. Kronz, Technical sketch sent by e-mail correspondence from of the Geochemical Institute,University of Goettingen, Goldschmidtstrasse 1, 37077 Goettingen.

[2.3] "X-ray emission and absorption wavelengths and L-value tables", book of tables included with JEOL JXA 8900 RL SuperProbe, JEOL, 2001

[2.4] M. Paunovic and M. Schlesinger, "Fundamentals of Electrochemical Deposition", Electrochemical Society Series, Wiley-Interscience publication, NY, USA, 1998

[2.5] R.O. Hull, Trans. Am., Electroplat. Soc., **27**, 52, 1939

[2.6] W.A. Caspari, Z Physik. Chem., **30**, 89, 1899

[2.7] J. Tafel, Z Physik. Chem., **50**, 641, 1905

[3.1] J.O'M. Bockris and A.K.N. Reddy , "Modern Electrochemistry", Volume 2, Plenum Press, 1970

[3.2] S. Mayer , Presented Talk, Gordon conference on Electrodeposition, 2000

[3.3] S. Roy, M. Matlosz and D. Landolt, Journal of the Electrochemical Society, **141**, 6, 1994

[3.4] C.C. Yang and H. Y. Cheh, Journal of the Electrochemical Society, **142**, 9, 1995

[3.5] A. Rousseau and P. Benaben, Plating and Surface Finishing, 106, 1999

[3.6] T. M. Rodgers, "Handbook of Practical Electroplating", The Macmillan Company, 1959

[4.1] J. Yang, M. Winter and J.O. Besenhard, Solid State Ionics, **90**, 281, 1996

[4.2] M. Winter and J.O. Besenhard, Electrochemica Acta, 31, 1999

[4.3] J.O. Besenhard, J. Yang and M. Winter, Extended Abstracts, Eighth International Meeting on Lithium Batteries, 1996

[4.4] A.A. Anami, S. Crouch-Baker and R.A. Huggins, Solid-State Science and Technology, **135**, 8, 2103, 1988

[4.5] R.A. Huggins, Lithium Alloy Anodes, "Handbook of Battery Materials", Chapter 4, edited by J.O. Besenhard, Wiley-VCH, Weinheim, 1999

[4.6] A.H. Whitehead, J. M. Elliott and J. R. Owen, Journal of Power Sources, 81, 1999

[4.7] T. Brousse, O. Crosnier, X. Devaux, P. Fragnaud, P. Paillard, J. Santos-Pena, and D.M. Schleich, Powder Technology, **128**, 124, 2002

[4.8] J. Santos-Pena, Tt. Brousse, L. Sanchez, J. Morales and D.M. Schleich, Journal of Power Sources, **97**, 232, 2001

[4.9] O. Crosnier, T. Brousse, X. Devaux, P. Fragnaud and D.M. Schleich, Journal of Power Sources, **94**, 169, 2001

[4.10] J Santos-Pena, T. Brousse and D.M. Schleich, Solid State Ionics, **135**, 87, 2000

[4.11] R. Retoux, T. Brousse and D. M. Schleich, Journal of the Electrochemical Society, **146**, 2472, 1999

[4.12] S. Fujitani et. al, 3rd Hawai Battery Conference, 210, 2001

[4.13] L.Y. Beaulieu, A. Bonakdarpour, T.D. Hatchard, M.D. Fleischauer and J.R. Dahn, Journal of the Electrochemical Society, **150**, 1457, 2003

[4.14] S. D. Beattie, T. Hatchard, A. Bonakdarpour, K. C. Hewitt, and J. R. Dahn, Journal of the Electrochemical Society, **150**, 701, 2003

[4.15] O. Mao, R.L. Turner, I. A. Courtney, B. D. Fredericksen, M. I. Buckett, L. J. Krause and J. R. Dahn, Electrochemical and Solid State Letters, **2**, 3, 1999

[4.16] L.Y. Beaulieu, D. Larcher, R.A. Dunlap and J.R. Dahn, Journal of the Electrochemical Society, **147**, 3206, 2000

[4.17] A. Haseeb, B. Blanpain, G. Wouters, J.P. Celis and J.R. Ross, Materials Science and Engineering, **168**, 137, 1993

[4.18] S. Menezes and D.P. Anderson, Journal of the Electrochemical Society, **137**, 2, 1990

[4.19] R. Intrater and J. Yahalom. Materials Science Letters, **12**, 1549, 1993.

[4.20] J. Yahalom and O. Zadok, Journal of Materials Science, **22**, 499, 1987)

[4.21] D.S. Lashmore and M.P. Dariel, Solid-State Science and Technology, **135**, 1218, 1988

[4.22] M. Alper, K. Attenborough, R. Hart, S.J. Lane, D.S. Lashmore, C. Younes and W. Schwarzacher, Appl. Phys. Lett. **63,** 15, 1993

[4.23] J.O. Besenhard, J. Yang and M. Winter, in 8th Extended Abstracts of International Meeting on Lithium Batteries, Nagoya, Japan, 69, 1996

[4.24] O.V. Reva, T.N. Vorob'eva and V.V. Sviridov, Russian Journal of Electrochemistry **35**, 942 ,1999

[4.25] M. Hansen, "Constitution of Binary Alloys", 2nd Edition, Reprinted by Genium Publishing Corp, Schnectady, New York, 1989

[4.26] K.D Kepler, J.T. Vaughey and M.M. Thackeray, Journal of Power Sources, **81-82,** 383, 1999

[4.27] D. Larcher, L. Y. Beaulieu, D. D. MacNeil and J. R. Dahn, Journal of the Electrochemical Society, **147**, 1658, 2000

[4.28] K. Kennedy; T. Stefansky,G. Davy; V.F. Zackay, E.R.J. Parker, App. Phys., **36**, 3808, 1965

[4.29] J.J. Hanak, Mater. Sci, **5**, 964, 1970

[4.30] R.B. van Dover, L.F. Schneemeyer, R.M. Fleming, Nature, 392, 1998

[4.31] H. Chang, I. Takeuchi, X.D. Xiang, Appl. Phys. Lett., **74**, 1165, 1999

[4.32] X.D. Xiang, Annu. Rev. Mater. Sci., **29**, 149, 1999

[4.33] D. Landolt, Electrochemica Acta, **39**, 8, 1075, 1994

[4.34] S.D. Beattie and J.R. Dahn, Journal of the Electrochemical Society, **150**, 457, 2003

[5.1] L.Y. Beaulieu, S.D. Beattie, T.D. Hatchard and J.R. Dahn, Journal of the. Electrochemical Society, **150**, 419, 2003

[5.2] T. Momma, H. Mukaibo, T. Sumi, T. Yokoshima, and T. Osaka (Waseda University), abstract #324, 204th Meeting of The Electrochemical Society, Orlando Fl. U.S.A., October, 2003

[5.3] C.F. Chu, S.T. Wu, Materials Chemistry and Physics, **71**, 248, 2001.

[5.4] X.Z He, C.B. Xia, H.J. Wang, Z.Q. Gong, H.Y. Jiang, Transactions of Nonferrous Metals Society of China, 11, 956, 2001

[5.5] M.Y. Hua, R.Y Tsai, Thin Solid Films, **388**, 1, 165, 2001

[5.6] L. Perez, O de Abril, M.C. Sanchez, C. Aroca, E. Lopez, P. Sanchez, Journal of Magnetism and Magnetic Materials, **215**, 337, 2000.

[5.7] C.F.Chu, S.T. Wu, Journal of the Electrochemical Society, **147**, 2190, 2000

[5.8] P. Schlossmacher, T. Yamasaki, Mikrochimica Acta, **132**, 309, 2000

[5.9] M. Kjuchukova, V. Ivanova, G. Raichevski, S. Vitkova, Transactions of the Institute of Metal Finishing, **78**, 44, 2000

[5.10] A. Bukaluk, Surface and Interface Analysis, **22**, 18, 1994

[5.11] X. Haowen, Z. Bangwei, Y. Qiaoqin, Trans IMF, **3**, 77, 1999

[5.12] A. Bukaluk, Surface and Interface Analysis, **22**, 18, 1994

[5.13] D. Larcher, L.Y. Beaulieu, O. Mao, A.E. George and J.R. Dahn, Journal of the Electrochemical Society, **147**, 1703, 2000

[5.14] M.D. Fleischauer, T.D. Hatchard, G.P. Rockwell, J.M. Topple, S. Trussler and J.R. Dahn , Journal of the Electrochemical Society, **150**, 11, 1465, 2003

Appendix 1 Electron binding energies

Electron binding energies in eV for the elements in their natural forms

Values compiled by Gwyn Williams

Last updated April 20, 1995

The energies are given relative to the vacuum level for rare gases and H, N, O, F, and Cl diatomic molecules; relative to the Fermi level for metals; and relative to the top of the valence band for semiconductors.

Values are take from J. A. Bearden and A. F. Burr, "Reevaluation of X-Ray Atomic Energy Levels," *Rev. Mod. Phys.* **39**, (1967) p.125, except values marked '*' are from M. Cardona and L. Ley, Eds., *Photoemission in Solids I: General Principles* (Springer-Verlag, Berlin, 1978) with additional corrections, and values marked with '+' are from J. C. Fuggle and N. Mårtensson, "Core-Level Binding Energies in Metals," *J. Electron Spectrosc. Relat. Phenom.* **21**, (1980) p.275.

Notes: (a) One-particle approximation not valid owing to short core-hole lifetime. (b) Values derived from Bearden and Burr.

		K	L-I	L-II	L-III	M-I	M-II	M-III	M-IV	M-V	N-I	N-II	N-III
#		1s	2s	2p1/2	2p3/2	3s	3p1/2	3p3/2	3d3/2	3d5/2	4s	4p1/2	4p3/2
1	H	13.6											
2	He	24.6*											
3	Li	54.7*											
4	Be	111.5*											
5	B	188*											
6	C	284.2*											
7	N	409.9*	37.3*										
8	O	543.1*	41.6*										
9	F	696.7*											
10	Ne	870.2*	48.5*	21.7*	21.6*								
11	Na	1070.8+	63.5+	30.4+	30.5*								
12	Mg	1303.0+	88.6*	49.6+	49.21								
13	Al	1559.0	117.8*	72.9*	72.5*								
14	Si	1839	149.7*b	99.8*	99.2*								
15	P	2145.5	189*	136*	135*								
16	S	2472	230.9	163.6*	162.5*								
17	Cl	2822.0	270*	202*	200*								
18	Ar	3205.9*	326.3*	250.6+	248.4*	29.3*	15.9*	15.7*					

19	K	3608.4*	378.6*	297.3*	294.6*	34.8*	18.3*	18.3*					
20	Ca	4038.5*	438.4+	349.7+	346.2+	44.3+	25.4+	25.4+					
21	Sc	4492	498.0*	403.6*	398.7*	51.1*	28.3*	28.3*					
22	Ti	4966	560.9+	460.2+	453.8+	58.7+	32.6+	32.6+					
23	V	5465	626.7+	519.8+	512.1+	66.3+	37.2+	37.2+					
24	Cr	5989	696.0+	583.8+	574.1+	74.1+	42.2+	42.2+					
25	Mn	6539	769.1+	649.9+	638.7+	82.3+	47.2+	47.2+					
26	Fe	7112	844.6+	719.9+	706.8+	91.3+	52.7+	52.7+					
27	Co	7709	925.1+	793.2+	778.1+	101.0+	58.9+	59.9+					
28	Ni	8333	1008.6+	870.0+	852.7+	110.8+	68.0+	66.2+					
29	Cu	8979	1096.7+	952.3+	932.7	122.5+	77.3+	75.1+					
30	Zn	9659	1196.2*	1044.9*	1021.8*	139.8*	91.4*	88.6*	10.2*	10.1*			
31	Ga	10367	1299.0*b	1143.2+	1116.4+	159.51	103.5+	100.0+	18.7+	18.7+			
32	Ge	11103	1414.6*b	1248.1*b	1217.0*b	180.1*	124.9*	120.8*	29.8*	29.2*			
33	As	11867	1527.0*b	1359.1*b	1323.6*b	204.7*	146.2*	141.2*	41.7*	41.7*			
34	Se	12658	1652.0*b	1474.3*b	1433.9*b	229.6*	166.5*	160.7*	55.5*	54.6*			
35	Br	13474	1782*	1596*	1550*	257*	189*	182*	70*	69*			
36	Kr	14326	1921	1730.9*	1678.4*	292.8*	222.2*	214.4	95.0*	93.8*	27.5*	14.1*	14.1*
37	Rb	15200	2065	1864	1804	326.7*	248.7*	239.1*	113.0*	112*	30.5*	16.3*	15.3*
38	Sr	16105	2216	2007	1940	358.7+	280.3+	270.0+	136.0+	134.2+	38.9+	21.6+	20.1+
39	Y	17038	2373	2156	2080	392.0*b	310.6*	298.8*	157.7+	155.8+	43.8*	24.4*	23.1*
40	Zr	17998	2532	2307	2223	430.3+	343.5+	329.8+	181.1+	178.8+	50.6+	28.5+	27.1+
41	Nb	18986	2698	2465	2371	466.6+	376.1+	360.6+	205.0+	202.3+	56.4+	32.6+	30.8+
42	Mo	20000	2866	2625	2520	506.3+	411.6+	394.0+	231.1+	227.9+	63.2+	37.6+	35.5+
43	Tc	21044	3043	2793	2677	544*	447.6*	417.7*	257.6*	253.9*	69.5*	42.3*	39.9*
44	Ru	22117	3224	2967	2838	586.1*	483.3+	461.5+	284.2+	280.0+	75.0+	46.3+	43.2+
45	Rh	23220	3412	3146	3004	628.1+	521.3+	496.5+	311.9+	307.2+	81.4*b	50.5+	47.3+
46	Pd	24350	3604	3330	3173	671.6+	559.9+	532.3+	340.5+	335.2+	87.1*b	55.7+a	50.9+
47	Ag	25514	3806	3524	3351	719.0+	603.8+	573.0+	374.0+	368.3	97.0+	63.7+	58.3+
48	Cd	26711	4018	3727	3538	772.0+	652.6+	618.4+	411.9+	405.2+	109.8+	63.9+a	63.9+a
49	In	27940	4238	3938	3730	827.2+	703.2+	665.3+	451.4+	443.9+	122.9+	73.5+a	73.5+a
50	Sn	29200	4465	4156	3929	884.7+	756.5+	714.6+	4g3.2+	484.9+	137.1+	83.6+a	83.6+a
51	Sb	30491	4698	4380	4132	940+	812.7+	766.4+	537.5+	528.2+	153.2+	95.6+a	95.6+a
52	Te	31814	4939	4612	4341	1006+	870.8+	820.8+	583.4+	573.0+	169.4+	103.3+a	103.3+a
53	I	33169	5188	4852	4557	1072*	931*	875*	630.8	619.3	186*	123*	123*
54	Xe	34561	5453	5107	4786	1148.7*	1002.1*	940.6*	689.0*	676.4*	213.2*	146.7	145.5*
55	Cs	35985	5714	5359	5012	1211*b	1071*	1003*	740.5*	726.6*	232.3*	172.4*	161.3*
56	Ba	37441	5989	5624	5247	1293*b	1137*b	1063*b	795.7+	780.5*	253.5+	192	178.6+
57	La	38925	6266	5891	5483	1362*b	1209*b	1128*b	853*	836*	274.7*	205.8	196.0*
58	Ce	40443	6548	6164	5723	1436*b	1274*b	1187*b	902.4*	883.8*	291.0*	223.2	206.5*
59	Pr	41991	6835	6440	5964	1511	1337	1242	948.3*	928.8*	304.5	236.3	217.6

60	Nd	43569	7126	6722	6208	1575	1403	1297	1003.3*	980.4*	319.2*	243.3	224.6
61	Pm	45184	7428	7013	6459	-	1471.4	1357	1052	1027	-	242	242
62	Sm	46834	7737	7312	6716	1723	1541	1419.8	1110.9*	1083.4*	347.2*	265.6	247.4
63	Eu	48519	8052	7617	6977	1800	1614	1481	1158.6*	1127.5*	360	284	257
64	Gd	50239	8376	7930	7243	1881	1688	1544	1221.9*	1189.6*	378.6*	286	271
65	Tb	51996	8708	8252	7514	1968	1768	1611	1276.9*	1241.1*	396.0*	322.4*	284.1*
66	Dy	53789	9046	8581	7790	2047	1842	1676	1333	1292*	414.2*	333.5*	293.2*
67	Ho	55618	9394	8918	8071	2128	1923	1741	1392	1351	432.4*	343.5	308.2*
68	Er	57486	9751	9264	8358	2206	2006	1812	1453	1409	449.8*	366.2	320.2*
69	Tm	59390	10116	9617	8648	2307	2090	1885	1515	1468	470.9*	385.9*	332.6*
70	Yb	61332	10486	9978	8944	2398	2173	1950	1576	1528	480.5*	388.7*	339.7*
71	Lu	63314	10870	10349	9244	2491	2264	2024	1639	1589	506.8*	412.4*	359.2*
72	Hf	65351	11271	10739	9561	2601	2365	2107	1716	1662	538*	438.2+	380.7+
73	Ta	67416	11682	11136	9881	2708	2469	2194	1793	1735	563.4+	463.4+	400.9+
74	W	69525	12100	11544	10207	2820	2575	2281	1949	1809	594.1+	490.4+	423.61
75	Re	71676	12527	11959	10535	2932	2682	2367	1949	1883	625.4+	518.7+	446.8+
76	Os	73871	12968	12385	10871	3049	2792	2457	2031	1960	658.2+	549.1+	470.7+
77	Ir	76111	13419	12824	11215	3174	2909	2551	2116	2040	691.1+	577.8+	495.8+
78	Pt	78395	13880	13273	11564	3296	3027	2645	2202	2122	725.4+	609.1+	519.4+
79	Au	80725	14353	13734	11919	3425	3148	2743	2291	2206	762.1+	642.7+	546.3+
80	Hg	83102	14839	14209	12284	3562	3279	2847	2385	2295	802.2+	680.2+	576.6+
81	Tl	85530	15347	14698	12658	3704	3416	2957	2485	2389	846.2+	720.5+	609.5+
82	Pb	88005	15861	15200	13035	3851	3554	3066	2586	2484	891.8+	761.9+	643.5+
83	Bi	90526	16388	15711	13419	3999	3696	3177	2688	2580	939+	805.2+	678.8
84	Po	93105	16939	16244	13814	4149	3854	3302	2798	2683	995*	851*	705*
85	At	95730	17493	16785	14214	4317	4008	3426	2909	2787	1042*	886*	740*
86	Rn	98404	18049	17337	14619	4482	4159	3538	3022	2892	1097*	929*	768*
87	Fr	101137	18639	17907	15031	4652	4327	3663	3136	3000	1153*	980*	810*
88	Ra	103922	19237	18484	15444	4822	4490	3792	3248	3105	1208*	1058	879*
89	Ac	106755	19840	19083	15871	5002	4656	3909	3370	3219	1269*	1080*	890*
90	Th	109651	20472	19693	16300	5182	4830	4046	3491	3332	1330*	1168*	966.4+
91	Pa	112601	21105	20314	16733	5367	5001	4174	3611	3442	1387*	1224*	1007*
92	U	115606	21757	20948	17166	5548	5182	4303	3728	3552	1439*b	1271*b	1043+

#		N-IV 4d3/2	N-V 4d5/2	N-VI 4f5/2	N-VII 4f7/2	O-I 5s	O-II 5p1/2	O-III 5p3/2	O-IV 5d3/2	O-V 5d5/2	P-I 6s	P-II 6p1/2	P-III 6p3/2
48	Cd	11.7+	10.7+										
49	In	17.7+	16.9+										
50	Sn	24.9+	23.9+										
51	Sb	33.3+	32.1+										
52	Te	41.9+	40.4+										

53 I	50.6	48.9										
54 Xe	69.5*	67.5*	-	-	23.3*	13.4*	12.1*					
55 Cs	79.8*	77.5*	-	-	22.7	14.2*	12.1*					
56 Ba	92.6+	89.9+	-	-	30.3+	17.0+	14.8+					
57 La	105.3*	102.5*	-	-	34.3*	19.3*	16.8*					
58 Ce	109*	-	0.1	0.1	37.8	19.8*	17.0*					
59 Pr	115.1*	115.1*	2.0	2.0	37.4	22.3	22.3					
60 Nd	120.5*	120.5*	1.5	1.5	37.5	21.1	21.1					
61 Pm	120	120	-	-	-	-	-					
62 Sm	129	129	5.2	5.2	37.4	21.3	21.3					
63 Eu	133	127.7*	0	0	32	22	22					
64 Gd	-	142.6*	8.6*	8.6*	36	20	20					
65 Tb	150.5*	150.5*	7.7*	2.4*	45.6*	28.7*	22.6*					
66 Dy	153.6*	153.6*	8.0*	4.3*	49.9*	26.3	26.3					
67 Ho	160*	160*	8.6*	5.2*	49.3*	30.8*	24.1*					
68 Er	167.6*	167.6*	-	4.7*	50.6*	31.4*	24.7*					
69 Tm	175.5*	175.5*	-	4.6	54.7*	31.8*	25.0*					
70 Yb	191.2*	182.4*	2.5*	1.3*	52.0*	30.3*	24.1*					
71 Lu	206.1*	196.3*	8.9*	7.5*	57.3*	33.6*	26.7*					
72 Hf	220.0+	211.5+	15.9+	14.2+	64.2+	38*	29.9+					
73 Ta	237.9+	226.4+	23.5+	21.6+	69.7+	42.2*	32.7+					
74 W	255.9+	243.5+	33.6*	31.4+	75.6+	45.3*b	36.8+					
75 Re	273.9+	260.5+	42.9*	40.5*	83+	45.6+	34.6*b					
76 Os	293.1+	278.5+	53.4+	50.7+	84*	58*	44.5+					
77 Ir	311.9+	296.3+	63.8+	60.8+	95.2*b	63.0*b	48.0+					
78 Pt	331.6+	314.6+	74.5+	71.2+	101.7*b	65.3*b	51.7+					
79 Au	353.2+	335.1+	87.6+	83.9+	107.2*b	74.2+	57.2+					
80 Hg	378.2+	358.8+	104.0+	99.9+	127+	83.1+	64.5+	9.6+	7.8+			
81 Tl	405.7+	385.0+	122.2+	117.8+	136.0*b	94.6+	73.5+	14.7+	12.5+			
82 Pb	434.3+	412.2+	141.7+	136.9+	147*b	106.4+	83.3+	20.7+	18.1+			
83 Bi	464.0+	440.1+	162.3+	157.0+	159.3*b	119.0+	92.6+	26.9+	23.8+			
84 Po	500*	473*	184*	184*	177*	132*	104*	31*	31*			
85 At	533*	507	210*	210*	195*	148*	115*	40*	40*			
86 Rn	567*	541*	238*	238*	214*	164*	127*	48*	48*	26		
87 Fr	603*	577*	268*	268*	234*	182*	140*	58*	58*	34	15	
88 Ra	636*	603*	299*	299*	254*	200*	153*	68*	68*	44	19	
89 Ac	675*	639*	319*	319*	272*	215*	167*	80*	80*	-	-	
90 Th	712.1+	675.2+	342.4+	333.1+	290*a	229*a	182*a	92.5+	85.4+	41.4+	24.5+	16.6+
91 Pa	743*	708*	371*	360*	310*	232*	232*	94*	94*	-	-	-
92 U	778.3+	736.2+	388.2*	377.4+	321*ab	257*ab	192*ab	102.8+	94.2+	43.9+	26.8+	16.8+

[http://www.chess.cornell.edu/Operations/Reference/Binding_Energies/binding_energies.htm]

Appendix 2 Standard electrode potentials to the nearest 10 mV

Half-Reaction	E_o (V)
$Li^+ + e^- \leftrightarrow Li$	-3.04
$K^+ + e^- \leftrightarrow K$	-2.92
$Ba^{2+} + 2e^- \leftrightarrow Ba$	-2.90
$Ca^{2+} + 2e^- \leftrightarrow Ca$	-2.87
$Na^+ + e^- \leftrightarrow Na$	-2.71
$Mg^{2+} + 2e^- \leftrightarrow Mg$	-2.37
$Al^{3+} + 3e^- \leftrightarrow Al$	-1.66
$Mn^{2+} + 2e^- \leftrightarrow Mn$	-1.18
$2H_2O + 2e^- \leftrightarrow H_2\ (g) + 2\ OH^-$	-0.83
$Zn^{2+} + 2e^- \leftrightarrow Zn$	-0.76
$Cr^{3+} + 3e^- \leftrightarrow Cr$	-0.74
$Fe^{2+} + 2e^- \leftrightarrow Fe$	-0.44
$Cr^{3+} + 3e^- \leftrightarrow Cr$	-0.41
$Cd^{2+} + 2e^- \leftrightarrow Cd$	-0.40
$Co^{2+} + 2e^- \leftrightarrow Co$	-0.28
$Ni^{2+} + 2e^- \leftrightarrow Ni$	-0.26
$Sn^{2+} + 2e^- \leftrightarrow Sn$	-0.14
$Pb^{2+} + 2e^- \leftrightarrow Pb$	-0.13
$Fe^{3+} + 3e^- \leftrightarrow Fe$	-0.04
$2H^+ + 2e^- \leftrightarrow H_2\ (g)$	0.00
$S + 2H^+ + 2e^- \leftrightarrow H_2S\ (g)$	0.14
$Sn^{4+} + 2e^- \leftrightarrow Sn^{2+}$	0.15
$Cu^{2+} + e^- \leftrightarrow Cu^+$	0.16
$SO_4^{2+} + 4H^+ + 2e^- \leftrightarrow SO_2\ (g) + 2H_2O$	0.17
$Cu^{2+} + 2e^- \leftrightarrow Cu$	0.34
$2H_2O + O_2 + 4e^- \leftrightarrow 4OH^-$	0.40
$Cu^+ + e^- \leftrightarrow Cu$	0.52
$I_2 + 2e^- \leftrightarrow 2I^-$	0.54
$O_{2\ (g)} + 2H^+ + 2e^- \leftrightarrow H_2O_2$	0.68
$Fe^{3+} + e^- \leftrightarrow Fe^{2+}$	0.77
$NO_3^- + 2H^+ + e^- \leftrightarrow NO_2\ (g) + H_2O$	0.78
$Hg^{2+} + 2e^- \leftrightarrow Hg\ (l)$	0.78
$Ag^+ + e^- \leftrightarrow Ag$	0.80
$NO_3^- + 4H^+ + 3\ e^- \leftrightarrow NO\ (g) + 2H_2O$	0.96

$Br_2 + 2e^- \leftrightarrow 2Br^-$	1.06
$O_2(g) + 4H^+ + 4e^- \leftrightarrow 2H_2O$	1.23
$MnO_2 + 4H^+ + 2e^- \leftrightarrow Mn^{2+} + 2H_2O$	1.28
$Cr_2O_7^{2-} + 14H^+ + 6e^- \leftrightarrow 2Cr^{3+} + 7H_2O$	1.33
$Cl_2 + 2e^- \leftrightarrow 2Cl^-$	1.36
$Au^{3+} + 3e^- \leftrightarrow Au$	1.50
$MnO_4^- + 8H^+ + 5e^- \leftrightarrow Mn^{2+} + 4H_2O$	1.52
$Co^{3+} + e^- \leftrightarrow Co^{2+}$	1.82
$F_2 + 2e^- \leftrightarrow 2F^-$	2.87

[http://physchem.co.za/Data/Electrode Potentials.htm]